Influence of viral fusion peptides, cellular solutes and cholesterol on the structure of lipid membranes

Dissertation
for obtaining the academic degree
Doctor rerum naturalium
(Dr. rer. nat.)
from the TU Dortmund University

submitted to the Faculty of Physics by

Göran Surmeier
from Bielefeld

Dortmund 2020

1. Supervisor and Referee: Prof. Dr. Metin Tolan

2. Referee: Prof. Dr. Roland Winter

Contents

Chapter 1

Introduction

Amphiphilic lipids are crucial components of every living organism. Due to the hydrophobic effect, they assemble in mesophases once they are dispersed in an aqueous medium [1–4]. These are often based on a bilayer structure in which two lipid layers are arranged symmetrically with their hydrophilic parts facing to the water phase shielding the hydrophobic regions. Cell membranes, which separate the cytoplasm from the environment and enable a controlled mass and information transfer between intra- and extracellular region, are based on this fundamental structure [5, 6]. Furthermore, lipid bilayers can be found in the cell interior, e.g., as constituents of transport vesicles or organelles like the mitochondria, the nucleus, the Golgi apparatus or the endoplasmatic reticulum [7, 8]. The properties of a lipid bilayer depend on many factors like temperature, pressure, composition, or the chemical environment, and transitions between fluid and gel-like states are observed [9, 10]. Typically, cell membranes require the high flexibility of the fluid L_α phase to fulfill their biological functionalities [5, 11]. In this context, conditions like in the Mariana Trench at low temperatures and high pressures appear to be highly unfavorable for living organisms. However, life found strategies to withstand these conditions [12, 13]. These are for example based on the regulation of the amount of lipids with unsaturated fatty acid chains or cholesterol, which are incorporated in membranes [14]. Cholesterol is a molecule that strongly influences the fluidity of a membrane, as its rigid sterol rings affect the mobility and order of the surrounding lipids [15].

Beside lipid membranes, also proteins are strongly affected by pressure and temperature [16]. It is known that an appropriate composition of osmolytes in a cell can prevent the denaturation of proteins at extreme conditions [17–19]. For example, there is a correlation between the depth at which a marine species is found and the concentration of trimethylamine-*N*-oxide (TMAO) in its tissue [20, 21]. While TMAO stabilizes the structure of proteins at high pressures, it was observed that urea has a counteracting influence and a mutual compensatory effect was found [22–25]. However, for a comprehensive understanding of the regulative effects of cellular solutes like TMAO and urea, also their influence on intracellular membrane processes and structures has to be considered. It was found that they can modify the phase behavior, fluidity and hydration

state of bilayers and they are thought to contribute to membrane remodeling processes like endocytosis and fusion [26–32].

The main driving forces of membrane remodeling are often interactions with proteins. An example of such a process is the viral cell entry. Enveloped viruses enter host cells via protein-mediated membrane fusion [33–36]. The proteins are embedded in the viral envelope and interact with the cell membrane pulling cell membrane and viral envelope towards each other [37–39]. Hydrophobic segments located in the ectodomain, which are either called fusion peptides or fusion loops depending on their position in the fusion protein sequence [33, 40], initiate this processes as their insertion into the target membrane leads to destabilization [41–43]. A hemifusion stalk forms and evolves into a fusion pore. It was found that for the generation of a pore also the peptide sequence that anchors the fusion protein in the viral envelope, the so-called transmembrane domain, is essential [44–50]. The intermediate states of membrane fusion are characterized by a negative Gaussian curvature whose molecular origin is subject of current research [37, 51–55].

Non-lamellar lipid structures also exist beyond transient intermediate states as some systems exhibit, e.g., micellar, hexagonal or bicontinuous cubic phases. From this polymorphism various technical applications arise. A focal point of current research are bicontinuous cubic phases due to their potential in fields like drug delivery [56–59], nucleic acid delivery [60–64], medical imaging [58, 65, 66], membrane protein crystallization [67–71], and biosensing [72–75]. A molecule that forms these phases spontaneously in an aqueous solution even at ambient conditions is monoolein [76, 77]. As it is non-toxic, biodegradable, bio-compatible and comparatively cheap in the production, it is suitable for many applications and it is one of the most studied lipids in this context. The unique properties of monoolein also give rise to numerous applications of it as component of model membranes for the investigation of biological processes [51, 76, 78, 79].

This thesis is divided into three subchapters that deal with different factors that affect the behavior of lipid structures. The first project (chapter 4) is a pressure-jump study on the effect of additives on the equilibration of cubic monoolein structures at excess water conditions. The formation of the cubic phase was triggered by an abrupt pressure release beyond the lamellar-to-cubic phase boundary. Due to the high water content of the samples, cubic phases subsequently emerge with much higher lattice constants compared to the equilibrium state. They release the excess of enclosed water in a process that lasts several hours. This process was investigated with small angle X-ray scattering in presence of different additives to explore their effect on the dynamics of lipid self-assembly. Subjects of this experiment were molecules that are crucial for the adaptation of living organisms to external conditions like TMAO and urea as well as viral fusogenic peptides. Model membranes consisting of monoolein or other lipids that form inverse phases are powerful tools to study membrane fusion, as their structure resembles intermediate states that occur in this process [51, 80–86]. The transition from lamellar to cubic phase and subsequent the release of enclosed water is accompanied by an increase of the membrane curvature. Observing how this process is influenced by viral fusion peptides thus provides implications about their role in the destabilization of target membranes.

Apart from viral infestation, numerous processes take place inside of cells that involve the deformation of lamellar membrane structures, and highly curved bilayers constitute the building blocks of certain organelles [87–93]. These structures are formed in an environment that is characterized not only by the presence of osmolytes like TMAO and urea, but also by a variety of soluble and insoluble macromolecules like proteins, lipids, ribosomes, biopolymers, nucleic acids or carbohydrates [23, 94–97]. Therefore, a further subject of this study was the polymer polyethylene glycol (PEG) that was already used in previous studies to simulate molecular crowding like it is found in cells [98–104]. This approach provides insight into the effect of depletion interactions on lipid phase formation. It is known that the presence of PEG in the extra- or intracellular space can induce membrane fusion or fission [105–107]. The investigation of the interaction of PEG and monoolein may also have implications for technical applications of monoolein that rely on the use of polymers to achieve the stabilization of cubosomes [108–111].

The second project (chapter 5) is the structural investigation of phospholipid Langmuir films interacting with viral fusogenic peptides. By combing X-ray reflectometry and grazing incidence diffraction, detailed vertical electron density profiles and lateral lattice parameters of the lipid monolayers have been obtained. While the first project focuses on the influence of fusogenic peptides on the membrane curvature, in this study, their adsorption and penetration behavior at lipid surfaces is characterized.

Viral fusion proteins are divided into three different classes based on different structural properties [33, 35, 112]. In this work, the fusion peptide of class I Influenza virus Hemagglutinin 2 [37, 113–117], the fusion loop of class II Tick-borne encephalitis virus glycoprotein E [38, 118–120], and the fusion loop and transmembrane domain of class III Vesicular stomatitis virus G protein [39, 44, 121–127] have been studied on the basis of amino acid sequences specified by Weise and Reed [128]. The investigations aim to improve the understanding of the molecular mechanisms of viral membrane fusion by identifying characteristics of the interactions of peptides belonging to all three classes with model membranes and contrasting the behavior of anchor and attacking sequences. Beyond increasing the knowledge of viral cell entry, this also has implications for medical applications of fusogenic peptides like the use of the Influenza fusion peptide for nuclear drug delivery in cancer treatment [129–131].

The third project (chapter 6) addresses the effect of cholesterol on the pressure response of 1,2-dimyristoyl-*sn*-glycero-3-phosphocholine (DMPC) membranes. The phase behavior of DMPC vesicles has already been studied in detail and phase boundaries between the L_α phase and several gel-like phases like the rippled $P_{\beta'}$ phase or the lamellar $L_{\beta'}$ phase have been determined [132–135]. There are also studies on the influence of cholesterol showing that the incorporation of cholesterol leads to a broadening of the main phase transition regime until, at a certain concentration, fluid and gel-like phase can no longer be distinguished [15, 136–141]. This state is called liquid ordered L_o phase and it combines the low positional order of the fluid phase with the high orientational order of gel-like phases [142]. However, most studies involving cholesterol only consider membranes at ambient pressure and little is known about the influence of high hydrostatic pressure [139, 143].

A promising but challenging strategy for the analysis of membranes is the preparation

of lipid layers on solid surfaces to enable their exploration with surface-sensitive methods [144–148]. This requires model membranes that are stable on the substrate surface without being influenced by it too much. A simple way to reduce the influence of the substrate is to prepare stacks of bilayers. In literature, solid-supported DMPC multilayers were investigated mostly under humidity gas phase [149, 150], as they lack stability once they are fully immersed in water, especially, when they are heated above the main phase transition temperature [144, 151]. However, it was also observed that the abrasive effect of water can be reduced or even reversed by increasing the pressure beyond the main phase transition boundary [152].

In this work, the structure of solid-supported DMPC multilayers containing cholesterol was analyzed with X-ray reflectometry up to a maximum pressure of 5 kbar. The sample temperature was 20 °C which is slightly below the main phase transition of pure DMPC at ambient pressure. In order to determine the influence of the substrate, the behavior of the multilayers was compared to single bilayers on a solid support and multilamellar vesicles. For the investigation of the vesicles, small angle X-ray scattering was applied. The results have also been published in the journal *Biophysical Chemistry* [153].

The experiments were conducted at the beamlines BL2 [154, 155] and BL9 [156, 157] of the Dortmund Electron Accelerator (DELTA), at the beamlines ID10 [158] and ID31 [159] of the European Synchrotron Radiation Facility (ESRF), and with a Bruker D8 diffractometer.

Chapter 2

Scientific Background

2.1 Polymorphism of lipid self-assembly and inverse bicontinuous cubic phases

The formation of lipid mesophases in aqueous solution is driven by the hydrophobic effect [160, 161]. Interfaces between non-polar molecules and water are entropically unfavorable, since the configuration entropy of the hydrogen bond network is restricted. Therefore, non-polar substances tend to aggregate. Amphiphilic lipids consist of a hydrophilic headgroup and a hydrophobic tailgroup, thus favoring structures in which the headgroups form the interface with the water while the tailgroups have no contact to the aqueous phase. Depending on the ratio of the polar surface area to the expanse of the hydrophobic region, the lipids assemble in very different structures. Rough predictions can be made with the critical packing parameter [162]

$$\gamma = \frac{v}{a_0 l_\mathrm{c}} \tag{2.1}$$

where v is the molecular volume, a_0 the optimum headgroup area and l_c the effective maximum chain extension. If the cross-section of the required space of a lipid parallel to the water interface is constant along the membrane normal, this ratio becomes 1 and the lipids tend to assemble in lamellar structures. When γ deviates from 1, the shape is conical or wedge-like. Then, phases with curved surfaces are preferred. For $\gamma < 1$, a curvature towards the hydrophobic region is induced (commonly referred to as *positive* curvature) and the corresponding phases are denoted by an index 1. For $\gamma > 1$, lipid layers exhibit curvature towards the aqueous phase (commonly referred to as *negative* curvature). These are the so-called inverse phases that are denoted by an index 2. The relationship between the critical packing parameter and the mesophases formed is summarized in figure 2.1.

In the framework of this thesis, lamellar and inverse bicontinuous cubic phases were investigated. While different lamellar phases differ mainly in the configuration of the tailgroups, the three bicontinuous cubic phases each have a fundamentally different architecture. They are based on triply periodic minimal surfaces (TPMS) that have

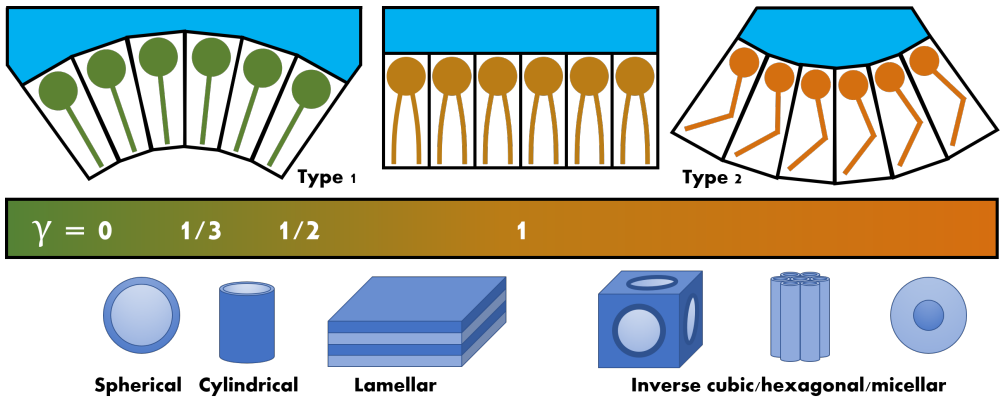

Figure 2.1: Relation between the molecular shape of lipids described by the critical packing parameter γ and the preferred phase geometry. Picture modified from [76].

zero mean curvature H and a negative Gaussian curvature K. Mean and Gaussian curvature result from the principle curvatures c_1 and c_2, which are the inverses of the principle radii of curvature, as

$$H = \frac{c_1 + c_2}{2} \qquad K = c_1 c_2. \tag{2.2}$$

Three types of inverse bicontinuous cubic phases are observed, which are based on the double diamond, the primitive, and the gyroid TPMS [163]. The first two were discovered by Schwarz [164, 165] and the third by Schoen [166]. The cubic phases are designated by their crystallographic space groups, which are Pn3m (double diamond), Im3m (primitive) and Ia3d (gyroid). The lipid phases consist of a bilayer whose hydrophobic core is aligned along a certain TPMS and divides the aqueous phase into two unconnected systems of water channels, which are congruent (Pn3m, Im3m) or enantiomeric (Ia3d). Each channel system forms junctions where a characteristic number of channels intersect. In case of the Im3m phase, the channels meet perpendicularly in 6-way junctions. In the Pn3m phase, 4-way junctions with tetrahedral symmetry occur. The Ia3d phase forms 3-way junctions at angles of 120°. The unit cells of the different phases are illustrated in figure 2.2.

How these phases can be identified by small angle X-ray scattering (SAXS) is explained in chapter 3.1. SAXS also yields the lattice constant a, from which further characteristic parameters like the lipid chain length l or the water channel radius r_w can be determined. The formulae shown in the following paragraphs are taken from [76].

When the water weight fraction in the lipid phase C_W is known, the volume fraction is given by

$$\phi_\mathrm{W} = \frac{C_\mathrm{W}}{C_\mathrm{W} + (1 - C_\mathrm{W})\frac{\rho_\mathrm{W}}{\rho_\mathrm{L}}} \tag{2.3}$$

with the density of water ρ_W and the density of the lipid ρ_L. For monoolein/water mixtures at 25 °C, these parameters are $\rho_\mathrm{W} \approx 0.997\,\mathrm{g/cm^3}$ and $\rho_\mathrm{L} \approx 0.942\,\mathrm{g/cm^3}$ [76].

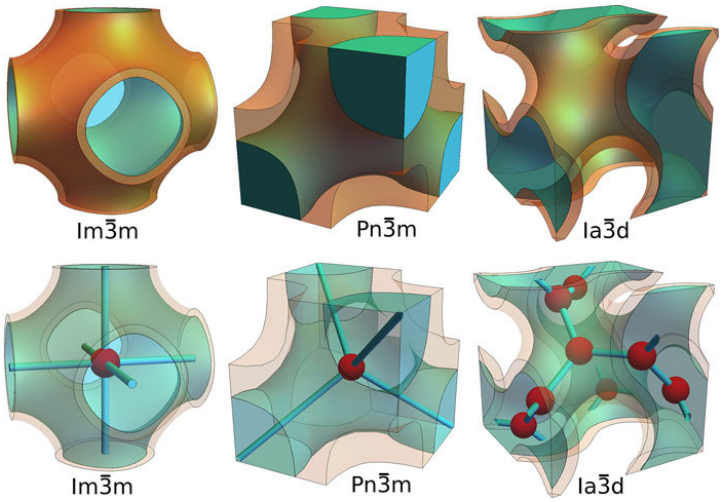

Figure 2.2: Unit cells of the inverse bicontinuous cubic phases. The lipid bilayer is shown in *orange* and one water channel network in *cyan*. The other water channel network is *transparent*. In the lower illustrations, the nodes of the *cyan* water channel network are marked with *red spheres* which are connected by *blue rods* along the water channels. Reprinted with permission from [167]. Copyright © 2018 Authors.

The corresponding lipid volume fraction is $\phi_L = 1 - \phi_W$. Using this, the chain length l can be determined by solving the following equation

$$\phi_L = 2\sigma\frac{l}{a} + \frac{4}{3}\pi\chi\frac{l^3}{a^3} \tag{2.4}$$

where χ is the Euler-Poincaré characteristic of the corresponding TPMS and σ is the ratio of the surface area in an unit cell to a^2. The values of these parameters for the three cubic phases are summarized in table 2.1.

With a and l, the radius of the water channels can be calculated as

$$r_w = \sqrt{-\frac{\sigma a^2}{2\pi\chi}} - l \tag{2.5}$$

and the area per lipid molecule at the interface as

$$a_0 = \frac{2m_L}{\rho_L}\,\frac{\sigma a^2 + 2\pi\chi l^2}{\phi_L a^3} \tag{2.6}$$

with m_L being the mass of a lipid molecule.

As mentioned above, TPMS have zero mean curvature. However, for lipid bilayers of cubic phases, this applies only in the center of their hydrophobic region. At the

Table 2.1: Parameters of cubic lipid phases [76].

TPMS	Space group	χ	σ	Channels per node
Diamond	Pn3m	-2	1.919	4
Primitive	Im3m	-4	2.345	6
Gyroid	Ia3d	-8	3.091	3

surface of the bilayer in a distance l to the TPMS, mean and Gaussian curvature are not constant. Their averaged values are given by

$$\langle H \rangle = \frac{2\pi\chi l}{a_0} \qquad \langle K \rangle = \frac{2\pi\chi}{\sigma a^2}. \tag{2.7}$$

When different cubic phases coexist, they usually share the same Gaussian curvature [168]. Therefore, their lattice constants occur in characteristic ratios of

$$a_{\mathrm{Im3m}} = 1.28 \cdot a_{\mathrm{Pn3m}} \qquad a_{\mathrm{Ia3d}} = 1.58 \cdot a_{\mathrm{Pn3m}}. \tag{2.8}$$

2.2 Monoolein

Monoolein is a lipid that consists of a glycerol backbone with two polar hydroxyl groups that is esterified with an 18 C-atoms long hydrocarbon chain. The chain is monounsaturated and has a *cis* double bond between the ninth and tenth carbon atom. The chemical structure is shown in figure 2.3. Due to the small headgroup in combination with a *cis* unsaturated hydrocarbon chain, monoolein has a high tendency to form inverse phases ($\gamma > 1$). Figure 2.4 shows a temperature-composition phase diagram of monoolein/water mixtures determined via X-ray diffraction and differential scanning calorimetry [77]. It can be seen that monoolein forms the inverse micellar L_2 phase, the inverse hexagonal H_2 phase, and the inverse bicontinuous cubic Ia3d and Pn3m phases. At low water content, also the lamellar fluid L_α phase and, at low temperatures, different polymorphs of the lamellar crystalline L_c phase have been observed. Between 20 °C and 90 °C, the Pn3m phase is present in the excess water regime. The boundary to the excess water regime marks the temperature-dependent maximum capacity for water of the corresponding phase. At 25 °C, this maximum is reached at a water content of approximately 44.5 wt%.

Pressure-dependent phase diagrams of monoolein exist for a few different water contents. Figure 2.5 shows a temperature-pressure phase diagram for excess water conditions obtained with small angle X-ray scattering [169]. At high pressures and low temperatures, a phase transition from the Pn3m to a L_c phase was observed. At limited hydration, also pressure-induced transitions from the Pn3m to the Ia3d phase and from the Ia3d to the L_α phase have been reported [51, 76].

Figure 2.3: The structural formula of monoolein (1-oleoyl-*rac*-glycerol).

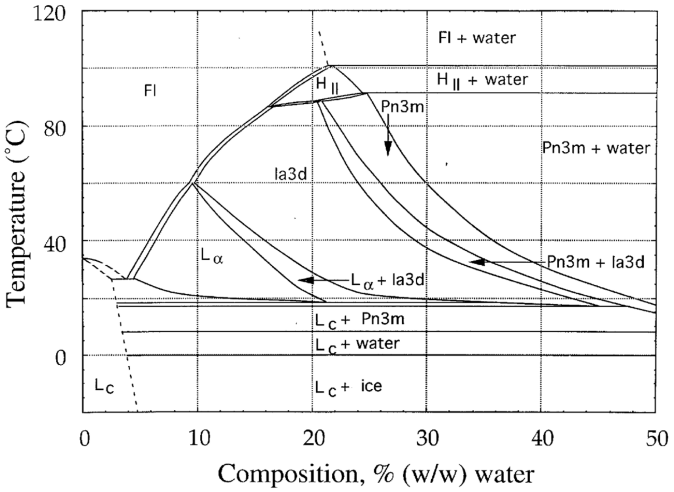

Figure 2.4: Temperature-composition phase diagram of monoolein at ambient pressure. The abbreviation FI stands for *fluid isotropic* and refers to an inverse micellar phase. Reprinted with permission from [77]. Copyright © 1999 Elsevier Science Ltd.

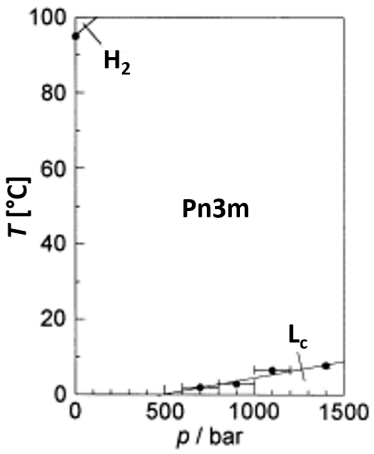

Figure 2.5: Temperature-pressure phase diagram of monoolein at excess water conditions. Adapted with permission from [169]. Copyright © 2001 Elsevier Science Ltd.

2.3 DMPC/cholesterol membranes

The structural formulae of the phospholipid 1,2-dimyristoyl-*sn*-glycero-3-phosphocholine (DMPC) and cholesterol are shown in figure 2.6. Phospholipids are a major component of cell membranes and constitute their bilayer structure. DMPC has two 14 C-atoms long hydrocarbon chains that are fully saturated. These are bound to a glycerol backbone that connects them to a polar headgroup consisting of a phosphate group and choline. The key feature of cholesterol are its four steroid rings. The polar hydroxyl group to which they are bound causes an oriented incorporation in lipid membranes, although cholesterol alone does not form bilayers. On the other side of the molecule is a short hydrocarbon chain. Cholesterol occurs in cell membranes in concentrations of up to 50 mol% [11].

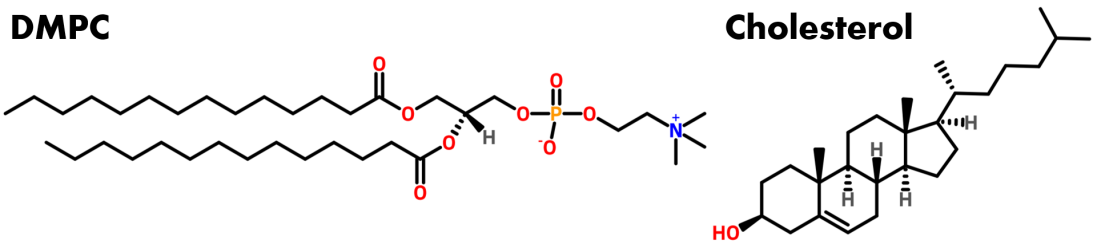

Figure 2.6: The structural formulae of DMPC (1,2-dimyristoyl-*sn*-glycero-3-phosphocholine) and cholesterol.

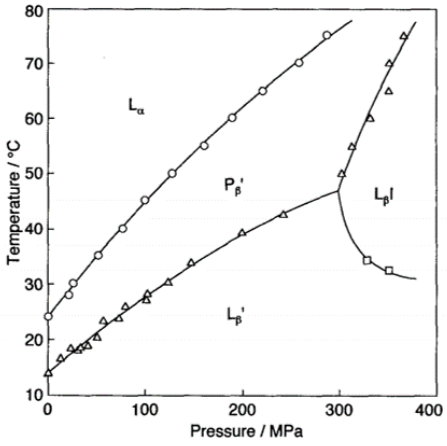

Figure 2.7: Temperature-pressure phase diagram of DMPC membranes. Reprinted with permission from [135]. Copyright © 1998 The Chemical Society of Japan.

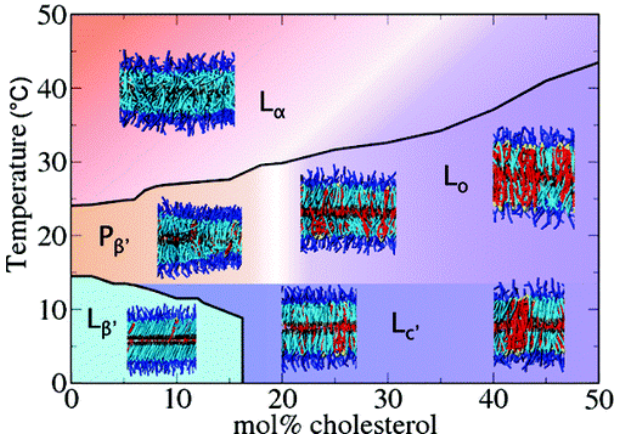

Figure 2.8: Simulated temperature-composition phase diagram of DMPC/cholesterol membranes. Reprinted with permission from [170]. Copyright © 2010 American Chemical Society.

Figure 2.7 shows a temperature-pressure phase diagram of pure DMPC vesicles determined by light transmittance measurements [135]. At ambient pressure, the main phase transition of DMPC between gel-like and fluid L_α phase occurs at approximately 24 °C where the hydrocarbon chains crystallize into an all-*trans* configuration (cooling) or melt into a disordered state (heating). In the gel-like regime exists a pretransition from $L_{\beta'}$ to $P_{\beta'}$ at 14 °C. In both of these phases, the hydrocarbon chains are tilted, but while the bilayer is flat in the $L_{\beta'}$ phase, it has a rippled superstructure in the $P_{\beta'}$ phase. Both transition temperatures increase upon pressurization. In the $L_\beta I$ phase, which was observed at high pressure by Ichimori et al. [135], the tailgroups are interdigitated. Prasad et al. [134] reported the Gel III phase in which the hydrocarbon chains are untilted at high pressures instead.

Figure 2.8 shows how the phase diagram of DMPC is modified by the addition of cholesterol at ambient pressure [170]. The phase diagram was determined with simulations in agreement with previous results of experimental studies [137, 140, 141, 171, 172]. The rigid steroid rings of cholesterol reduce the flexibility of the L_α phase and disturb the order of the gel-like phases [15]. Due to these opposing effects, the phase transition region broadens with increasing cholesterol content until fluid and gel-like phase cannot be distinguished anymore [136–139]. This state is called liquid ordered L_o phase. Furthermore, a non-tilted liquid crystalline L_c phase was observed at low temperature. For high cholesterol contents, a separation of molecules into pure DMPC and cholesterol clusters occurred. The cholesterol-induced broadening of the main phase transition and the development of the L_o phase was also observed in pressure studies [11]. However, the pressure-dependent phase behavior of DMPC is only known for a few temperatures and cholesterol concentrations [133, 139, 143].

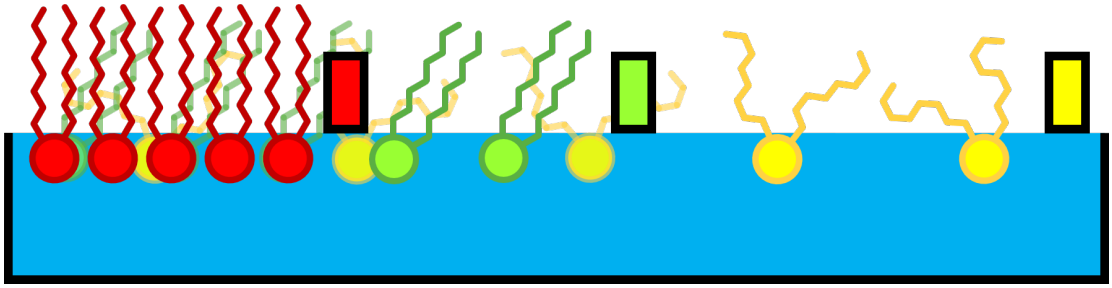

Figure 2.9: A Langmuir monolayer in different states of compression. Upon reduction of the available surface with a movable barrier (*colored rectangle*) from the *yellow* to the *green* to the *red* position, the lipid molecules pass from a gaseous into a crystalline phase. The lipids in the respective states are color matched to the barrier at the corresponding position. Flexibility and tilt of the hydrocarbon chains reduce as the molecular distances decrease.

2.4 DPPC and DPPA Langmuir films

The term Langmuir film refers to layers of insoluble organic materials on an aqueous surface with a thickness of one molecule [173]. Langmuir films are typically prepared in Langmuir troughs, which are flat containers with hydrophobic inner surfaces. These are filled with an aqueous subphase to such an extent that a convex meniscus forms on the surface. This makes it possible to vary the surface area available for the Langmuir film with movable barriers that are placed on the side walls of the trough. The compression level of a Langmuir monolayer can be described with the surface pressure $\Pi = \gamma_0 - \gamma$ that is given by the difference of the surface tension of an empty surface of the corresponding subphase γ_0 and the tension which is observed in presence of the film γ.

Figure 2.9 illustrates different states of compression of a Langmuir monolayer which consists of amphiphilic lipids. The lipids align with their polar headgroups immersed in the subphase and their hydrophobic hydrocarbon chains protruding from it. The lipid film undergoes certain phase transitions depending on the available surface area [174]. If the density of the molecules is low, the film can be described as a two-dimensional gas based on the ideal gas law. When the distances between the molecules are reduced, they start to interact and at a certain level of compression, the surface pressure starts to increase. The lipids enter the liquid-expanded state in which they maintain the conformational disorder of the gaseous phase (*yellow*). Upon further compression, the molecules start to arrange in a two-dimensional lattice and the hydrocarbon chains crystallize (*green*). This state is called liquid-condensed phase. When the reduction of the surface area is continued, the lattice constant and the molecular tilt angle decrease (*red*) until the monolayer finally collapses [175].

In this thesis, Langmuir films consisting of 1,2-dipalmitoyl-*sn*-glycero-3-phosphocholine (DPPC) and 1,2-dipalmitoyl-*sn*-glycero-3-phosphate (DPPA) were used to mimic the outer monolayer of a cell that is attacked by viral fusion peptides. The structural formulae are shown in figure 2.10. DPPC is one of the most abundant phospholipids in the human body [176]. At pH 5, it is uncharged. This pH value corresponds to the

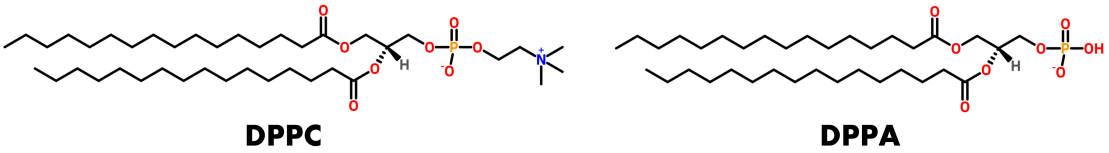

Figure 2.10: The structural formulae of DPPC (1,2-dipalmitoyl-*sn*-glycero-3-phosphocholine) and DPPA (1,2-dipalmitoyl-*sn*-glycero-3-phosphate).

conditions at which the fusion proteins whose fusogenic peptides are studied in this work are active. DPPA has the same tailgroup as DPPC consisting of two 16 C-atoms long hydrocarbon chains, but the headgroup carries a negative charge at pH 5. Previous studies showed that anionic lipids can play a crucial role for the interaction of fusogenic peptides with target membranes [177].

DPPC and DPPA Langmuir films behave very differently upon compression. As the headgroup of DPPA is much smaller than the headgroup of DPPC, van der Waals interactions between the hydrocarbon chains are much more pronounced in DPPA films [178]. This can be seen especially in the fact that DPPC has a wide liquid-expanded phase regime, whereas DPPA forms a crystalline order immediately when the first increase of the surface pressure occurs upon compression from the gaseous regime. In chapter 5.5, the behavior of both lipids is discussed in detail based on experimentally obtained isotherms.

2.5 Viral membrane fusion and fusogenic peptides

The description of viral membrane fusion is based on the reviews of White and Whittaker [33], Harrison [34, 35] and Podbilewicz [112] unless indicated otherwise.

Enveloped viruses deliver their genomes into the cytoplasm of their host cells by membrane fusion. Only some of them attack the plasma membrane directly. In most cases, viruses enter the interior of the target cell via endocytosis and the environmental changes which are associated with their encapsulation launch a fusion mechanism with the endosomal membrane. The process of membrane fusion is catalyzed by fusion proteins located on the virion surface. This is necessary as energetic barriers have to be overcome, e.g., due to the repulsive hydration force [37, 179, 180]. The fusion proteins are held in a prefusion conformation until they are converted to a fusion-competent state by priming. This involves an event of proteolytic cleavage that takes place in the fusion protein itself or in a companion protein. A primed fusion protein can be triggered to release a hydrophobic segment buried in its structure. The trigger can be binding to a receptor, exposure to low pH, binding to a receptor followed by exposure to low pH, or binding to a receptor followed by proteolytic cleavage. If the hydrophobic segment is located at the N-terminal, it is called fusion peptide (FP), if it is internal to the fusion protein, it is called fusion loop (FL). After its exposure, it can insert into the target membrane. The fusion protein that is also anchored in the viral envelope by a

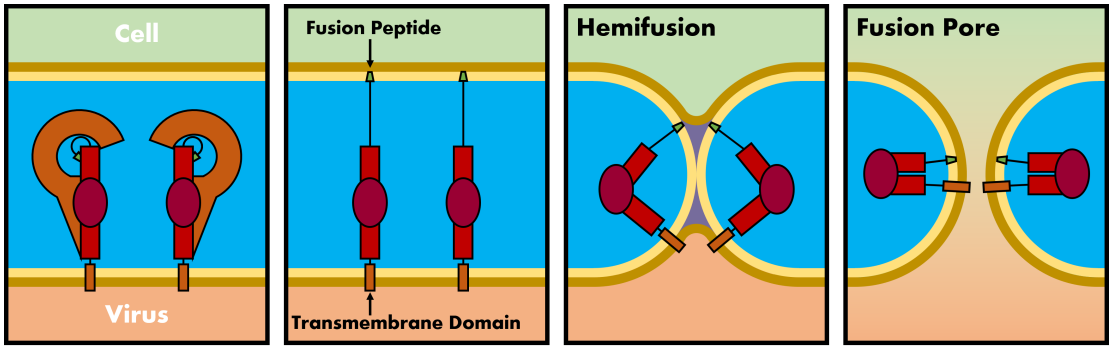

Figure 2.11: Schematic illustration of a protein-mediated fusion process. The inner monolayers of viral envelope and plasma membrane are represented in *brown* and the outer monolayers in *yellow*. The *first frame* shows the fusion proteins in a fusion-incompetent state. After a priming event, the release of the fusion peptide can be triggered, e.g., by a reduction of the pH value. In the *second frame*, the fusion proteins connect virus and cell as their FPs are inserted into the plasma membrane. Then, refolding of the fusion proteins pulls the membranes together and the outer monolayers fuse. The *third frame* shows the corresponding intermediate state of hemifusion. The fusion pore finally opens as also the inner monolayers fuse. This is depicted in the *fourth frame*.

transmembrane domain (TMD) then bridges viral and cellular membrane. By refolding, it pulls both membranes together and causes at first the inner monolayers to fuse, a hemifusion stalk forms [181, 182], and then the entire bilayers, a fusion pore opens [44, 183, 184]. In the post-fusion state, the fusion proteins typically form hairpin-like trimers. In this stage, the FPs or FLs are in contact with the TMDs. Their interaction is thought to complete the fusion process [44–49]. The protein-mediated fusion mechanism is illustrated in figure 2.11.

Fusion proteins are divided into three different classes based on their structural properties. Class I fusion proteins are trimeric proteins mainly build of α-helices with a central coiled-coil structure [37, 114]. The fusion proteins of class II have an extended β-sheet structure and rearrange from a homo- or heterodimeric prefusion into a homotrimeric postfusion state [38]. Class III fusion proteins exhibit structural features of class I and II and typically require no priming event [39, 113, 125]. For the sake of completeness, it should be mentioned that a fourth class exists to which fusion-associated small transmembrane proteins of non-enveloped reoviruses are assigned [185, 186]. However, subject of this thesis are only the fusion mechanisms of enveloped viruses.

In this work, the FP of class I Influenza virus Hemagglutinin (HA) glycoprotein [37, 113–117], the FL of class II Tick-borne encephalitis virus (TBEV) glycoprotein E [38, 118–120], and the FL and TMD of class III Vesicular stomatitis virus (VSV) G protein [39, 44, 121–127] have been studied. Additionally, a highly hydrophobic artificial sequence called L16 was examined as a reference to distinguish between effects originating from unique structural features of the fusogenic peptides and general properties of hydrophobic peptides. All three fusion proteins from which the fusogenic peptides were taken are triggered by the drop of the pH that occurs after their encapsulation in endo-

Table 2.2: Sequences of the investigated fusogenic peptides from Weise and Reed [128]. The numbers refer to the positions of the residues in the corresponding fusion proteins. The text color indicates **acidic**, **basic**, **polar**, **aromatic** and **aliphatic** residues.

Peptide	Sequence	Classification
HA2-FP	GLFGA^{5} IAGFI^{10} ENGWE^{15} GMIDG^{20} GCGKKKK	class I
TBEV-FL	DRG^{100} WGNHC^{105} GLFGK^{110} G GCGKKKK	class II
VSV-FL	QGTWL^{105} NPGFP^{110} PQSCG^{115} YATVT^{120} D GCGKKKK	class III
VSV-TMD	FFF^{470} IIGLI^{475} IGLFL^{480} VL GCGKKKK	class III
L16	LLLLLLLLLLLLLLL WGCGKKKK	artificial

somes. The fusion process of HA is the most widely studied. The inactive precursor HA0 cleaves into HA1 and HA2 during priming [37]. HA1 attaches to sialic-acid receptors on the target cell surface and exposes the fusion-active subunit HA2 that releases the fusion peptides. HA1 dissociates and is not involved in the further process. While the trimeric pre- and postfusion states of HA are known in detail, the cascade of refolding events that catalyses the membrane fusion is not fully understood. On the surface of TBEV, the fusion protein E occurs in association with the companion protein prM which prevents activation until priming [118]. As in all class II fusion processes, priming occurs in the companion protein. After the priming event, the now exposed FLs of the E proteins interact and trigger a trimerization before the refolding cascade starts [119, 120]. The VSV G protein is the only protein on the VSV virion surface and does not require a priming cleavage to become activated. Therefore, its pre- to postfusion transition is reversible [122, 187]. There is evidence that VSV G fusion proteins form monomeric intermediates during the conformational changes from pre- to postfusion trimers [39, 122, 188, 189].

The amino acid sequences that were examined in this study are summarized in table 2.2 and were taken from Weise and Reed [128]. The design of the model peptides is based on the host-guest system by Han and Tamm [190]. Besides the actual fusogenic sequence, they also consist of an anchor unit that is highly charged and thus, ensures sufficient solubility in aqueous buffer and prevents aggregation in solution. The charge is provided by four consecutive lysines. These are connected to the fusogenic peptide by the flexible linker unit glycine-cysteine-glycine to avoid that the conformation of the fusogenic sequence is affected by the anchor unit. The anchor unit can promote the interaction of the peptides with anionic membranes, but is not able to penetrate lipid layers and has no affinity to reside in the hydrophobic region of membranes.

The HA2-FP was found to have a high structural flexibility between α-helix and random coil and turn structure under fusogenic conditions [128, 191, 192]. It inserts into membranes as two antiparallel α-helices [115, 193–195]. Han et al. [196] analyzed the structure of the HA2-FP model sequence, which is also used in this work, in phospholipid micelles via nuclear magnetic resonance and electron paramagnetic resonance spectroscopy. They observed a N-terminal helix involving the residues L2 to I10 followed by a turn that is stabilized by hydrogen bonds between the NHs of E11 and N12 and the

carbonyls of G8 and F9 and a short helical sequence from E15 to D19 that is only present at pH 5 and not at neutral conditions. The resulting V-shape is oriented with the open side towards the hydrophobic core in lipid bilayers. The formation of the C-terminal helix rotates the charged residues E15 and D19 to the top and is thought to increase the hydrophobicity of the bottom side and thus the penetration depth and the lateral pressure exerted on the lipid tailgroups. In further studies, it was observed that HA2-FP tends to oligomerize in a membrane mimicking environment [192, 197]. Moreover, the stress that is exerted on a membrane due to the insertion of HA2-FP was found to modify the membrane structure and curvature [41, 191, 198, 199]. It is discussed that it induces negative curvature [51, 85, 200], which is characteristic for hemifusion stalks, or positive curvature [83, 201], which promotes the formation of nipple-like precursors of hemifusion.

The FL of TBEV includes the residues D98 to G111 and is found at the tip of an elongated domain formed of two disulfide-stabilized loops [118, 120, 202, 203]. In contrast to the HA2-FP, no structural flexibility is found for the TBEV-FL. Its random coil and turn structure is stabilized by internal hydrogen bonds, a salt bridge between D98 and K110, and a disulfid bridge between C74 and C105 [128, 204]. It is assumed that the loops penetrate the membrane via an aromatic anchor formed by W101 and F108, whose insertion depth is limited by surrounding charged and polar residues [177, 205]. It was found that TBEV-FLs can strongly affect the structure of lipid membranes. In presence of TBEV-FLs, the pressure-temperature phase diagram of monoolein at limited hydration changes drastically and monoolein adopts phases with higher negative curvature [51].

VSV exhibits a bipartite FL consisting of W72-Y73 and Y116-A117 [39, 124, 126]. Similar to class II fusion peptides, the FLs of VSV are believed to attack the membrane via aromatic residues whose penetration depth is limited by adjacent amino acids [125]. Obviously, it is problematic to study a bipartite loop based on the experimental approach to examine isolated fusogenic sequences. The sequence examined in this work contains the residues Q101 to D121 and thus includes only one part of the loop and its environment. Although the impact of Y73 for the fusion process was underlined by Sun et al. [124], this region was chosen since it is highly conserved and its significance for the fusion process was pointed out in many studies [128, 206–208]. The sequence shows structural flexibility between α-helix and random coil and turn structure similar to class I fusion peptides. However, there is no evidence of a helical insertion into membranes [206].

The VSV-TMD involves the residues F468 to L482 and is thought to insert into bilayers as an α-helix aligned almost parallel to the membrane normal, as it was also observed for TMDs of other fusion proteins [45, 46, 209–211]. However, it shows conformational flexibility between α-helix and β-sheet at fusogenic pH mainly due to the presence of glycines and isoleucines [128, 209]. Glycine can destabilize α-helices in TMDs acting as a flexible hinge [212], while the side chains of isoleucines provide a high β-sheet propensity resulting from steric interactions [213, 214]. The observed structural flexibility seems to be crucial for the role of TMDs in membrane fusion [215, 216]. While early studies suggested that the fusogenic activity of VSV G protein does not depend on

the exact amino acid sequence of its envelope anchoring unit [217], more recent results demonstrated that replacement of the TMD can strongly reduce the fusion activity or even cause the fusion process to abort in the hemifusion state [44]. This implies that FL and TMD, which are in close proximity at this stage, need a structural compatibility to facilitate the opening of a fusion pore.

2.6 Urea, TMAO and sucrose

In cell biology, the term *osmolyte* refers to substances of low-molecular weight that are formed or incorporated by a cell in a hypertonic milieu to level the osmotic stress [20, 21, 218, 219]. As the concentration range in which inorganic ions do not perturb the metabolism of a cell is typically small, organic osmolytes with minor influence on cellular processes, called *compatible* solutes, are crucial for the adjustment of the osmolality [220]. The group of organic osmolytes includes polyols and sugars, free amino acids and amino acid derivates, urea and methylamines [221]. However, compatibility is not given for all of them. It was found that some of these molecules can have a considerable effect on the structure of macromolecules like proteins, which is suppressed in cells by an appropriate composition of stabilizing and denaturing agents. Therefore, terms like *compensatory* or *counteracting* solutes became more common [17, 222].

A widely studied couple of counteracting osmolytes are TMAO (trimethylamine-*N*-oxide) and urea (figure 2.12), which are found in many marine species that are exposed to osmotic stress and hydrostatic pressure in a characteristic molar ratio of 2:1 (urea:TMAO) [223–225]. The presence of urea shifts the conformational equilibrium of proteins towards unfolded states, while TMAO is able to stabilize their native structure. It is believed that urea accumulates in proximity of proteins due to favorable interactions with the protein backbone and amino acid side chains. Since a compact protein structure limits the possible amount of such interactions, this constitutes a thermodynamic driving force for unfolding [223, 226–228]. For TMAO, an indirect mechanism is proposed. Accordingly, the strong interactions of TMAO and water prevent the molecule from residing in vicinity of proteins resulting in an *osmophobic effect* that favors folded protein conformations with low surface area [229–232]. However, less is known about the mechanism of TMAO counteracting the denaturing effect of urea. There is doubt about explanations stating that TMAO and urea form strong hydrogen bonds [233, 234] or that TMAO displaces urea from the protein surface [235], since more recent studies suggest that there is little direct interaction between the two molecules [236] and that

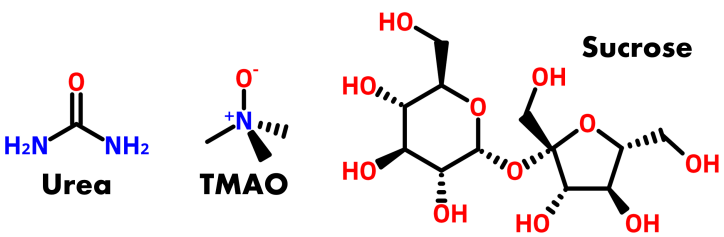

Figure 2.12: The structural formulae of urea, TMAO and sucrose.

the distribution of urea near the protein is not affected by TMAO [237]. Therefore, it is assumed that the counteracting effect results in sum from the individual interactions of TMAO and urea with water and proteins [25, 238, 239].

While the compensatory effects of TMAO and urea on proteins have been a focal point of research for a long time, less attention has been paid to their interaction with lipid structures, which goes beyond an adjustment of the osmotic pressure on the plasma membrane as a simple effect of the number of dissolved particles. Also in this context, limits of the *compatibility* are found and individual effects of single osmolytes come into play [29, 240, 241]. It was observed that interactions of TMAO with lipid headgroups are unfavorable, causing an exclusion of TMAO from membrane interfaces. Consequently, TMAO solution is displaced from inter-bilayer spaces, so that an attractive force is generated between membranes [26]. This phenomenon can also be described by a TMAO concentration gradient between inter-bilayer and bulk water, which leads to an osmotic pressure. Manisegaran et al. [27] found that TMAO causes a reduction of the spacing of multi-lamellar vesicles in a broad temperature and pressure range, accompanied with an increase of the conformational order of the lipid tails, a shift of phase boundaries towards higher temperatures and lower pressures, and a coalescence of liquid disordered domains in multi-component membranes consisting of saturated and unsaturated phospholipids and cholesterol. In contrast, urea shows an affinity to reside near lipid headgroups and thus does not dehydrate inter-bilayer spaces. Instead, it was observed that urea increases the hydration level of cubic monoolein phases [71, 242]. Further, it can act as a substitute for solvents at dry conditions and it is able to prevent phase transitions of lipid bilayers that are caused by severe dehydration, promoting the fluid phase [28, 30].

In addition to TMAO and urea, sucrose (figure 2.12) is examined in the framework of this thesis. Sucrose is an osmolyte that has only a weak ability to stabilize native protein structures compared to TMAO [243, 244]. It was found to have an affinity to interact with phosphatidylcholine headgroups and it can act as a solvent substitute at dry conditions similar to urea [245, 246]. The interaction with membrane surfaces causes a swelling of multi-lamellar lipid structures at low concentrations. Upon addition of higher amounts of sucrose, an exclusion of the molecules from inter-bilayer spaces dominates and the lamellar spacing reduces [26, 247]. It was observed that sucrose decreases the lattice constants of cubic monoolein structures in excess water [242, 248] and shifts the phase boundaries at limited hydration towards phases with higher negative curvature [71, 249, 250].

2.7 Polyethylene glycol and the excluded volume effect

Living cells are occupied by various macromolecules reaching total concentrations of 50-400 mg/mL [95, 96, 251]. Since typically each single species does not occur in a high concentration, these environments are not referred to as *concentrated*. Instead, the term *crowded* is used. Considering the diversity of macromolecules, the effects of crowding on biochemical processes can be attributed mainly to non-specific interactions [252, 253]. Non-specific interactions result from global properties of molecules rather than

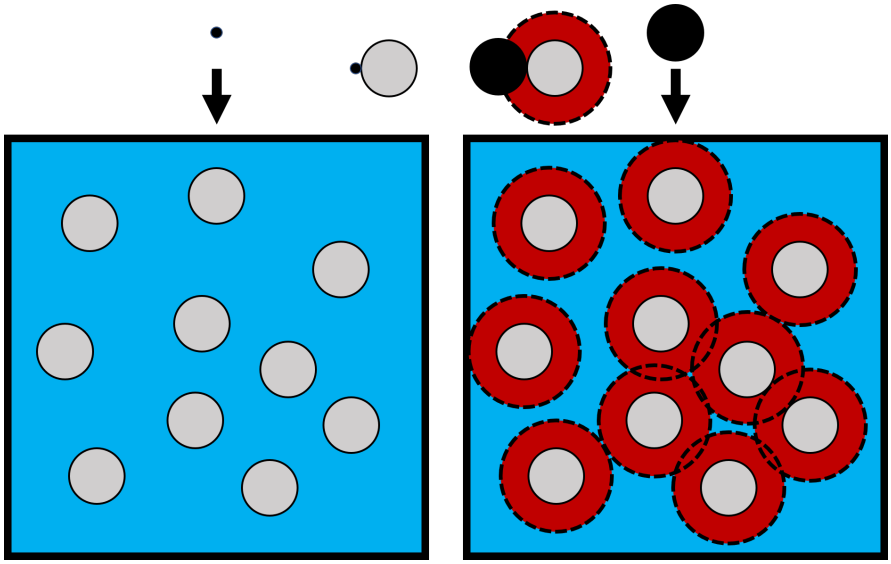

Figure 2.13: Illustration of the excluded volume effect. The crowding agents (*gray*) reduce the available space (*blue*) for the test particles (*black*). For small particles, the excluded volume is almost equal to the volume occupied by the crowding agents. The minimum distance between the test particle and the surface of a crowding agent is given by its radius, so that the excluded volume (*red*) per molecule increases for larger particles.

from particular structural features and include steric, electrostatic, and hydrophobic interactions. Molecular crowding shifts chemical equilibria and interaction constants. The most fundamental contribution is the steric repulsion as all molecules share the property of being mutually impenetrable [254]. Therefore, the presence of background molecules reduces the available volume for particles involved in cellular processes. Figure 2.13 illustrates how crowding affects particles of different sizes. When a particle is small compared to the background molecules, the excluded volume is almost equal to the volume occupied by the crowding agents. For a particle that has a similar size or is even larger than the background molecules, the situation is different. As the components cannot overlap, the radius r of the particle defines the minimal distance of its center to the surface of a crowding agent. Thus, a spherical shell with a thickness r around each background molecule adds to the excluded volume. The reduction of the available space decreases the configuration entropy, accompanied by an increase of the free energy and the chemical potential [99, 100, 255].

The excluded volume effect can be a driving force for aggregation of larger particles. As shown in figure 2.14, an overlap of the excluded regions around the particles increases the available space for the surrounding molecules and thus also their configuration entropy [256]. The exclusion of molecules from the space between the larger particles leads to an anisotropy of the osmotic pressure that promotes the cohesion [257–261]. This so-called depletion force is counteracted by diffusion, since aggregation generates concentration gradients [262].

In the framework of this thesis, polyethylene glycol (PEG) of different sizes was

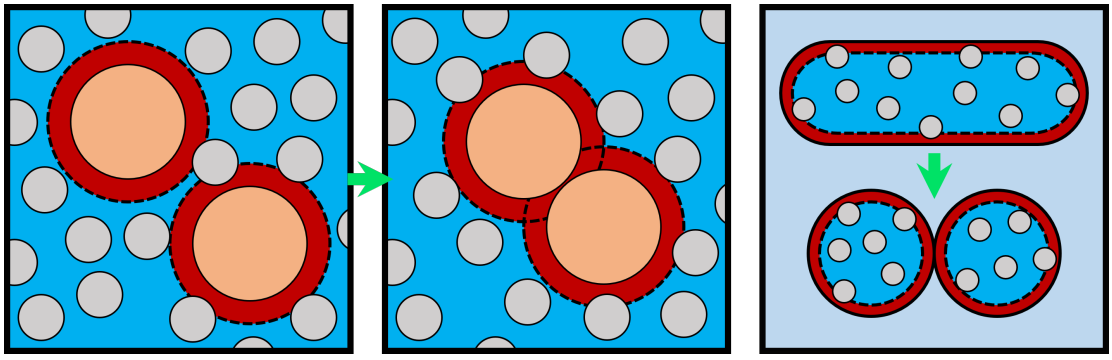

Figure 2.14: Illustration of how the excluded volume effect can be a driving force of aggregation, fusion and budding. The *orange* objects in the *first frame* reduce the available space for the *gray* particles, excluding them from the *red* colored area. The configurational entropy increases upon aggregation of the large molecules (*second frame*), as the excluded *red* spaces now overlap and thus the total excluded volume is reduced. When the orange objects represent vesicles or cells, this process leads to a partial dehydration of the membrane surfaces and promotes fusion events. The *third frame* illustrates how crowding agents inside of a vesicle can induce budding. If the area of the surface is constant and the surface includes a constant volume, the excluded volume due to the confinement decreases, when the curvature of the membrane increases.

applied as crowding agent. Figure 2.15 shows the chemical formula of the polymer. In this work, the smallest applied polymer was PEG 200 (molar mass $M = 200\,\mathrm{g/mol}$) and the largest PEG 35000 (molar mass $M = 35000\,\mathrm{g/mol}$). From the molar mass M, the radius of gyration R_G and the hydrodynamic radius R_H can be calculated as

$$R_\mathrm{G} = 0.215 \cdot M^{0.588\pm0.031}\,\text{Å} \qquad R_\mathrm{H} = 0.145 \cdot M^{0.571\pm0.009}\,\text{Å} \tag{2.9}$$

based on power laws established by Devanand and Selser [263]. When the concentration of PEG c is larger than the overlap concentration

$$c^* = \frac{M}{4/3\pi N_\mathrm{A} R_\mathrm{G}^3}, \tag{2.10}$$

with N_A being the Avogadro constant, the polymers form an entangled mesh [264, 265]. For $c \ll c^*$, the properties of individual PEG molecules determine the behavior of the solution, while it is essentially defined by the volume concentration above c^*. The

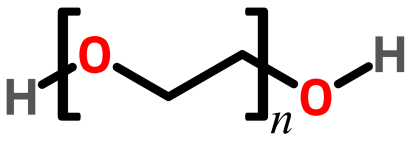

Figure 2.15: The structural formula of PEG.

Table 2.3: Radii of gyration R_G, hydrodynamic radii R_H and overlap concentrations c^* of PEG of different molecular weight M.

M [g/mol]	R_G [Å]	R_H [Å]	c^* [g/L]
200	4.72	2.99	754
400	7.07	4.44	449
600	8.96	5.59	331
1000	12.06	7.49	226
1500	15.28	9.44	167
2000	18.07	11.12	134
4000	27.07	16.53	80
8000	40.55	24.55	48
35000	95.86	57.02	16

properties of the applied PEG are summarized in table 2.3. The osmotic pressure exerted by PEG was found to decrease with the molecular weight and to increase with the concentration [266].

The presence of PEG removes water from the inter-bilayer spaces of multi-lamellar lipid structures [241, 267] and shifts lipid phase boundaries, promoting phases with negative curvature [268]. As a result of depletion and dehydration, PEG can induce cell fusion [105, 106, 267, 269, 270]. When PEG is placed inside of vesicles, its exclusion from regions close to the lipid surface can be a driving force for budding, since the excluded volume reduces with increasing membrane curvature [107]. How crowding agents can induce fusion and fission is illustrated in figure 2.14.

Chapter 3

Experimental methods

Common to all experiments that were conducted in the framework of this thesis is that they are based on structural investigations of lipid membranes with X-ray scattering methods. Three different techniques have been applied, which are introduced in this chapter. The first section deals with small angle X-ray scattering (SAXS) which was used to identify and characterize mesophases formed by lipids in an aqueous environment. Then, X-ray reflectometry (XRR) and grazing incidence diffraction (GID) will be described. These methods are surface-sensitive and were applied to study the behavior of Langmuir films and solid-supported multilayers. XRR provides information on the laterally averaged vertical electron density distribution of thin films, while the lateral lattice structure of lipid layers can be determined by GID. In the last section of this chapter, the custom-made high hydrostatic pressure sample cells are introduced, which were used to perform X-ray scattering experiments at pressures of up to 5 kbar.

In the following, formula symbols in bold print stand for vectors $\boldsymbol{X}$, while normal print refers to their absolute values $X = |\boldsymbol{X}|$. A caret denotes the unit vector $\widehat{\boldsymbol{X}} = \frac{\boldsymbol{X}}{X}$. For clarity, vector arrows are only used in figures.

3.1 Small angle X-ray scattering

Small angle X-ray scattering is a technique that provides structural information on a sample system by observing its elastic scattering. The name is derived from the recorded scattering angles, which are typically below 5°. SAXS enables to resolve structural features of the size of 10 to 1000 Å. This corresponds to the dimensions of nanoparticles and macromolecules like proteins as well as the lattice constants of lipid phases. These range from the typical thickness of a bilayer of 30-60 Å to the repeat units of bicontinuous cubic phases which can reach to more than 200 Å. This chapter focuses on the theoretical principles that are essential for the latter application. The description of the concepts is based on the textbook "Festkörperphysik" by Rudolf Gross and Achim Marx [271].

The basic scattering geometry of a SAXS experiment is shown in figure 3.1. A monochromatic X-ray beam with a wavelength λ and a wave vector $\boldsymbol{k}_\mathrm{i} = \frac{2\pi}{\lambda}\widehat{\boldsymbol{k}}_\mathrm{i}$ hits the sample and the scattered intensity is detected as a function of the scattering angle 2θ.

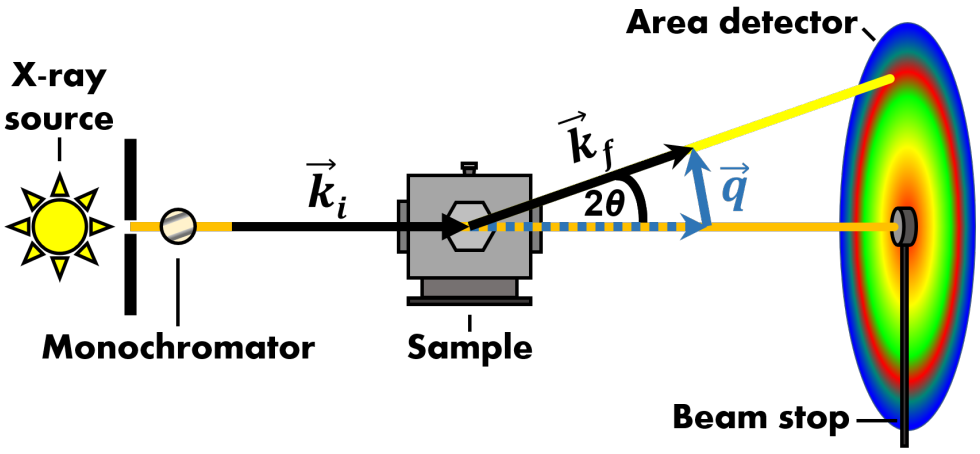

Figure 3.1: Basic scattering geometry of a SAXS experiment.

For a representation independent of the incident energy, the scattering angle is typically converted to the momentum transfer $\boldsymbol{q} = \boldsymbol{k}_\mathrm{f} - \boldsymbol{k}_\mathrm{i}$. In case of fully elastic scattering, the absolute value of the momentum transfer can be determined as $q = \frac{4\pi}{\lambda} \sin\theta$.

Periodic structures like crystal lattices and also multi-lamellar arrangements of lipid bilayers with repetition units in the order of magnitude of the wavelength lead to the occurrence of sharp reflections at certain scattering angles. For crystal planes spaced at a distance d, the positions of these so-called Bragg reflections can be determined by the Bragg condition [272]

$$2d \sin\theta = n\lambda, \tag{3.1}$$

where n is a positive integer.

A more comprehensive view is offered by the description of Max von Laue [273]. Accordingly, the scattering of a plane wave $\Psi(\boldsymbol{r}) = \Psi_0 \mathrm{e}^{\mathrm{i}\boldsymbol{kr}}$ from a three-dimensional Bravais lattice $\boldsymbol{R} = n_1\boldsymbol{a}_1 + n_2\boldsymbol{a}_2 + n_3\boldsymbol{a}_3$, where n_i are integers and $\boldsymbol{a}_\mathrm{i}$ are the primitive translation vectors, interferes constructively when the wave vector transfer is a reciprocal lattice vector. The reciprocal lattice $\boldsymbol{G} = h\boldsymbol{b}_1 + k\boldsymbol{b}_2 + l\boldsymbol{b}_3$, where h,k,l are integers and $\boldsymbol{b}_i$ are the reciprocal translation vectors, is defined by $\mathrm{e}^{\mathrm{i}\boldsymbol{GR}} = 1$. The von Laue condition is therefore

$$\boldsymbol{q} = \boldsymbol{G}. \tag{3.2}$$

Under neglect of multiple scattering, the kinematic approximation (which is equivalent to the Born approximation) provides information about the intensity of the reflections. The form factor $f(\boldsymbol{q})$ of a single base atom of a crystal lattice is obtained as the Fourier transform of its charge distribution and its square is proportional to the scattering intensity. For small scattering angles, it becomes independent of $\boldsymbol{q}$ and proportional to the atomic number of the base atom. By phase correct summation of the form factors of all atoms in the unit cell, the structure factor $S(\boldsymbol{q})$ is obtained. Taking

Table 3.1: Characteristic ratios of the positions in q of diffraction maxima of different lipid phases.

Pn3m	$\sqrt{2} : \sqrt{3} : \sqrt{4} : \sqrt{6} : \sqrt{8} : \sqrt{9} : \sqrt{10}...$
Im3m	$\sqrt{2} : \sqrt{4} : \sqrt{6} : \sqrt{8} : \sqrt{10} : \sqrt{12} : \sqrt{14}...$
Ia3d	$\sqrt{6} : \sqrt{8} : \sqrt{14} : \sqrt{16} : \sqrt{20} : \sqrt{22} : \sqrt{24}...$
Lamellar	$1 : 2 : 3 : 4 : 5 : 6 : 7...$
Hexagonal	$1 : \sqrt{3} : \sqrt{4} : \sqrt{7} : \sqrt{9} : \sqrt{12} : \sqrt{13}...$

into account the von Laue condition 3.2, possible scattering vectors can be described by the coefficients h,k,l of the reciprocal lattice. If the unit cell atoms are located at the positions (x_i,y_i,z_i), the structure factor is given as

$$S_{hkl} = \sum_i f_i \mathrm{e}^{-\mathrm{i}2\pi n(hx_i+ky_i+lz_i)}. \tag{3.3}$$

For a cubic crystal structure with an atom with the form factor f_1 at (0,0,0) and an atom with the form factor f_2 at ($\frac{1}{2}$,$\frac{1}{2}$,$\frac{1}{2}$) the structure factor is

$$S_{hkl} = f_1 + f_2 \mathrm{e}^{-\mathrm{i}\pi(h+k+l)} = \begin{cases} f_1 + f_2 & \text{if } \; h+k+l = \text{even} \\ f_1 - f_2 & \text{if } \; h+k+l = \text{odd}. \end{cases} \tag{3.4}$$

For $f_1 = f_2$, this describes a body-centered cubic lattice. It can be seen that in this case only those reflexes occur whose h,k,l triplets have an even sum. This example illustrates that it is possible to deduce the lattice structure of a sample system on the basis of the observed reflections and their intensities in a diffraction experiment.

If one can assign a h,k,l triplet to an observed reflection at $q = q_{hkl}$, the lattice constant

$$a = \frac{2\pi}{q_{hkl}} \frac{1}{\sqrt{h^2 + k^2 + l^2}} \tag{3.5}$$

of the crystal structure can be determined.

The same principles apply for the identification of the mesophases of monoolein that are described in chapter 2.1. Here, the scattering patterns are mainly determined by the electron density contrast between the less dense hydrophobic areas and the surrounding water. In case of the bicontinuous cubic phases, the corresponding periodic minimal surface defines a region of minimal electron density and thus a periodic modulation of the electron density with a specific symmetry belonging to a certain space-group [274, 275]. The bicontinuous cubic Im3m phase, for example, has the same symmetry as a body-centered cubic lattice and so the occurrence of reflections in a SAXS pattern is given by equation 3.4 with $f_1 = f_2$. The structure factors of further phases formed by monoolein are summarized in table 3.1.

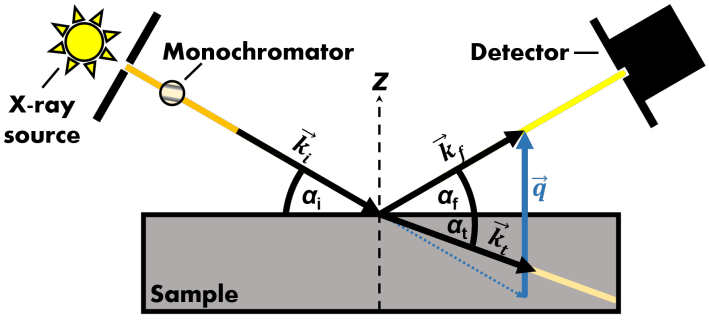

Figure 3.2: Basic scattering geometry of an XRR experiment.

3.2 X-ray reflectometry

While SAXS exploits the powder-like character of randomly oriented lipid mesophases in solution, X-ray reflectometry is a surface-sensitive method that requires highly ordered samples. From the data obtained, a vertical electron density profile with sub-Ångström resolution can be extracted. This section provides information on the basic scattering geometry, characteristic features, and the fitting procedure of XRR experiments. The explanations are based on the textbook "X-ray scattering from soft-matter thin films: materials science and basic research" by Metin Tolan [276].

An XRR measurement is the observation of the specularly reflected intensity of a monochromatic X-ray beam at an interface as a function of the angle of incidence α_i. The interface is a boundary between media with different refractive indices n, where the incident radiation with a wave vector $\boldsymbol{k}_\mathrm{i}$ splits into a reflected beam with a wave vector $\boldsymbol{k}_\mathrm{f}$ and a transmitted beam with a wave vector $\boldsymbol{k}_\mathrm{t}$. The reflected beam occurs under the angle $\alpha_\mathrm{f} = \alpha_\mathrm{i}$, while the angle of the transmitted part α_t depends on the corresponding refractive indices. The basic scattering geometry is summarized in figure 3.2.

In adequate distance to absorption edges of the sample elements, the refractive index of a homogeneous medium is given as

$$n = 1 - \frac{\lambda^2}{2\pi} r_\mathrm{e} \rho + \mathrm{i}\frac{\lambda}{4\pi}\mu = 1 - \delta + \mathrm{i}\beta \tag{3.6}$$

with the classical electron radius r_e, the electron density ρ and the linear absorption coefficient μ. It can be described by the dispersion δ and the absorption β. The objective of this section is to outline the relation between the reflectivity $R(\alpha_\mathrm{i})$ and the vertical dispersion profile $\delta(z)$ of a sample, which according to equation 3.6 is directly proportional to the electron density profile $\rho(z)$. In the X-ray regime, δ typically assumes values between 10^{-5} and 10^{-8}, while β is around one or two orders of magnitude smaller. This means that the real part of the refractive index is less or equal 1. Therefore, external total reflection occurs in the X-ray regime, whereby radiation is completely reflected below a critical angle $\alpha_\mathrm{c} \approx \sqrt{2\delta}$ when passing into an optically denser medium.

On basis of Fresnel's formulae, the reflectivity of an ideally smooth surface (the

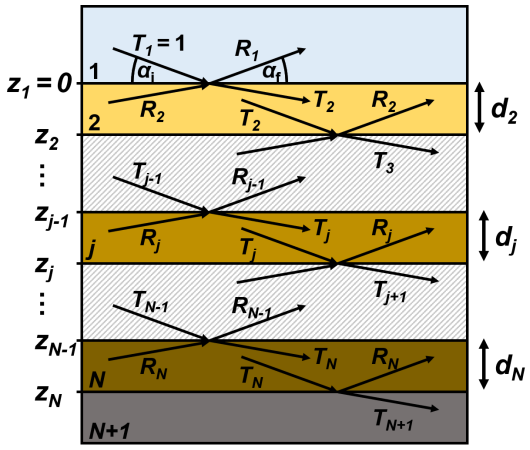

Figure 3.3: Amplitudes of transmitted T_j and reflected R_j components in XRR experiments on multilayer systems consisting of $N-1$ layers with thicknesses d_j which are separated by N interfaces at positions z_j between substrate (layer N+1) and surrounding medium (layer 1). With the Parratt algorithm, the ratios between transmitted and reflected components can be determined for every layer. Picture modified from [276].

so-called Fresnel reflectivity) can be determined as

$$R_\mathrm{F} = \frac{(\alpha_\mathrm{i} - p_+)^2 + p_-^2}{(\alpha_\mathrm{i} + p_+)^2 + p_-^2} \tag{3.7}$$

in the small angle regime with the real and imaginary part of the complex transmission angle $\alpha_\mathrm{t} = p_+ + \mathrm{i}p_-$

$$p_{+/-}^2 = \frac{1}{2}\left(\sqrt{\left(\alpha_\mathrm{i}^2 - \alpha_\mathrm{c}^2\right)^2 + 4\beta^2} \pm \left(\alpha_\mathrm{i}^2 - \alpha_\mathrm{c}^2\right)\right).$$

For $\alpha_\mathrm{i} > 3\alpha_\mathrm{c}$, this can be approximated as

$$R_\mathrm{F} \approx \left(\frac{\alpha_\mathrm{c}}{2\alpha_\mathrm{i}}\right)^4. \tag{3.8}$$

The reflectivity of a system that consists of more than one interface is given by the Parratt algorithm, which provides a phase correct summation of all reflected radiation [277]. Due to multiple reflection at the different interfaces between the substrate and the surrounding medium, phase shifts and thus interference occurs. The resulting sequences of constructive and destructive interference with varying incident angle are called Kiessig oscillations. Analogous to SAXS at crystalline structures (equation 3.1), a periodic arrangement of interfaces leads to Bragg reflections in reflectivity measurements. Figure 3.3 provides an overview of the parameters required for the mathematical description of the reflectivity of a multilayer system with N interfaces at positions z_j. The Parratt algorithm is based on the recursive layer-by-layer calculation of the ratio between the reflected and transmitted components $X_j = \frac{R_j}{T_j}$. The starting value is $X_{j+1} = 0$, because there is no reflected component in the infinitely large substrate. The recursion expression is

$$X_j = \exp^{-2\mathrm{i}k_{z,j}z_j} \frac{r_{j,j+1} + X_{j+1}\exp^{2\mathrm{i}k_{z,j+1}z_j}}{1 + r_{j,j+1}X_{j+1}\exp^{2\mathrm{i}k_{z,j+1}z_j}} \tag{3.9}$$

with the Fresnel coefficients

$$r_{j,j+1} = \frac{k_{z,j} - k_{z,j+1}}{k_{z,j} + k_{z,j+1}}, \tag{3.10}$$

where $k_{z,j} = k\sqrt{n_j^2 - \cos^2 \alpha_\mathrm{i}}$ is the z component of the wave vector in layer j.

In order to predict the reflectivities of real systems whose interfaces typically cannot be assumed to be ideally smooth, an additional parameter is required. A rough interface exhibits a lateral inhomogeneity of the height z_j of the boundary between two media that can be described with a probability density $P_j(z)$. The expected value of z regarding $P_j(z)$ is then interpreted as the position z_j of the interface. The corresponding root mean square deviation σ_j characterizes the width of the probability density function and is therefore a suitable measure of the roughness of the interface. In the framework of this thesis, the reflectivities were simulated and fitted under the assumption of Gaussian distributed interface boundaries with a probability density

$$P_j(z) = \frac{1}{\sqrt{2\pi\sigma_j^2}} \exp\left(-\frac{(z - z_j)^2}{2\sigma_j^2}\right). \tag{3.11}$$

If the thickness of the layers is large compared to the roughness of the interfaces ($d_j \gg \sigma_j$), the roughness can be incorporated into the Parratt algorithm using modified Fresnel coefficients. However, if d_j and σ_j are in the same order of magnitude, this concept leads to discontinuities in the corresponding dispersion profiles. Since this is the case for lipid systems, a different approach is discussed here. The effective density model provides an initial guess of a dispersion profile that is still based on a layer structure where every layer is defined by a thicknesses d_j, a dispersions δ_j and an absorption β_j and every interface by a roughness σ_j. A continuous transition between the layers is implemented by an odd function $Y_j(z)$, which is ± 1 for $z \to \pm\infty$. In this work $Y_j(z) = \mathrm{erf}\left(\frac{z}{\sqrt{2}\sigma_j}\right)$ is used. With the connection points

$$\zeta_j = \frac{\sigma_j z_{j-1} + \sigma_{j-1} z_j}{\sigma_j + \sigma_{j-1}} \tag{3.12}$$

the fraction of material j at position z can be determined as

$$W_j(z) = \begin{cases} \frac{1}{2}\left(1 + Y_j(z - z_j)\right) & \text{for } z \leq \zeta_j \\ \frac{1}{2}\left(1 - Y_j(z - z_{j-1})\right) & \text{for } z > \zeta_j. \end{cases} \tag{3.13}$$

This results in the following dispersion profile

$$\delta(z) = \left(\sum_{j=1}^{N+1} \delta_j W_j(z)\right) \Bigg/ \left(\sum_{j=1}^{N+1} W_j(z)\right). \tag{3.14}$$

In analogy, the absorption can be calculated for each point. The layer system is then sliced into thin smooth layers to which the Parratt algorithm 3.2 can be applied. To

extract a dispersion profile based on an XRR pattern, the parameters of the model are varied minimizing the deviation between calculated and measured reflectivity.

The electron density of lipid monolayers was modelled by two sublayers representing the head- and the tailgroup. In chapter 5, the formation of adsorbate layers at Langmuir films was taken into account by adding another layer below the headgroups. For the simulation of bilayers, a sublayer was introduced to describe the gap of the electron density between adjacent tailgroups in addition to the two head- and two tailgroup sublayers. In multi-lamellar lipid structures, the bilayers are separated by water layers, so that the repeat unit has to be modeled by a total of six sublayers. In chapter 6, a periodic repetition of a symmetric bilayer was used to simulate the structure of solid-supported multilayers.

3.3 Grazing incidence diffraction

The lateral structure of Langmuir films was determined by grazing incidence diffraction. This method exploits the low penetration depth ($\sim 5\,\mathrm{nm}$) of a monochromatic X-ray beam into a substrate when the angle of incidence is below the critical angle ($\alpha_\mathrm{i} \approx 0.8{\cdot}\alpha_\mathrm{c}$) to achieve high surface sensitivity. The resulting scattering patterns provide information on the lateral organization of lipid monolayers and lattice vectors, mean crystallite sizes, and tilt angles of the tailgroups can be determined. The basic scattering geometry of a GID experiment is presented in figure 3.4. In this geometry, the momentum transfer of elastic scattering is given by

$$\boldsymbol{q} = \frac{2\pi}{\lambda} \begin{pmatrix} \cos\alpha_\mathrm{f}\cos(2\theta) - \cos\alpha_\mathrm{i} \\ \cos\alpha_\mathrm{i}\sin(2\theta) \\ \sin\alpha_\mathrm{i} + \sin\alpha_\mathrm{f} \end{pmatrix} \tag{3.15}$$

with a constant incident angle α_i and the vertical and horizontal scattering angles α_f and 2θ. As $\alpha_\mathrm{i} \approx 0$ and $\alpha_\mathrm{f} \approx 0$, the horizontal component of the wave vector transfer can typically be written as

$$q_\parallel \approx \frac{4\pi}{\lambda}\sin\theta. \tag{3.16}$$

Figure 3.5 illustrates the alignment of lipids in a compressed monolayer at the air-water interface. The objective of this section is to demonstrate how the specified parameters can be determined from a measured GID pattern. The structure is defined by lattice vectors $\boldsymbol{a}$ and $\boldsymbol{b}$, which include the angle γ, and a tilt angle τ of the lipid tail in a direction given by ψ, which is the angle between $\boldsymbol{a}$ and the projection of the lipid tail on the water surface. Without restriction of the generality, the lattice vectors can be written as

$$\boldsymbol{a} = a\begin{pmatrix}1\\0\\0\end{pmatrix} \qquad\qquad \boldsymbol{b} = b\begin{pmatrix}\cos\gamma\\\sin\gamma\\0\end{pmatrix}. \tag{3.17}$$

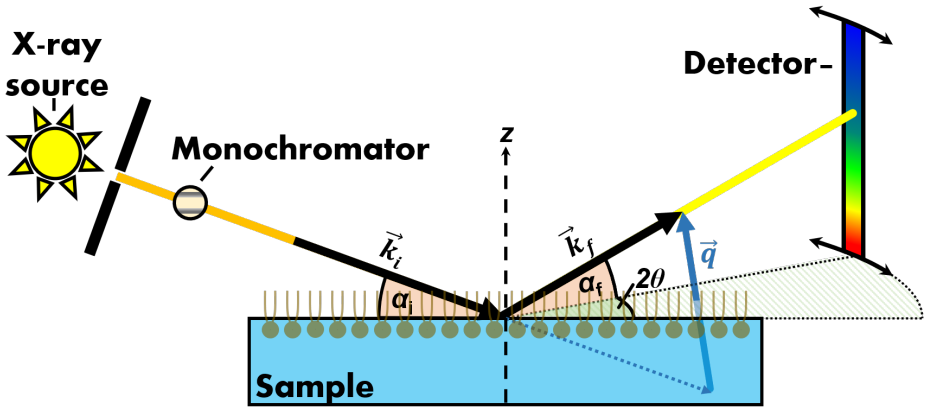

Figure 3.4: Basic scattering geometry of a GID experiment.

However, the description of the unit cell, which is determined by the electron density distribution of a lipid, is more complex. Here, we treat the molecules as rod-shaped objects of a length l whose orientation is given by τ and ψ. The tilt is now introduced into the mathematical consideration by defining a third lattice vector

$$\boldsymbol{l} = l \begin{pmatrix} \sin\tau\cos\psi \\ \sin\tau\sin\psi \\ \cos\tau \end{pmatrix}. \tag{3.18}$$

Then, the reciprocal lattice vectors are given by

$$\boldsymbol{g_a} = 2\pi \frac{\boldsymbol{b}\times\boldsymbol{l}}{|\boldsymbol{a}(\boldsymbol{b}\times\boldsymbol{l})|} \tag{3.19}$$

by cyclic permutations of $\boldsymbol{a}$, $\boldsymbol{b}$ and $\boldsymbol{l}$. According to the von Laue condition 3.2, these define the scattering vectors where Bragg reflections can occur. It must be noted that there is no periodic structure in vertical direction, so that in this case the von Laue condition is only fulfilled for

$$G_{hk} = h\boldsymbol{g_a} + k\boldsymbol{g_b}. \tag{3.20}$$

However, the additional lattice vector $\boldsymbol{l}$ leads to a tilting of the lattice planes that affects especially the z component of the resulting reciprocal lattice vectors

$$\boldsymbol{g_a} = \frac{2\pi}{a\sin\gamma}\begin{pmatrix} \sin\gamma \\ -\arctan\gamma \\ -\sin(\gamma-\psi)\tan\tau \end{pmatrix} \qquad \boldsymbol{g_b} = \frac{2\pi}{b\sin\gamma}\begin{pmatrix} 0 \\ 1 \\ -\sin\psi\tan\tau \end{pmatrix}. \tag{3.21}$$

Therefore, Bragg reflections are expected at

$$\begin{aligned} q_{z,hk} &= -\frac{2\pi}{ab\sin\gamma}\left(hb\sin(\gamma-\psi) + ka\sin\psi\right)\tan\gamma \\ q_{\parallel,hk} &= \frac{2\pi}{ab\sin\gamma}\left|h\boldsymbol{b} - k\boldsymbol{a}\right|. \end{aligned} \tag{3.22}$$

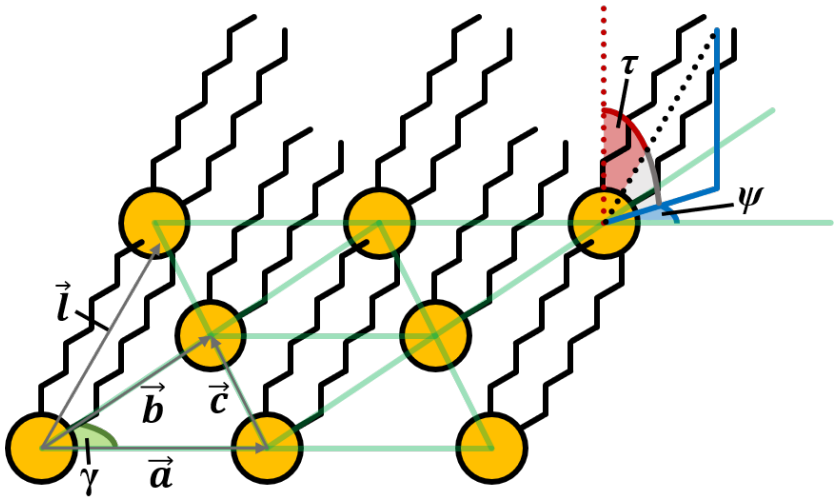

Figure 3.5: Illustration of the parameters of a compressed lipid film that can be determined via GID. The vectors $\boldsymbol{a}$, $\boldsymbol{b}$ and $\boldsymbol{c}$ and the angle γ describe the two dimensional lattice. The length and orientation of the alkyl chains is represented by the vector $\boldsymbol{l}$. The tilt of the molecules is specified by the angles τ and ψ.

Based on these equations, all stated parameters can be determined from the positions of the Bragg reflections that occur at the lowest horizontal scattering angles. The corresponding lattice planes have the Miller indices (1,0), ($\bar{1}$,0), (0,1), (0,$\bar{1}$), (1,$\bar{1}$) and ($\bar{1}$,1). Lattice planes with h,k-pairs with opposite signs yield the same horizontal scattering angle, while their vertical scattering angles also have opposite signs. As the water surface shades reflections with negative q_z values, only one of the corresponding reflections is observed or they overlap at $q_z = 0$. Therefore, a maximum of three distinguishable reflexes are observed. For their scattering vectors, new designations are introduced. We define

$$\begin{aligned} q_{\parallel,a} &= q_{\parallel,10} & q_{z,a} &= |q_{z,10}| \\ q_{\parallel,b} &= q_{\parallel,01} & q_{z,b} &= |q_{z,01}| \\ q_{\parallel,c} &= q_{\parallel,1\bar{1}} & q_{z,c} &= |q_{z,1\bar{1}}| \end{aligned} \tag{3.23}$$

with the convention $q_{\parallel,a} \geq q_{\parallel,b} \geq q_{\parallel,c}$. The tilt angles can then be determined as

$$\psi = \arctan\left(\frac{\sin\gamma}{\cos\gamma + \frac{q_{z,a}q_{\parallel b}}{q_{z,b}q_{\parallel a}}}\right) \tag{3.24}$$

$$\tau = \arctan\left(\frac{q_{z,b}}{q_{\parallel b}\sin\psi}\right). \tag{3.25}$$

Up to this point, only the positions of maximum scattering intensity were determined. However, due to the lack of restriction of the scattering vector perpendicular

to the 2D crystal, the Bragg reflections are continuous rods, so-called Bragg rods, in this scenario. Therefore, the vertical scattering will now be discussed in more detail. A detailed description of the Bragg rods can be obtained by an explicit determination of the form factor

$$f(\boldsymbol{q}) = \int_{\text{unit cell}} d\boldsymbol{r}\ \rho_{\text{e}}(r)\ \mathrm{e}^{-\mathrm{i}\boldsymbol{q}\boldsymbol{r}}. \tag{3.26}$$

Besides the form factor, the scattering intensity is defined by the transmission functions of the incident and the scattered wave t_{i} and t_{f} and a Debye-Waller-like roughness term. It can be written as

$$I(\boldsymbol{q}) \propto |t_{\text{i}}(\alpha_{\text{i}})|^2\ |f(\boldsymbol{q})|^2\ |t_{\text{f}}(\alpha_{\text{f}})|^2\ \mathrm{e}^{-q_z^2\sigma^2} \tag{3.27}$$

with the surface roughness σ. Since α_{i} is constant, an explicit specification of $t_{\text{i}}(\alpha_{\text{i}})$ is not necessary to model the relative intensity distribution. The transmission function of the scattered wave describes the Yoneda or Vineyard peak [278, 279] that originates from the maximum of the transmission coefficient at the critical angle and is given by

$$t_{\text{f}}(\alpha_{\text{f}}) = \frac{2\sin\alpha_{\text{f}}}{\sin\alpha_{\text{f}} + \sqrt{n^2 - \cos^2\alpha_{\text{f}}}}. \tag{3.28}$$

The form factor will be approximated by a cylinder with homogeneous electron density. In a rotated coordinate system with the transformed coordinates q_z' and $q_{\|}'$ which is set with the cylinder axis pointing in direction of q_z', the form factor separates into a q_z'- and a $q_{\|}'$-dependent component and the following relation can be found

$$f(\boldsymbol{q}') = F_1(q_z')\ F_2(q_{\|}') \propto \frac{\sin\left(\frac{q_z' L}{2}\right)}{q_z'}. \tag{3.29}$$

The transformation is given by

$$q_z' = q_z\cos\tau - q_{\|}\sin\psi^*\sin\tau \tag{3.30}$$

with $q_{\|}\sin\psi^*$ being the projection of the the parallel wave vector transfer $q_{\|}$ into a plane perpendicular to the rotation axis.

In the framework of this thesis, the function

$$I(q_z') = C_1\ |t_{\text{f}}(q_z')|^2\ \left|\frac{\sin\left(\frac{q_z' L}{2}\right)}{q_z'}\right|^2 + C_2 \tag{3.31}$$

with a constant of proportionality C_1 and an offset C_2 was used to model the measured Bragg rods. The surface roughness term was neglected, as it has only minor effects on the scattering in the low q_z regime [280].

Along $q_{\|}$, the Bragg rods can be modeled with a Lorentzian distribution. As shown in equation 3.22, the maxima provide information about the lattice constants of a Langmuir

film. Furthermore, the Scherrer equation [281, 282] provides a relation between the full width at half maximum FWHM_{hk} of a Bragg rod in radian measure and the mean crystallite size

$$L_{hk} = \frac{0.9\lambda}{\mathrm{FWHM}_{hk} \cos\theta_{hk}}. \tag{3.32}$$

3.4 High hydrostatic pressure sample cells

The application of high hydrostatic pressure was achieved using the high pressure XRR cell described by Wirkert et al. [283] and the high pressure SAXS cell described by Krywka et al. [284] that allow experiments at pressures of up to 5 kbar. The two cells are depicted in figures 3.6 and 3.7. In both constructions, pressure transmitting liquid and sample liquid are separated to ensure a clean and controlled sample environment. The outer cells are designed similarly and consist of blocks of high strength stainless steel with five openings pointing to the center. Two of them are the entry and exit points for the beam in X-ray scattering experiments and are sealed with Poulter-type [285] diamond windows. The apertures have a diameter of 2 mm. The sample port is aligned perpendicularly to the beam direction. The two remaining holes are terminals for high pressure tubes that connect the cell to a pump and pressure gauges. In addition, there is a channel system running through the pressure cells that is not connected to the sample area. Through this, a liquid can circulate to regulate the temperature.

The inner sample cell of the XRR pressure cell offers space for a wafer measuring $7.6 \times 7.6\,\mathrm{mm}^2$. The wafer is fixed with a screw in a sample holder that is mounted in a steel casing. The casing has openings for the X-ray beam that are sealed with Kapton foil. The opening for the sample holder is closed with a screw cap. The screw cap has a hole in the center that is sealed with a flexible membrane transmitting the pressure into the sample cell. The filling volume of the XRR sample cell is approximately 300 µL.

The design of the inner sample cell for SAXS experiments is much simpler. Again, the sample volume is separated by Kapton foil. However, in this case, no additional membrane is needed to transmit the pressure into the inner sample cell as the size of the Kapton windows is large compared to the thickness of the cell. Therefore, the pressure can be transferred directly via the foil without it being exposed to too much strain. The cell can be filled with a syringe. The corresponding opening is sealed with a Teflon screw. The filling volume of the inner SAXS cell is approximately 40 µL.

To ensure sufficient flux through the liquid phase and the diamond windows, X-ray sources that provide radiation with high photon energies and high intensities are required for high pressure studies. Therefore, the experiments involving high hydrostatic pressure were performed at synchrotron facilities.

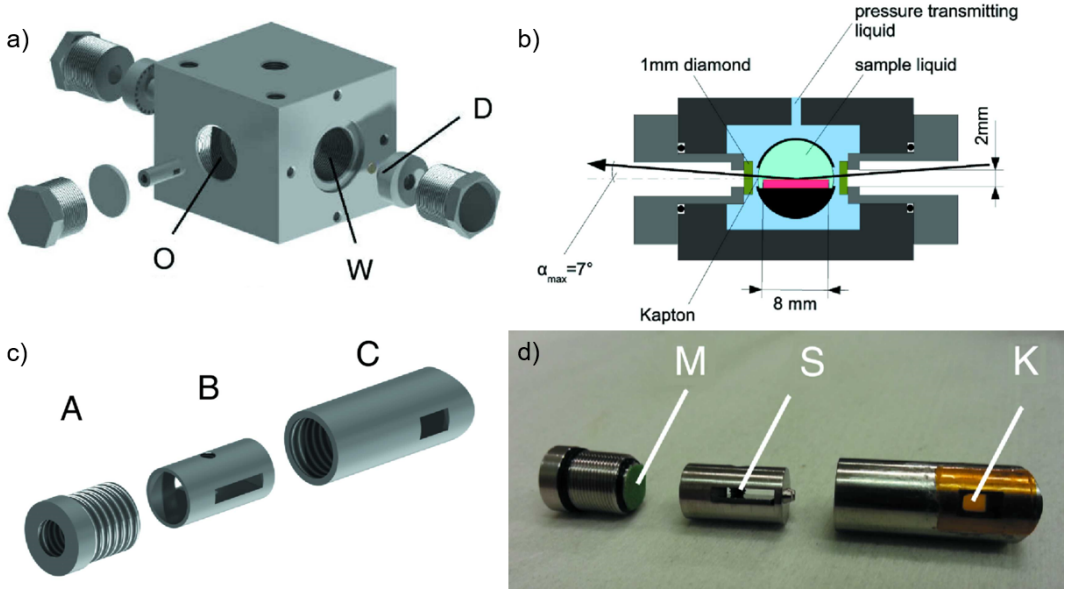

Figure 3.6: a) Sketch of the high hydrostatic pressure XRR sample cell with an opening (O) for the sample and windows (W) sealed by diamonds (D) along the beam path. b) Cross sectional drawing of the beam path through the sample cell. The wafer is shown in red. c) Design of the inner sample cell consisting of a screw cap (A), a sample holder (B) and a casing (C). d) Photo of the inner sample cell showing the flexible membrane (M), the grub screw (S) that fixes the wafer and the Kapton windows (K). Reproduced from [283] with permission of the International Union of Crystallography.

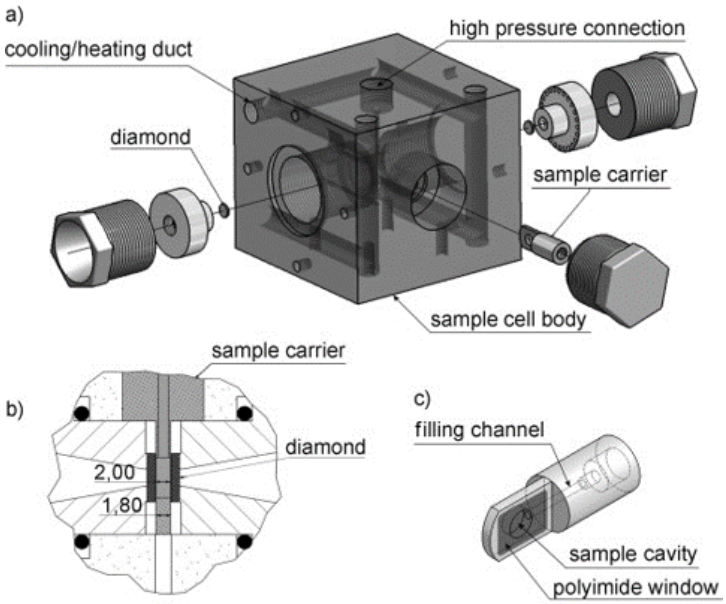

Figure 3.7: a) Sketch of the high hydrostatic pressure SAXS sample cell. b) Cross sectional drawing of the inner sample cell mounted between the diamond windows. c) Sketch of the inner sample cell. Reprinted with permission from [284]. Copyright © 2008 WILEY-VCH Verlag GmbH & Co. KGaA, Weinheim.

Chapter 4

The effect of additives on the lamellar-to-cubic transition dynamics of monoolein at excess water conditions

4.1 Objective

In this study, we took advantage of the unique properties of monoolein [76] to investigate how different additives affect hydration and curvature of remodeling lipid structures. Many cellular membrane processes involve events of fusion and fission and thus drastic changes of the membrane curvature and the hydration state [36, 88, 89, 92, 286]. These processes are subject to various influencing factors, which often include interactions with proteins and solutes. An obvious example is viral membrane fusion that is facilitated by viral envelope proteins and the insertion of fusogenic peptides into the target membrane [33–35, 42]. But also osmolytes and crowding agents can play an important role in fusion events as they, e.g., can promote dehydration of inter-bilayer spaces [26, 105]. In this study, the influence of fusogenic peptides, TMAO, urea, sucrose, and PEG on the equilibration dynamics of monoolein in excess water after a pressure-jump across the boundary between lamellar and cubic phase is explored. When the hydrostatic pressure is abruptly released in the lamellar regime, the cubic phase forms with a lattice constant that is increased compared to equilibrium and that slowly decreases with time, as excess water is released from the lipid structures. SAXS was applied to monitor the time-dependence of this process and to examine the influence of additives.

4.2 Sample preparation

The SAXS pressure-jump experiments were conducted in the high hydrostatic pressure XRR cell that was introduced in chapter 3.4. The XRR cell was chosen because of

the large inner cells, which are easier to fill with highly viscous samples such as monoolein/water mixtures than the inner cells of the high hydrostatic pressure SAXS cell. Monoolein (Sigma Aldrich) and buffer solution were poured into the inner sample cell and mixed mechanically. Then, the cell was sealed and allowed to equilibrate for at least 12 hours. The buffer solution was 10 mM BisTris (Sigma Aldrich) buffer at pH 5 or 7 and was added in concentrations of 80 or 90 wt%, depending on the sample system. The additives were dissolved in the buffer solution before it was mixed with monoolein. The concentrations were 2 wt% for the fusogenic peptides (GeneCust, > 90 % purity), 1 M for urea (Sigma Aldrich), TMAO (Sigma Aldrich) and sucrose (Sigma Aldrich), 0.67 M urea and 0.33 M TMAO for mixtures of both solutes, and 150 g/L for PEG of molecular weights between 200 and 35000 g/mol (Sigma Aldrich).

4.3 Experimental setup

The SAXS measurements were conducted at beamlines BL2 [154, 155] and BL9 [156] of DELTA (Dortmund, Germany) with photon energies of 12 keV ($\lambda = 1.033$ Å) and 13 keV ($\lambda = 0.954$ Å). BL2 is a bending magnet beamline that originally operated with white beam. However, it was lately equipped with a Pd-B_4C-multilayer monochromator with an energy resolution $\Delta E/E$ of 1.5 % to enable diffraction measurements. At BL2 and BL9, the SAXS patterns were captured with a MAR345 image plate detector. The beamsize was set to 0.5 × 0.5 mm^2 at BL2 and to 1 × 1 mm^2 at BL9 by slit systems. For the calibration of the setups, silver behenate [287] was used. Pressure-jumps across the lamellar-to-cubic phase boundary were typically performed from 1000 bar to 50 bar. The reduction of pressure took about 10 s. In presence of the fusogenic peptides HA2-FP and TBEV-FL, also pressure-jumps in the opposite direction from 50 to 1500 bar were conducted to examine their effects on the cubic-to-lamellar transition. All measurements were performed at 25 °C. The experimental setup at BL2 is shown in figure 4.1.

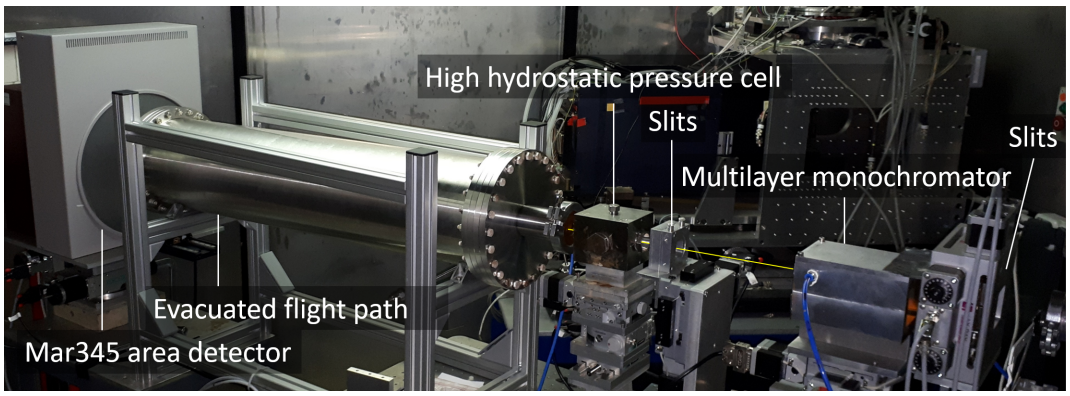

Figure 4.1: The high hydrostatic pressure SAXS setup at BL2. The beam path is shown in *yellow*.

4.4 Measuring procedure and data treatment

Figure 4.2 shows the first steps of data processing for a SAXS pattern of monoolein in the Pn3m phase at 50 bar. The black shadow that extends from the bottom of the picture to the center is caused by a lead beam stop that was used to block the primary beam. The area around the beamstop was masked, before the detector image was integrated azimuthally to obtain the intensity as a function of q. From the integrated data, an interpolated background was subtracted. As discussed in chapter 3.1, conclusions about the phase behavior can be drawn from the positions of the occurring Bragg reflections. The scattering intensity as a function of the wave vector transfer was fitted using Gaussian distributions to determine the lattice constants. For cubic phases, the first seven reflections were considered, for lamellar phases, the first four at most. The height and width of the maxima were adjusted by two independent fit parameters for each reflection. The positions of all maxima corresponding to the same phase were fitted in a fixed ratio based on only the lattice constant a as fit parameter. The ratios were set according to the characteristic ratios of the positions of Bragg reflections stated in table 3.1 of chapter 3.1. The position of the n-th Bragg reflection q_n is then given as

$$q_n = \frac{2\pi}{a}\sqrt{h_n^2 + k_n^2 + l_n^2} \tag{4.1}$$

with h_n,k_n,l_n specifying the corresponding lattice planes.

Figure 4.3 a shows the pressure-dependent behavior of monoolein in 80 wt% water at 25 °C. The identification of the occurring phases is demonstrated in figure 4.3 c. It can be seen that the phase behavior observed upon pressurization differs from the phase behavior observed upon pressure release. When the pressure was increased, the phase transition from cubic Pn3m to lamellar occurred at 2.5 kbar. As further pressurization hardly affected the spacing of the lamellar phase, it can be identified as a lamellar crystalline phase. When the pressure was decreased again, a transition into a lamellar phase with a slightly higher spacing was observed. This phase also showed only a very low compressibility. Additional measurements revealed that the lamellar phase with the

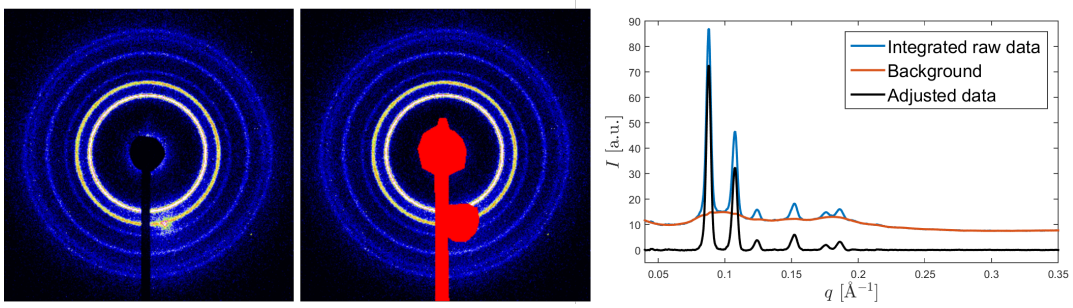

Figure 4.2: SAXS intensity of monoolein in the Pn3m phase at 50 bar shown as a raw 2D detector image (*left*), after masking the beam stop (*center*) and as a function of q after azimuthal integration (*right*). The area which was also masked on the right of the beam stop is the center of rotation of the MAR345 image plate detector.

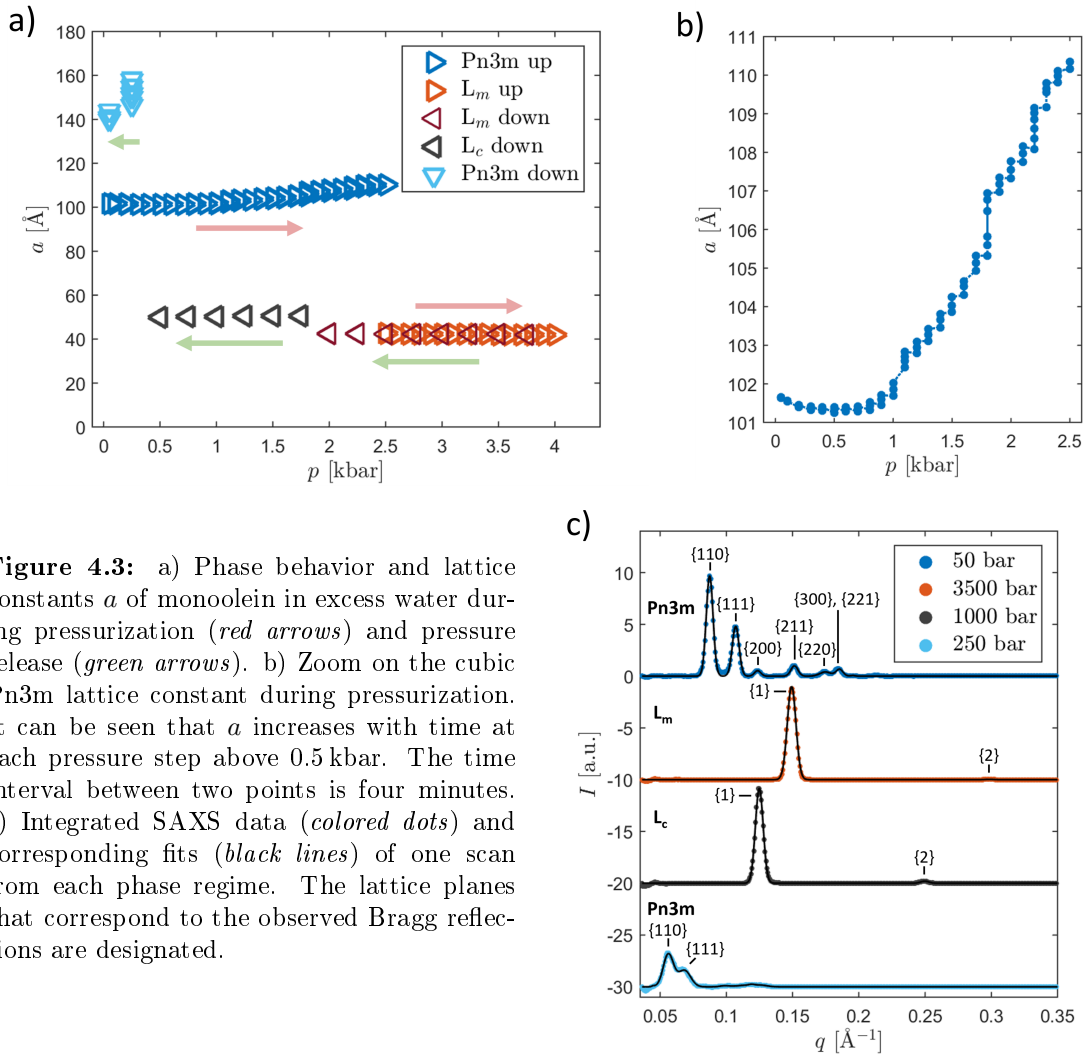

Figure 4.3: a) Phase behavior and lattice constants a of monoolein in excess water during pressurization (*red arrows*) and pressure release (*green arrows*). b) Zoom on the cubic Pn3m lattice constant during pressurization. It can be seen that a increases with time at each pressure step above 0.5 kbar. The time interval between two points is four minutes. c) Integrated SAXS data (*colored dots*) and corresponding fits (*black lines*) of one scan from each phase regime. The lattice planes that correspond to the observed Bragg reflections are designated.

lower spacing is not stable and that the transition into the lamellar phase with the larger spacing also happens without pressure release after several hours. The observation of a metastable phase with a spacing of approximately 43 Å and a stable crystalline phase with a spacing of approximately 50 Å is in good agreement with the behavior of monoolein found at low temperatures [77, 288] and was already observed upon pressurization at 7.5 °C [289]. In the following, the metastable phase will be referred to as L_m phase and the stable phase as L_c phase. Upon pressure release, the lamellar-to-cubic transition occurred below 0.5 kbar. At this point, the Pn3m phase forms again with an increased lattice constant that shrinks with time. The time difference between two data points in figure 4.3 a is approximately four minutes.

A closer look at the cubic lattice constant during the pressure increase provided in figure 4.3 b shows that the system was not in equilibrium above 0.5 kbar. At each

pressure, three to six SAXS patterns were taken at four minute intervals and it can clearly be seen that the lattice constant slowly increased with time in the corresponding pressure range. Additional measurements proved that the increase of the lattice constant continues over many hours and finally culminates in a phase transition into the L_c phase (see section 4.7, figure 4.24).

Based on the discussed observations, the following measuring procedure was established for the investigation of the dynamics after a lamellar-to-cubic phase transition. First, a SAXS pattern was captured at 50 bar with an exposure time of 150 s to obtain an equilibrium value of the Pn3m lattice constant at this pressure. Then, the pressure was increased to 3.5 kbar to ensure a fast transition into the lamellar L_m phase. After this, the pressure was decreased to 1000 bar, since it was found that the pressure reduction reliably causes an immediate transition from the L_m to the L_c phase. To monitor this process, SAXS patterns were taken at both pressures. As the Bragg reflections of the lamellar phases are more pronounced, exposure times of 30 s were found to be sufficient for this purpose. From this stable starting point, a pressure-jump was performed down to 50 bar. Immediately after this value was reached, repetitive SAXS measurements with exposure times of 150 s were conducted over several hours. As the readout time of the detector is 90 s, the time step between each measurement was four minutes. After the pressure-jump, Pn3m domains with different lattice constants can coexist temporally. In this case, the mean values of the lattice constants weighted with the area under the first two reflections corresponding to each domain were determined.

Selected integrated SAXS patterns of different samples with the obtained fits are presented in appendix A.1.

4.5 Urea, TMAO and sucrose

In this section, the results of the pressure-jump study on monoolein in presence of urea, TMAO and sucrose are presented. The experiments were conducted at pH 7 and a water content of 90 wt%. Figure 4.4 shows the Pn3m lattice constants of all samples at 50 bar before pressurization. The mean value for monoolein in absence of osmolytes was 105 Å. In accordance with existing knowledge, TMAO and sucrose decreased the lattice parameter as they displace water from lipid structures, while urea increased the lattice parameter as it promotes lipid structures with large headgroup areas [26, 71, 242]. Moreover, the effects of urea and TMAO on the lattice constant compensated each other when they were mixed in the characteristic 2:1 ratio [239]. TMAO in a concentration of 1 M reduced the lattice constant by about 8 Å, sucrose by 12 Å. The data points for urea strongly deviated from the mean value. As will be seen below, urea strongly slows down the equilibration process after a pressure-jump. Therefore, it is likely that the waiting time of 12 h between sample preparation and experiment is not sufficient to reach equilibrium for urea samples. From the convergence of the lattice parameter after a pressure-jump (figure 4.6), the actual equilibrium lattice constant of monoolein in buffer solution containing 1 M urea is estimated to be approximately 110 Å. The mean values of the lattice parameter of monoolein in presence and absence of urea and TMAO in a

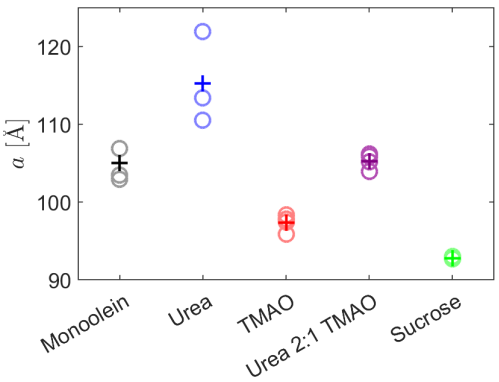

Figure 4.4: Equilibrium values of the Pn3m lattice constant of monoolein at 50 bar in presence of different osmolytes. The *circles* represent the values for different samples to illustrate the variance. The *crosses* mark the mean values.

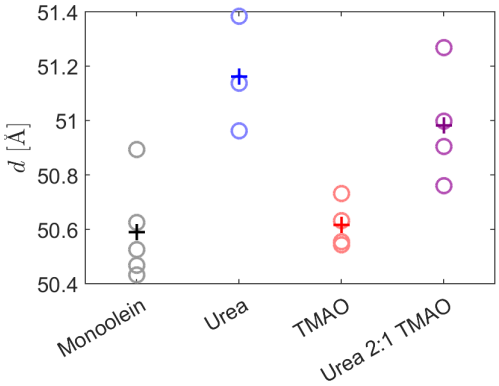

Figure 4.5: Spacing of the L_c phase of monoolein at 1000 bar in presence of different osmolytes. The *circles* represent the values for different samples to illustrate the variance. The *crosses* mark the mean values.

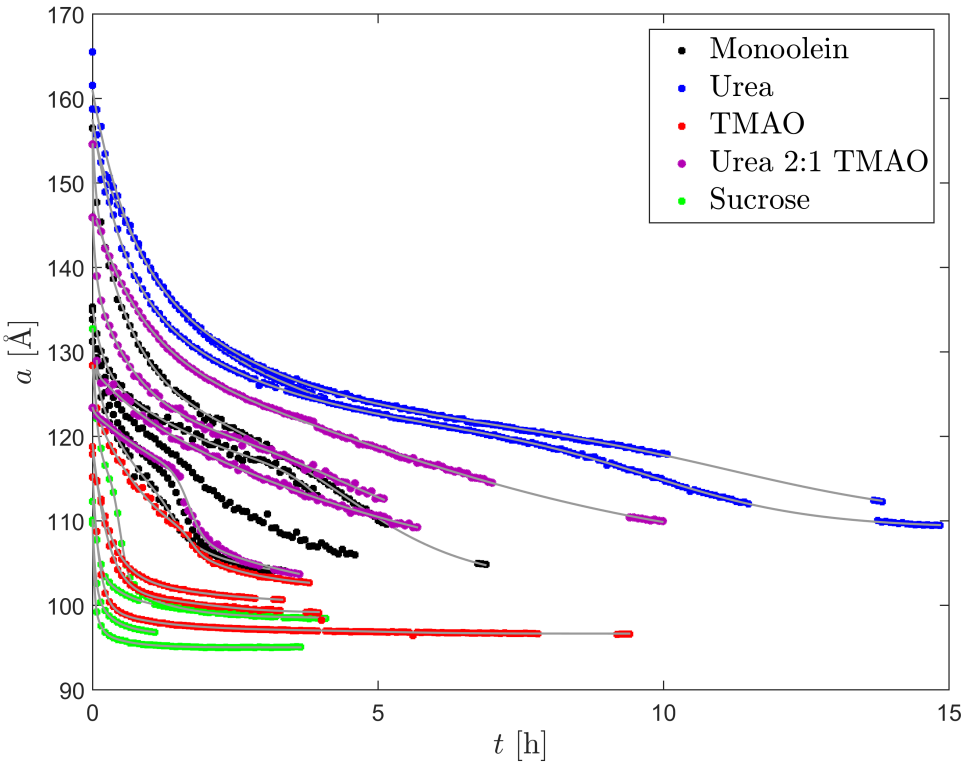

Figure 4.6: Decrease of the Pn3m lattice constant of monoolein after a pressure-induced lamellar-to-cubic transition in presence of urea, TMAO and sucrose (*colored dots*) and fits (*gray lines*).

2:1 ratio differ by 0.3 Å, which is less than the observed variance between the individual samples.

Figure 4.5 shows the lamellar spacing of the L_c phase at 1000 bar before the pressure-jump. The spacing was hardly affected by urea and TMAO as the observed values deviate from each other by less than 1 Å. However, the urea-containing samples showed a slight increase of spacing. By estimating the water content of the lamellar structure based on the excess water boundary of 4 wt% given by Qiu and Caffrey [77], the thickness of the hydrated inter-bilayer space can be determined to be approximately 2 Å. This means that all water molecules in the hydration layer are in close proximity to the headgroups and therefore have limited mobility [290]. Presumably, a lack of free hydration water is the reason why we did not observe a displacement of water molecules induced by TMAO. Such a displacement would be reflected in a reduced spacing. The increase of spacing caused by urea can be explained by its affinity to reside at lowly hydrated membrane interfaces [28, 30]. The effect on the spacing was more pronounced for the samples with 1 M urea compared to the urea/TMAO mixtures that contained 0.67 M urea. In the case of sucrose, the lamellar phase was found to be unstable at 1000 bar. Therefore, the pressure-jump to 50 bar was performed from a starting pressure of 2000 bar. However, at this pressure, monoolein remained in the metastable L_m phase. The mean value of the spacing in presence of 1 M sucrose was 42.8 Å.

Figure 4.6 shows the decrease of the lattice constant after a pressure-jump across the lamellar-to-cubic phase boundary of monoolein with and without osmolytes as a function of time. The speed of the water release from the cubic structure strongly varied upon the addition of the different osmolytes. While the lattice constant still reduced after more than ten hours in presence of urea, the system was close to equilibrium after only one hour in presence of TMAO and sucrose.

In order to determine how the growth process of the Pn3m crystallites and their mean size was affected by the additives, the intensity and width of the reflections were analyzed. As the reflections shift due to the decrease of the lattice constant, they appear broader and less intense. Therefore, their intensity was compared based on the integral over the first two Pn3m reflections instead of their maximum values. Figure 4.7 shows the integrated intensities as a function of time. It can be seen that the formation of the Pn3m structures was much faster than the equilibration of the lattice parameter for all samples, as the integrated intensity increased to a constant level in less than one hour in all cases. For TMAO and sucrose, the maximum was already reached after the first measurement, indicating that the formation of the Pn3m structures is completed after less than four minutes. In case of pure monoolein, it is difficult to estimate the time scale, as the data points strongly fluctuate. However, the initial increase of the intensity happened mostly in the first 15 minutes. For urea, two of the samples showed an increase only during the first 10 to 15 minutes, while the intensity rose for 40 minutes in case of the third sample. In presence of urea and TMAO in a 2:1 ratio, the convergence to the maximum value took approximately half an hour. Since the equilibration of the integrated intensity was much faster than the dynamics of the lattice constant in all cases, it is reasonable to assume that the number of lipids in the Pn3m crystallites is mostly constant during the shrinking process.

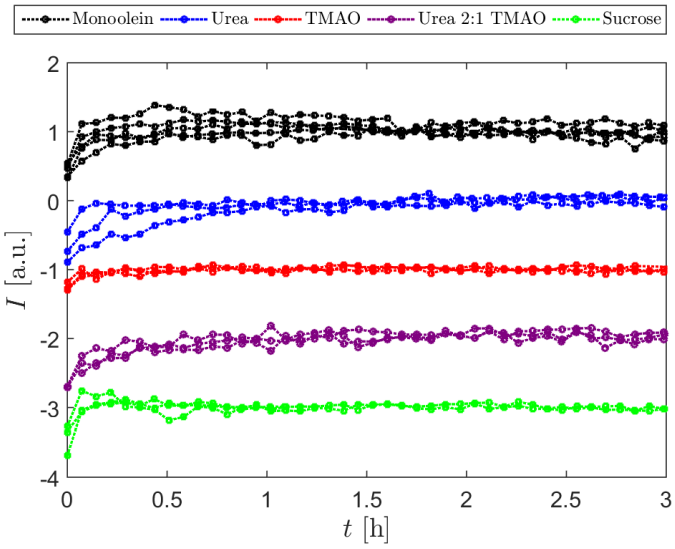

Figure 4.7: Time-dependence of the integrated intensity of the first two Pn3m Bragg reflections of monoolein in presence of different osmolytes after a pressure-jump. The integrated intensities were normalized to their temporal mean values and vertically shifted for clarity.

The size of crystallites is directly connected to the width of the corresponding Bragg reflections. As mentioned above, in this experiment, the reflections broaden as they shift during the exposure time. For a rough comparison, the FWHM of the first Pn3m reflections of different samples was determined in time ranges with an almost constant lattice constant. For the two pure monoolein samples with the fastest decrease, the mean values of the FWHM during the last hour were 0.0039 $Å^{-1}$ and 0.0041 $Å^{-1}$. After more than three hours, the reflections of the TMAO sample that was measured for the longest time had an average width of 0.0040 $Å^{-1}$. In the plateau area between four and seven hours after the pressure-jump, the two urea samples exhibited FWHMs of 0.0040 $Å^{-1}$ and 0.0041 $Å^{-1}$. The mean value of the FWHM of monoolein in presence of urea and TMAO in a 2:1 ratio after more than nine hours was 0.0042 $Å^{-1}$. For the two sucrose samples that were measured for the longest time, the average widths after more than two hours were 0.0040 $Å^{-1}$ and 0.0045 $Å^{-1}$. For none of the osmolytes, the FWHM strongly differed from the value of pure monoolein. It can be concluded that the presence of the osmolytes has only a minor effect on the mean size of monoolein Pn3m crystallites. Considering the experimental resolution, which is limited in particular by the length of the sample of 1 cm and the resolution of the incident energy, a mean crystallite size of approximately 2000 Å can be estimated from the observed FWHMs.

The analysis of the intensity and width of the reflections revealed that the growth of the lipid structures after a pressure-jump was typically completed after a few minutes and that the resulting lipid structures had comparable sizes in all samples. Therefore, the different time scales of the equilibration of the lattice constants of monoolein in presence of different osmolytes (figure 4.6) cannot be attributed to differences of the shape or growth process of the Pn3m phase. Instead, for all samples, a water release from Pn3m structures with similar sizes which consist of an almost constant amount of lipids was observed. In absence of additives, this process is driven by the effort of

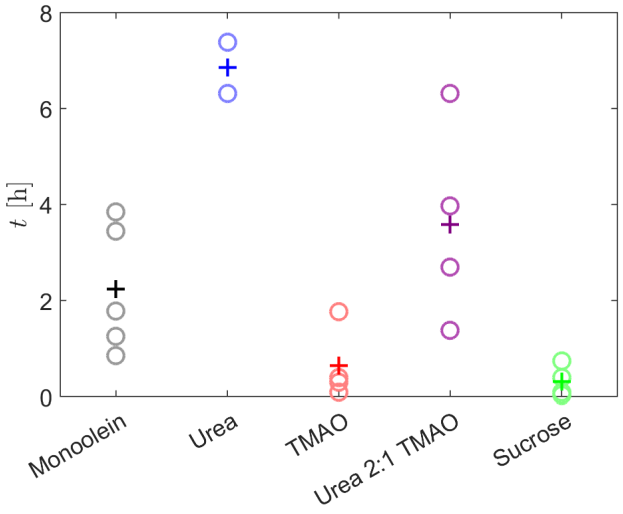

Figure 4.8: Required time t for the lattice constant to fall below 110 % of the equilibrium value after pressure-jumps in presence of osmolytes. Except for urea, the mean values shown in figure 4.4 were taken as equilibrium lattice constants. In case of urea, the equilibrium value was estimated based on figure 4.6 to be roughly 110 Å. The *circles* represent the values for different samples to illustrate the variance. The *crosses* mark the mean values.

the lipid leaflets to approach a certain curvature which is mostly defined by the space requirement of the hydrocarbon chains.

In figure 4.8, the speed of the equilibration processes is compared based on the time that elapsed after the pressure-jump until the lattice constant decreased under 110 % of the equilibrium value. For this purpose, a continuous and smoothed representation of the data was generated. It was found that the data can be reproduced accurately with a superposition of two exponential functions and a hyperbolic tangent. As the speed of the reduction of the lattice constant typically slows down with time, the course of the data can mostly be described with exponential functions. However, for pure monoolein and the urea containing samples, an increase of the speed occurred between 120 and 110 Å. This feature was taken into account by the hyperbolic tangent. The obtained fits are shown in figure 4.6. The mean values from figure 4.4 were taken as equilibrium values for all samples except for the urea samples. As discussed above, for urea, the observed values are assumed to be too high due to the slow equilibration dynamics of the system. Therefore, an equilibrium value of 110 Å was estimated based on the course of the lattice constant as a function of time in figure 4.6.

For pure monoolein, 110 % of the equilibrium lattice constant were reached between 50 minutes and 4 hours after the pressure-jump. The mean value was slightly more than two hours. In presence of urea, this value increased to almost seven hours. Hence, the interactions of urea molecules with the headgroups do not only shift the equilibrium value of the lattice constant, but also stabilize structures with even lower negative curvature and thus larger headgroup areas, so that the water release from the Pn3m structures is slowed down. Due to the *osmophobic effect*, TMAO and sucrose molecules are displaced from lipid structures. This results in a concentration gradient and therefore an osmotic pressure between the hydration water and the excess water that accelerates the water release. For TMAO, 110 % of the equilibrium lattice constant were reached after approximately 40 minutes and for sucrose, after approximately 20 minutes. When

urea and TMAO were added in a 2:1 ratio, the threshold was reached between 1 hour and 20 minutes and 6 hours and 20 minutes. With three and a half hours, the mean value is higher than for pure monoolein. However, the deviations between the individual data points of pure monoolein and samples containing urea and TMAO are high and the intervals largely overlap, in which the values for both compositions are. It can be concluded that the effects of urea and TMAO on the equilibration process compensate each other to a large extent when the two molecules are present in a 2:1 ratio.

4.6 Polyethylene glycol

In this section, the results of the pressure-jump study on monoolein in presence of PEG of different sizes are presented. The experiments were conducted at a water content of 80 wt% and at pH 5. Figure 4.9 and 4.10 show how PEG in concentrations of 150 g/L changed the monoolein structure at 50 bar before the pressure-jump. PEG with a molecular weight of 4000 g/mol and more induced a phase transition into the Ia3d phase, which is usually not observed in excess water [77]. In order to obtain a direct comparison of the dimensions of the cubic channel systems and the polymers, figure 4.9 shows the water channel radius r_w as a function of the radius of gyration R_G (as given by equation 2.9) of the added PEG. In figure 4.10, the lattice constant is shown. The radii of the water channels were determined based on the assumption that the chain length of monoolein does not change when PEG is added. With the excess water boundary of the Pn3m phase of 44.5 wt% at 25 °C and ambient pressure (see chapter 2.2), the water volume fraction in the lipid structures and the chain length of monoolein can be calculated from the lattice constant with the equations given in chapter 2.1. At 50 bar, the lattice parameter of monoolein was 102.8 Å on average, which corresponds to a chain length of 16.1 Å. This value was used for the determination of all water channel radii at 50 bar in this chapter.

For pure monoolein, a channel radius of 24.0 Å was calculated. The data points of pure monoolein and monoolein in presence of PEG 200 overlapped and with 23.8 Å, the mean value was only slightly lower when PEG 200 was added. An increase of the molecular weight of the examined PEG led to a strong decrease of the water channel radius until a constant level of approximately 17 Å was reached for PEG of a molecular weight of 4000 g/mol and more. The lowest Pn3m lattice constant was observed for PEG 2000 with a mean value of 88.8 Å. For larger PEGs, the Ia3d phase was observed instead, with a lattice constant of approximately 130 Å. It is known that the osmotic pressure exerted by PEG reduces with the molecular weight at constant mass concentration [266]. Therefore, the reduction of the lattice constant and water channel radius with increasing molecular weight of the added PEG indicates that the amount of PEG molecules that penetrate into the water channel system of the monoolein structures strongly decreases with the size of the polymers. Since the radii of gyration of the investigated PEGs and the water channel radii of monoolein structures are in a similar order of magnitude, this is not surprising. While the radius of gyration of PEG 200 is six times smaller than the observed water channel radius, both radii are almost the same in presence of

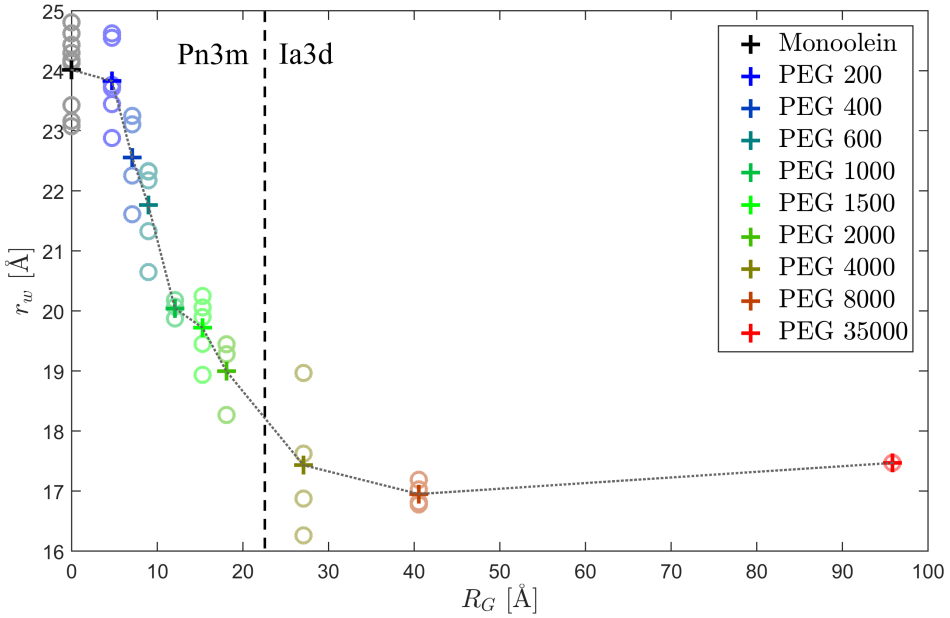

Figure 4.9: Radius of the water channels r_w of cubic monoolein phases at 50 bar in presence of PEG with different radii of gyration R_G. The *circles* represent the values for different samples to illustrate the variance. The *crosses* mark the mean values.

PEG 2000. For PEG 4000, where the Ia3d phase occurred, the radius of gyration is larger than the water channel radius of pure monoolein. At this point, the polymers might still be able to penetrate into the water network of the lipid structures, since their shape is not necessarily globular. However, the confinement of the polymers in the water channels is highly unfavorable for the molecules, as it reduces their configuration entropy. Above 4000 g/mol, the water channel radius barely changed with the molecular mass of the added PEG. As the osmotic pressure as a function of the molecular weight is also almost constant for large PEGs, this is in good agreement with the assumption that the polymers are fully excluded from the monoolein structures in the whole Ia3d regime. The overlap concentration boundary is crossed between PEG 1500 and PEG 2000 at the applied concentration. Thus, the polymers form an entangled mesh in the Ia3d regime.

Figure 4.11 shows the spacing of the L_c phase in presence of PEG at 1500 bar. As especially PEGs with high molecular weight induce a shift of the cubic-to-lamellar transition, some of the pressure-jumps were not conducted from a starting value of 1000 bar but from 1500 bar or even 2000 bar. Therefore, the initial state of the monoolein structures was not always the same. At a starting pressure of 1000 bar, the lamellar spacing was typically approximately 1 Å lower than at 1500 bar. At 2000 bar, the L_m phase with a spacing of about 43 Å was still present. However, systematic deviations of the dynamic behavior after the pressure-jump due to the different starting pressures were

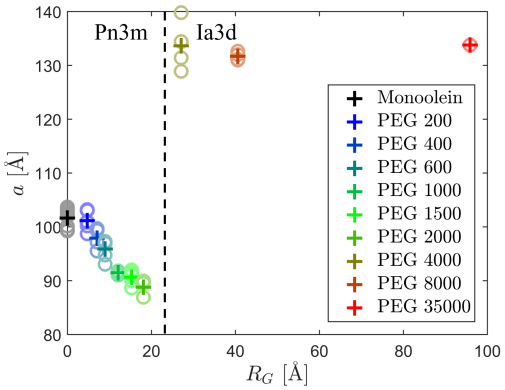

Figure 4.10: Equilibrium lattice constants of cubic monoolein phases at 50 bar in presence of PEG with different radii of gyration R_G. The *circles* represent the values for different samples to illustrate the variance. The *crosses* mark the mean values.

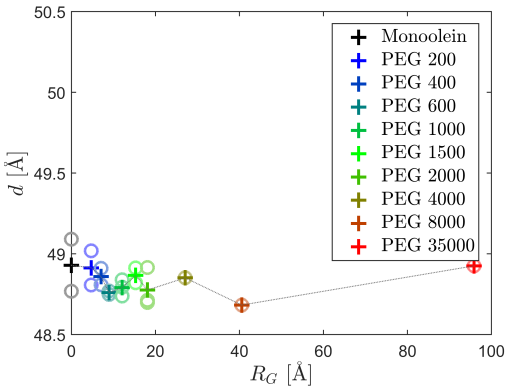

Figure 4.11: Spacing of the L_c phase of monoolein at 1500 bar in presence of PEG with different radii of gyration R_G. The *circles* represent the values for different samples to illustrate the variance. The *crosses* mark the mean values.

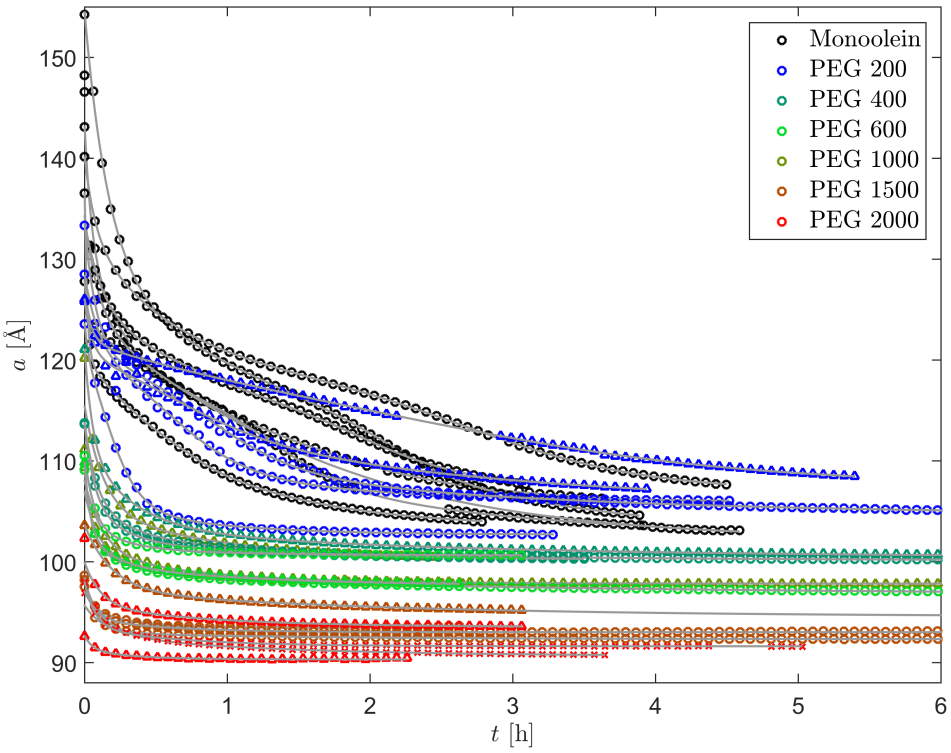

Figure 4.12: Decrease of the Pn3m lattice constant of monoolein after a pressure-induced lamellar-to-cubic transition in presence of PEG of different molecular weight (*colored symbols*) and fits (*gray lines*). *Circles* indicate that the pressure-jump was conducted from a starting pressure of 1000 bar, *triangles* indicate a starting pressure of 1500 bar and *crosses* of 2000 bar.

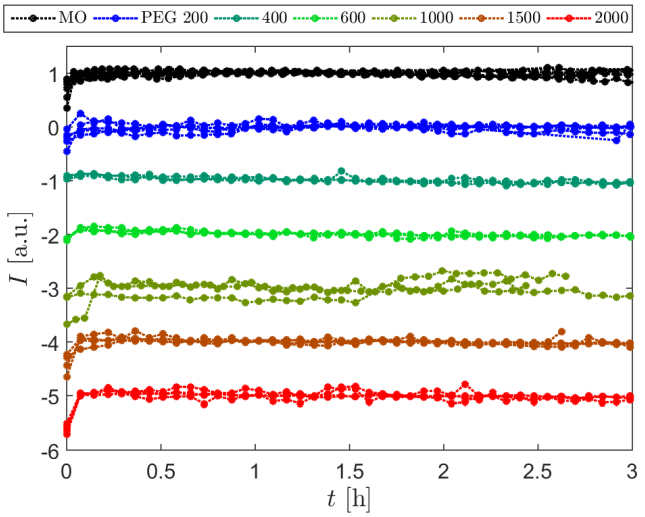

Figure 4.13: Time-dependence of the integrated intensity of the first two Pn3m Bragg reflections of monoolein (MO) in presence of different PEGs after a pressure-jump. The integrated intensities were normalized to their temporal mean values and vertically shifted for clarity.

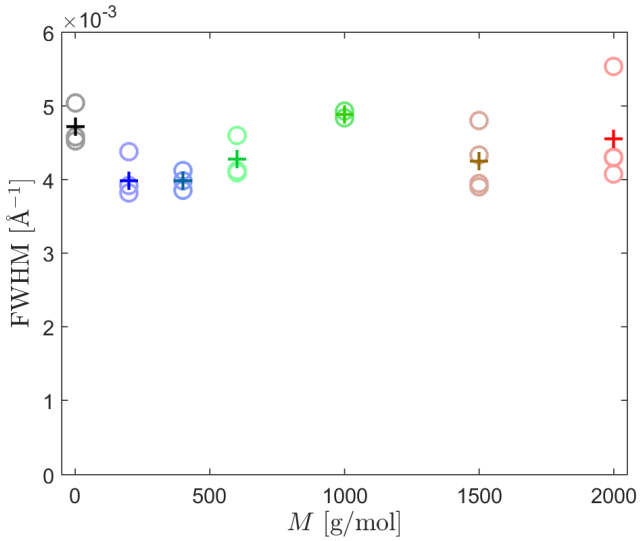

Figure 4.14: Mean FWHM of the first Pn3m reflections of monoolein in presence of PEG of different molecular weight after a pressure-jump. For the calculation of the mean values, only scans which were taken in plateau regions, where the lattice constant barely changed in time, were considered. The *circles* represent the values for different samples to illustrate the variance. The *crosses* mark the mean values.

not found. Figure 4.11 shows that PEG barely affected the spacing of the L_c phase. As discussed for TMAO in chapter 4.5, this is most likely due to the fact that the L_c phase is highly dehydrated even in absence of additives. Therefore, a further compression due to depletion is not observed.

Figure 4.12 shows the decrease of the Pn3m lattice constant of monoolein in presence of PEG with a maximum molecular weight of 2000 g/mol. While the equilibration processes of pure monoolein and monoolein interacting with PEG 200 took several hours, the decrease of the lattice constant was almost completed after one hour for larger PEGs.

To analyze the formation process and shape of the monoolein structures in presence of PEG, figure 4.13 and 4.14 show the integrated intensity and the width of the Pn3m reflections. It can be seen that in all cases, the intensity reached its maximum level very fast. Typically, already the second data point taken after four minutes had the

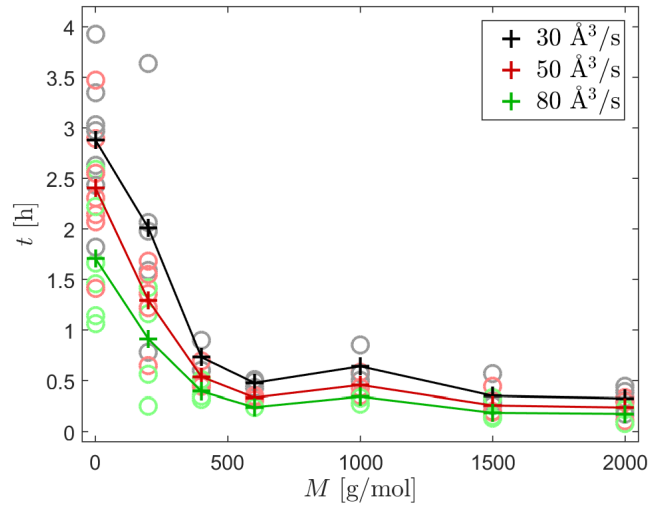

Figure 4.15: Time t until the released water volume per second and Pn3m unit cell decreased below threshold values of 30 Å^3/s, 50 Å^3/s and 80 Å^3/s after a pressure-jump in presence of different PEG to compare the speed of the equilibration dynamics. The *circles* represent the values for different samples to illustrate the variance. The *crosses* mark the mean values.

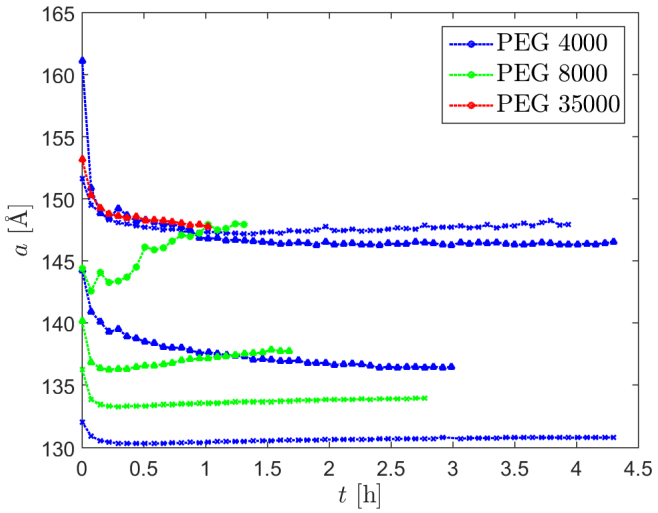

Figure 4.16: Decrease of the Ia3d lattice constant of monoolein after a pressure-induced lamellar-to-cubic transition in presence of PEG of different molecular weights (*colored symbols*). *Circles* indicate that the pressure-jump was conducted from a starting pressure of 1000 bar, *triangles* indicate a starting pressure of 1500 bar and *crosses* of 2000 bar.

maximum intensity. The width of the reflections was barely affected by the addition of PEG. The data presented in figure 4.14 are the mean values of the FWHM of the first Pn3m reflection in a time span where the lattice parameter was almost constant. Typically, the last nine scans of the samples were considered. The intensity and width of the observed reflections reveal that the maximum size of the lipid structure was similar in presence of all examined PEGs and that the maximum size of the crystallites was reached very fast in all cases.

In order to compare the speed of the equilibration process of monoolein in presence of different PEGs, the data in figure 4.12 were fitted with a superposition of two exponential function and a hyperbolic tangent, yielding an analytic description of the lattice constant as a function of time. With the length of the lipid molecules, the water content of the unit cell was determined. The first temporal derivation of the resulting term describes

the water volume that is released per time and unit cell during the equilibration. Figure 4.15 shows how much time elapsed until this parameter dropped permanently under certain thresholds for the different samples as a measure for the equilibration time. To assess the accuracy of this criterion, three different limits of 30 Å^3/s, 50 Å^3/s and 80 Å^3/s were set. In all three cases, the equilibration time reduced strongly with the addition of PEG with increasing molecular weight up to 600 g/mol. For PEG larger than 600 g/mol, the elapsed time remained largely independent of M. Comparable to the effect of TMAO and sucrose, the osmotic pressure exerted by PEG increased the speed of the equilibration process strongly.

Figure 4.16 shows the behavior of the Ia3d lattice constant of monoolein after a pressure-jump in presence of PEG with high molecular weight. On average, the lattice constants at 50 bar before the pressure-jump were 133.6 Å, 131.8 Å and 133.8 Å for PEG 4000, 8000 and 35000, respectively. The structures that formed after the pressure-jump exhibited mostly much larger lattice constants than before. In most cases, a fast decrease of the lattice constant was observed initially. For two of the PEG 4000 and all PEG 8000 samples, the lattice parameter increased again after that. While the lamellar phase is very low hydrated, the water content of the cubic phase is relatively high. Therefore, an increase of the lattice constant after the pressure-jump could be explained by a slow release of excess water from the entangled mesh of polymers that surrounds the lipid structures. As the behavior of the different samples strongly deviates, it is assumed that the amount of available excess water is locally very different.

4.7 Viral fusion peptides

In this section, the results of the pressure-jump study on monoolein in presence of fusogenic peptides are presented. The experiments were conducted at a water content of 80 wt% and at the fusogenic pH of 5. Figure 4.17 shows that all peptide sequences increased the Pn3m lattice constant at 50 bar before pressurization. It is believed that FLs of TBEV and VSV interact mainly with membrane surfaces and that they only insert via aromatic anchors with a limited penetration depth into lipid structures [125, 205]. Thus, the observation that these peptides increase the lattice constant of monoolein can be explained by an enlargement of the headgroup area resulting from favorable interactions between headgroups and peptides, comparable with the effect of urea. Moreover, an insertion with limited depth partially compensates the wedge shape of the lipids, leading to a reduced negative curvature [291].

The other three peptides have pronounced hydrophobic properties and are presumably able to penetrate deeply into the tailgroup regions of the lipid structures. Thus, their structural properties when they are incorporated into a membrane are crucial for their effect on lipid phases. Tenchov et al. found that HA2-FP reduces the lattice parameter of cubic phospholipid structures [198]. They suppose that the rigid V-shape [196] of HA2-FP induces positive curvature along its contour and negative curvature perpendicular to it as the lipids wrap around the peptide, resulting in an increasing negative Gaussian curvature. The effect of such an interaction mechanism could strongly depend

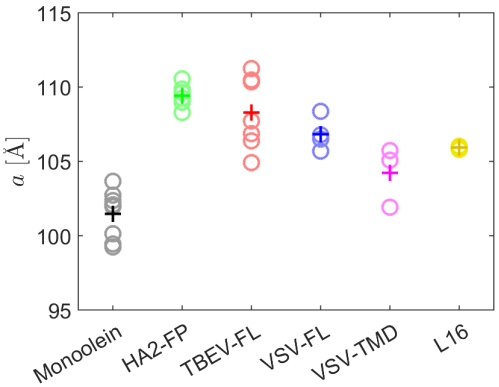

Figure 4.17: Equilibrium values of the Pn3m lattice constant of monoolein at 50 bar in presence of different fusogenic peptides. The *circles* represent the values for different samples to illustrate the variance. The *crosses* mark the mean values.

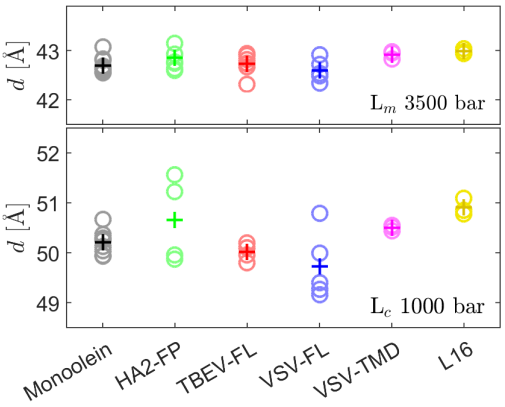

Figure 4.18: Spacing of monoolein in the L_m phase at 3500 bar and the L_c phase at 1000 bar in presence of different fusogenic peptides. The *circles* represent the values for different samples to illustrate the variance. The *crosses* mark the mean values.

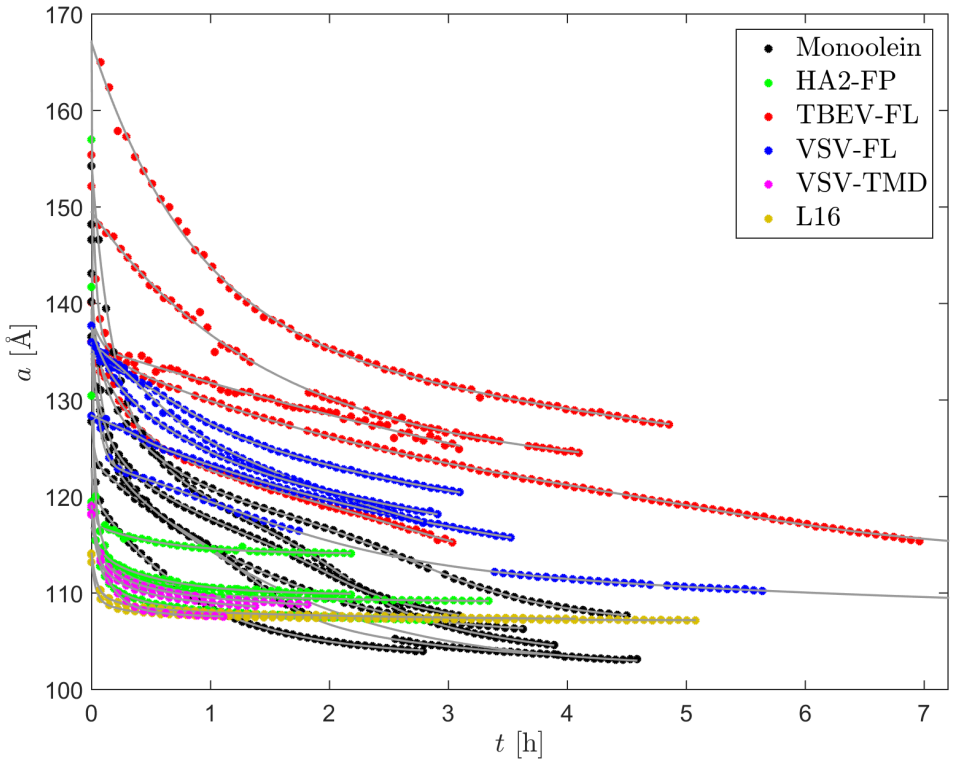

Figure 4.19: Decrease of the Pn3m lattice constant of monoolein after a pressure-induced lamellar-to-cubic transition in presence of fusogenic peptides (*colored dots*) and fits (*gray lines*).

on the membrane composition. Possibly, HA2-FP can also be favorably incorporated in monoolein membranes with negative Gaussian curvature, but the corresponding optimum lattice constant might still be higher than the lattice constant of pure monoolein. For VSV-TMD, it is assumed that it inserts as an α-helix perpendicular to the membrane surface. A cylindrical insertion with a similar cross-section in head- and tailgroup region reduces membrane curvature. The L16 peptide was also found to form α-helices in membrane mimicking environments [128]. Since leucine is highly hydrophobic while the anchor unit is polar, it is likely that L16 also inserts parallel to the membrane normal rather than parallel to the surface, so that a similar geometric argument can be made as for VSV-TMD.

Figure 4.18 shows that the effect of the peptides on the spacing of the L_m phase at 3500 bar and the L_c phase at 1000 bar before the pressure-jump was low. The data suggest that the peptides are widely displaced from the lipid structures in the lamellar crystalline phases. A disruption of the crystalline chain order by incorporated peptides would presumably cause a pronounced reduction of spacing. An accumulation in the narrow hydration layer also seems unlikely.

The time-dependence of the lattice constant after a pressure-jump beyond the lamellar-to-cubic boundary presented in figure 4.19 reveals that the fusogenic peptides strongly affected the dynamics of the monoolein structures. While HA2-FP, VSV-TMD and L16 drastically accelerated the equilibration process, the FLs of TBEV and VSV slowed it down. In presence of TBEV-FL and in three of four cases also in presence of VSV-FL, the Im3m phase formed in coexistence with the Pn3m phase. In all samples, the Im3m and Pn3m structures had the same mean Gaussian curvature, so that their lattice constants decreased in parallel, fulfilling the condition $a_{\mathrm{Im3m}} = (1.28 \pm 0.02) \cdot a_{\mathrm{Pn3m}}$ (see equation 2.8) at every point within the specified error. For urea, TMAO, sucrose, and PEG, an increase of the equilibrium lattice constant was connected to a slower and a decrease of the equilibrium lattice constant was connected to a faster equilibration process after the pressure-jump. In contrast, the examined peptides showed different effects on the dynamics, although they all increased the equilibrium lattice constant. Therefore, the acceleration of the reduction of the lattice constant induced by HA2-FP, VSV-TMD and L16 cannot be explained by depletion forces. Instead, this observation confirms that these peptides modulate the behavior of the monoolein structures by inserting into their hydrophobic region.

Before possible interaction mechanism of the fusogenic peptides with the monoolein structures are discussed in more detail, the formation process and size of the cubic crystallites will be analyzed based on the intensity and width of the observed reflections. Figure 4.20 shows how the integrated intensity of the first two Bragg reflections of the Pn3m phase changed with time for monoolein with and without HA2-FP, VSV-TMD, and L16. The formation of the Pn3m structures was completed in a few minutes for all samples, as the maximum value of the intensity was typically reached already after the first scan. The integrated intensities of the first Im3m and the first Pn3m reflection are compared for TBEV-FL and VSV-FL in figure 4.22. The Im3m phase was more pronounced in presence of TBEV-FL than in presence of VSV-FL. In both cases, the Pn3m phase built up fast, as the corresponding reflections typically reached their

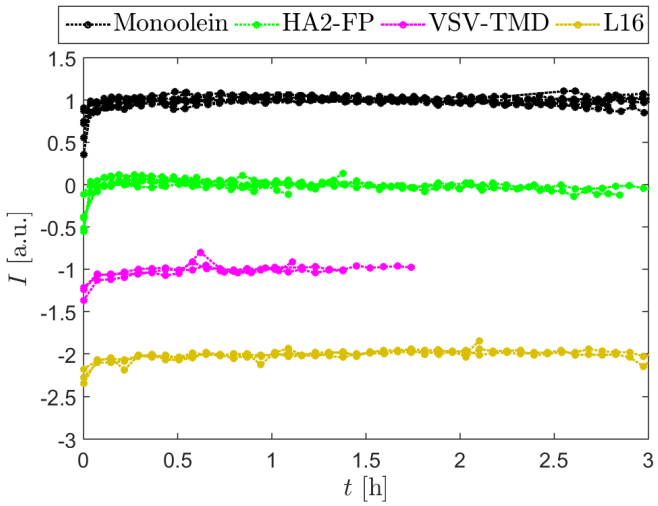

Figure 4.20: Time-dependence of the integrated intensity of the first two Pn3m Bragg reflections of monoolein in presence of different fusogenic peptides after a pressure-jump. The integrated intensities were normalized to their temporal mean values and vertically shifted for clarity.

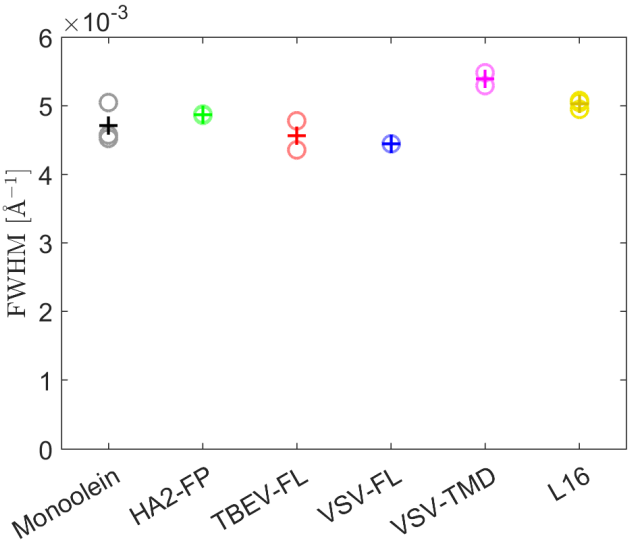

Figure 4.21: Mean FWHM of the first Pn3m reflections of monoolein in presence of fusogenic peptides after a pressure-jump. For the calculation of the mean values, only scans which were taken in regions, where the change of the lattice constant was slow, were considered. The *circles* represent the values for different samples to illustrate the variance. The *crosses* mark the mean values.

maximum enlargement during the first ten minutes. After that, it was observed that the Pn3m intensity reduced while the Im3m intensity increased, indicating that Pn3m structures converted into Im3m structures. For TBEV-FL, in some cases, the reverse process occurred after a few hours. In conclusion, the formation process of the cubic structures was much faster than the equilibration dynamics of the lattice constants in presence of all five peptides. However, in case of the FLs, the amount of Pn3m and Im3m changed slightly also after a few hours.

In figure 4.21, the mean values of the FWHM of the first Pn3m reflection in regions where the slope of the decrease of the lattice constant was low are compared. Typically, the last nine values of a measurement series were taken into account. Only data from experiments conducted at BL2 and not at BL9 are shown, since the experimental resolution at BL2 and BL9 is very different and thus the FWHM values are difficult to

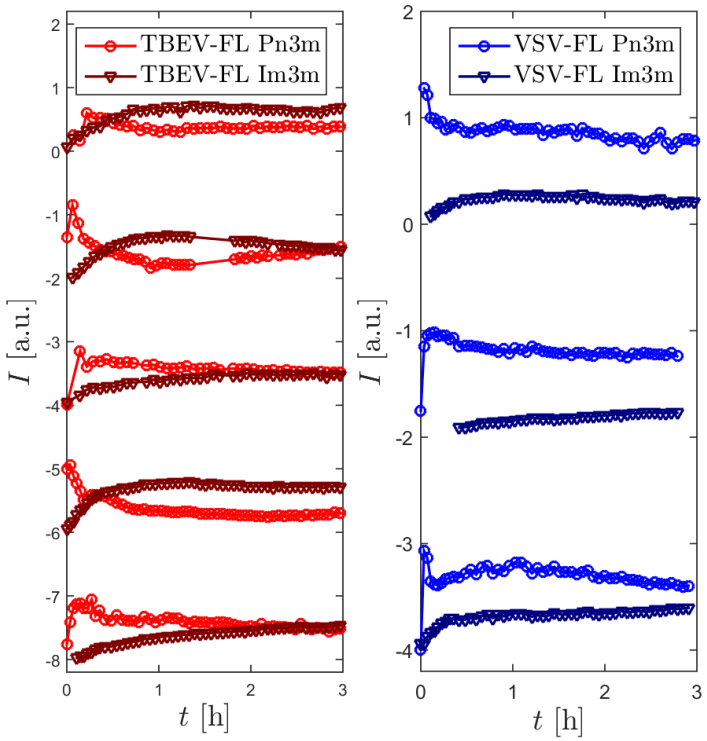

Figure 4.22: Time-dependence of the integrated intensity of the first Pn3m and the first Im3m Bragg reflection of monoolein in presence of TBEV-FL and VSV-FL after a pressure-jump. The integrated intensities were normalized to the temporal mean values of the sum of the Pn3m and Im3m intensity and vertically shifted for clarity.

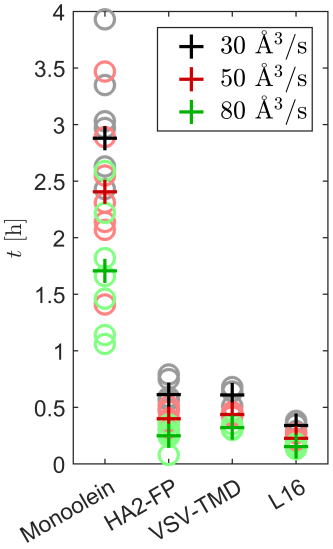

Figure 4.23: Period of time t until the released water volume per second and Pn3m unit cell decreased below threshold values of 30 Å^3/s, 50 Å^3/s and 80 Å^3/s after a pressure-jump in presence of different fusogenic peptides to compare the speed of the equilibration dynamics. The *circles* represent the values for different samples to illustrate the variance. The *crosses* mark the mean values.

compare. It can be seen that the fusogenic peptides had only minor effects on the reflection width. Therefore, it can be assumed that the mean size of the Pn3m crystallites was similar in all samples.

In figure 4.23, the speed of the convergence of the lattice constant towards equilibrium of monoolein in presence and absence of HA2-FP, VSV-TMD and L16 is compared based on the time that passed until the released water volume per unit cell and time dropped under certain limits, like it was also done for PEG in chapter 4.6. According to these limits, the equilibration of the Pn3m phase after a pressure-jump was approximately 6 times faster when HA2-FP was added. While the acceleration caused by VSV-TMD was comparable to the effect of HA2-FP, the process was twice as fast in presence of L16.

Since all three peptides caused a strong acceleration of the equilibration process, it is unlikely that unique structural details of the individual peptides are the primary reason for this behavior. A common feature of all three sequences is their hydrophobicity, so

that they are presumably able to penetrate into the hydrophobic regions of membranes. As shown above, the L_c phase was barely affected by the peptides and it was assumed that the peptides are displaced from the lipid structures into the excess water in this phase. During the transition into the cubic phase, the crystalline hydrocarbon chains melt and the lipid structure becomes more permeable. Possibly, an increase of the area of the Pn3m surface due to a reinsertion of peptides is the main driving force of the fast decrease of the lattice constant.

When peptides leave the hydration water volume and insert into the lipid film, the hydration volume per unit cell reduces slightly, while the film area increases. From previous studies it is known that HA2-FP can expand the area of a lipid film strongly with approximately 200 $Å^2$ per inserted molecule [292, 293]. A changed ratio between hydration volume and lipid film area forces the dimensions of the unit cell to adapt. Based on the assumption that the chain length of monoolein $l = 16.1$ Å remains constant, it can be determined how an enlargement of the Pn3m surface area affects the lattice parameter at constant water content. For example, upon an increase of the Pn3m surface area at a lattice constant of $a = 130$ Å by a factor of 1.4, the lattice constant would have to assume a value of $a = 110$ Å to maintain the same water capacity. Therefore, an enlargement of the Pn3m surface area by the insertion of peptides could reduce the lattice constant without water being released from the cubic phase.

Besides a surface enlargement, the dynamics of the lattice constant are presumably affected by further features of the peptides and their interactions with the surrounding lipids. The exact alignment and shape of the peptides, when they are incorporated in the lipid film, might promote a certain curvature and facilitate the formation of the corresponding lattice constant. It is also possible that a reduction of the surface area is caused by pressure-induced structural changes of peptides that are already incorporated in the lipid structures. However, for HA2-FP, a high structural stability in membranes was found upon pressurization [51].

The fact that the FLs of VSV and TBEV did not accelerate the decrease of the lattice constant is a strong indication that they do not penetrate monoolein films. Instead, they seem to stabilize swollen Pn3m phases. This can again be explained by a preferred interaction with the surface of the lipid layers and an attachment via aromatic anchors. This behavior promotes structures with large headgroup areas and counteracts the formation of negative curvature.

With HA2-FP and TBEV-FL, also pressure-jumps from 50 bar to 1500 bar were conducted. Figure 4.24 shows the behavior of the Pn3m lattice constant. As already discussed in section 4.4, initially, monoolein remained in the cubic Pn3m phase. The lattice constant increased slowly until the system underwent a phase transition into the lamellar L_c phase. For one sample, the phase transition was observed between 11 h and 17 h after the pressure-jump. Unfortunately, this was during a lock-down period of the synchrotron light source, so that the process was not monitored directly. The other two samples did not show a phase transition after 19 h and 76 h measuring time. In all three cases, the lipid structures were initially slightly compressed by the pressure application, before they gradually incorporated more and more water, so that the lattice constant increased. Although the swelling slowed down over time, even after 75 h, a slight increase

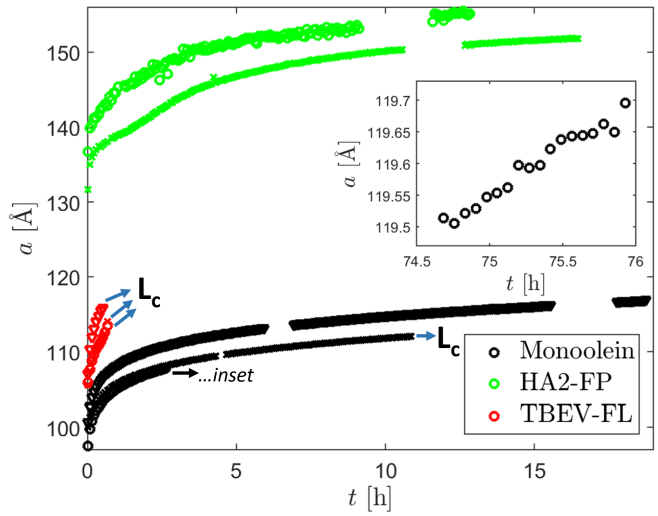

Figure 4.24: Behavior of the Pn3m lattice constant of monoolein after a pressure-jump from 50 to 1500 bar in presence and absence of HA2-FP and TBEV-FL. The *symbols* indicate different samples. For the TBEV-FL samples and one pure monoolein sample, a transition into the L_c phase was observed. The *inset* shows the continuation of the measurements on the monoolein sample represented by the *black circles*.

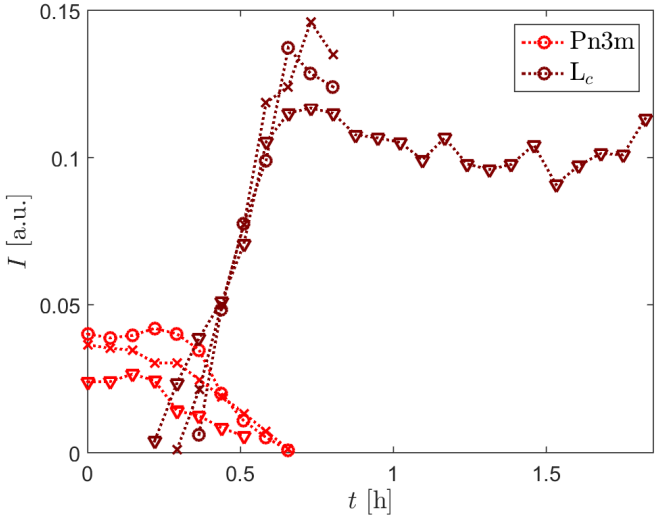

Figure 4.25: Integrated intensity of the first two Pn3m and the first L_c reflection of monoolein in presence of TBEV-FL after a pressure-jump across the cubic-to-lamellar phase boundary as a function of time. The *symbols* indicate different samples.

of the lattice parameter was still visible.

TBEV-FL drastically changed the behavior of monoolein upon pressure-jumps from 50 bar to 1500 bar. The lattice constant increased much faster and the phase transition into the lamellar phase occurred earlier. For all three samples, the Pn3m reflections fully disappeared 40 minutes after the pressure-jump at the latest. Figure 4.25 shows the integrated intensity of the Pn3m and L_c reflections as a function of time. It can be seen that the lamellar phase already formed after approximately 15 minutes. Then, the intensity of the reflections of the cubic phase linearly decreased and the intensity of the reflections of the lamellar phase linearly increased for approximately 20 minutes, until only the lamellar phase remained. The experiment shows that TBEV-FL does not only stabilize lipid structures with a large headgroup area, but also promotes their formation and even the occurrence of phase transitions. The results confirm the assumption that

TBEV-FL interacts mainly with the surface of lipid structures. On average, the L_c phase formed with a spacing of 49.04 Å in presence of TBEV-FL. After the transition in a pure monoolein system, the spacing was 49.09 Å. Considering the variance of the data presented in figure 4.18, it can be concluded that TBEV-FL had no effect on the L_c spacing within the experimental resolution. This indicates that the peptide was displaced from the lipid structure once the phase transition was completed.

When HA2-FP was added to the monoolein system, a fast increase of the lattice constant to approximately 140 Å was observed immediately after the pressure-jump to 1500 bar. After that, a gradual swelling of the cubic structures occurred, which slowed down over time. In contrast to TBEV-FL, the accelerated increase of the lattice constant was not connected to an early transition into the lamellar phase. During the observation periods of 13 and 16.5 h, the cubic phase remained stable. This confirms that the interaction mechanisms of HA2-FP and TBEV-FL with monoolein are fundamentally different. The rapid increase of the lattice constant was presumably connected to a reduction of the area of the Pn3m surface by a displacement of peptides from the lipid layers. However, it is likely that the peptides at least partially remained incorporated in the lipid structure and exerted a stabilization effect, which prevented the cubic-to-lamellar phase transition even at lattice constants of more than 150 Å. Possibly, the Gaussian curvature in this lattice constant range is ideally matched to the incorporation of a HA2-FP.

The observed effects of different peptide sequences on the structure and dynamics of monoolein in excess water show that fusogenic peptides have different interaction mechanisms with membranes. A general distinction can be made between very hydrophobic peptides that penetrate deeply into membranes and peptides that interact mainly with the surface of lipid structures. Therefore, the effect of HA2-FP on monoolein structures was more similar to the behavior of the TMD of VSV and the artificial L16 peptide than the attacking sequences of TBEV and VSV.

4.8 Conclusion

In this chapter, the equilibration process after a pressure-jump across the lamellar-to-cubic phase boundary of monoolein in excess water was analyzed. After a pressure-jump, the cubic phase formed in a swollen state and slowly released excess hydration water until the equilibrium lattice constant was reached after several hours. It was found that the formation process of the cubic crystallites was much faster than the equilibration of the lattice constant, since the full intensity of the reflections, which correspond to the cubic phase, was typically reached after a few minutes. This did not change when the system contained additives. Moreover, also the width of the reflections and thus the mean crystallite size was barely affected.

In agreement with existing knowledge, TMAO and sucrose reduced the equilibrium lattice constant of monoolein in the Pn3m phase, while urea increased it [26, 71, 242]. In this study, it was shown that this behavior translates into an acceleration of the equilibration process in presence of TMAO and sucrose, and a deceleration in presence

of urea. The observations can be explained by the *osmophobic effect*, which causes a displacement of TMAO and sucrose from the water channel system of the cubic phase and thus an osmotic pressure that compresses the lipid structures, and the affinity of urea to interact with lipid surfaces resulting in a stabilization of states with high headgroup areas. Similar to the compensation of the effects of urea and TMAO on the structure of proteins that was found in previous studies [223–225], samples containing a mixture of both osmolytes behaved very similarly to pure monoolein samples.

Similar to TMAO and sucrose, PEG decreased the equilibrium lattice constant of the Pn3m phase and increased the speed of the equilibration process after a pressure-jump. The lattice constant of the Pn3m phase reduced with increasing molecular weight of the polymers. As the osmotic pressure exerted by PEG decreases as a function of the molecular weight [266], this effect is attributed to a reduced ability of larger PEGs to enter the cubic water channel system. Therefore, large polymers exert a more pronounced depletion force on the cubic phase. Once the radius of gyration was higher than the radius of the water channels, monoolein formed the Ia3d phase, which is usually not observed at excess water conditions [77]. Beyond this point, the cubic structure was not further compressed with increasing molecular weight of the polymers. The speed of the reduction of the lattice constant after a pressure-jump increased with the molecular weight up to 600 g/mol and remained almost constant for larger PEGs in the Pn3m regime. In the Ia3d regime, the equilibration process was found to be non-monotonic, as the cubic structures compete with the surrounding entangled mesh of polymers to absorb the available water.

All five examined peptide sequences increased the equilibrium lattice constant of monoolein. However, their effects on the equilibration dynamics after a pressure-jump were very different. While HA2-FP, VSV-TMD and L16 caused a drastic acceleration of the decrease of the lattice constant, TBEV-FL and VSV-FL decreased the speed of the process. These observations prove that the fusogenic peptide sequences interact very differently with lipid structures. Presumably, the hydrophobic peptides HA2-FP, VSV-TMD and L16 induce the fast reduction of the lattice constant by penetration of the lipid structures and an enlargement of the Pn3m surface. In addition, there are probably more specific interactions based on the individual structure of the peptides that have direct effects on the film curvature. Similar to urea, the FLs stabilized structures with large headgroup areas which can be explained by preferred interactions with the surface of lipid layers. Moreover, an insertion of aromatic anchors with limited penetration depth might counteract the spontaneous curvature of monoolein. Pressure-jumps in the opposite direction confirmed this interpretation and showed that the interaction of TBEV-FL induces a faster transition from the cubic to the lamellar phase. HA2-FP induced a fast increase of the lattice constant, but stabilized the cubic structures at the same time, since no phase transition into a lamellar state was observed even after 16 h. At this point, a lattice constant of more than 150 Å was reached. The observations suggest that HA2-FP does not generally increase the negative curvature of lipid phases, but induces a specific curvature depending on external conditions and the membrane composition. However, to confirm that the stabilization of the swollen Pn3m phase is indeed due to the structural properties of HA2-FP, the influence of VSV-TMD and

L16 on the behavior of monoolein after pressure-jumps over the cubic-to-lamellar phase boundary will be examined in a future study.

In this chapter, the effects of fusogenic peptides on the dynamic behavior and curvature of lipid structures was discussed. The results indicated different penetration depths of the sequences in lipid membranes. The study presented in the next chapter addresses the adsorption and insertion behavior of the peptides directly as the vertical and lateral structure of lipid Langmuir films in presence of fusogenic peptides is explored. This model system does not provide the opportunity to study effects on the membrane curvature, but enables a direct structural resolution of the peptides interacting with lipid structures and thus complements the results of this chapter. In good agreement with the assumptions on the interaction of the sequences with monoolein made in this chapter, it was found that HA-FP and VSV-TMD are able to insert deeply into the hydrophobic regions of phospholipid monolayers, while TBEV-FL and VSV-FL tend to attach to the surface.

Chapter 5

The interaction of viral fusion peptides with Langmuir layers

5.1 Objective

In this study, the interaction of fusogenic peptides of viral envelope proteins with phospholipid monolayers at the air-water interface was examined with XRR and GID. The monolayer technique is a well-established tool for the investigation of peptide- or protein-membrane interactions [294–296]. Although only half of an endosomal membrane is represented in this model, this approach is appropriate for the study of FPs and FLs, as they interact primarily with the outer leaflet of a bilayer [125, 196, 205]. Combining XRR and GID yields a comprehensive insight into the structure of Langmuir monolayers. From the investigation of the vertical layer structure with XRR, conclusions can be drawn if fusogenic peptides adsorb at the membrane surface or penetrate it in an early stage of the fusion process. In contrast, GID provides information on changes of the lateral organization of a membrane induced by fusogenic peptides.

5.2 Sample preparation

Langmuir films of 1,2-dipalmitoyl-*sn*-glycero-3-phosphocholine (DPPC, Sigma Aldrich) and 1,2-dipalmitoyl-*sn*-glycero-3-phosphate (DPPA, Sigma Aldrich) were spread from chloroform solutions containing lipids in a concentration of 1 mg/mL. In case of DPPA, 1 mL methanol was added per 10 mL solution to improve the solubility. A few drops of the lipid solution were gradually spread on the surface of aqueous solution in a Langmuir trough until a surface pressure of 1-3 mN/m was reached. After an evaporation time of several minutes, the target pressure was adjusted by compressing the monolayer slowly with a movable barrier. Film pressures of 5, 15, 25, and 35 mN/m were applied. Sørensen's phosphate buffer solution at pH 5 consisting of 0.113 g/L potassium dihydrogen phosphate and 8.992 g/L disodium hydrogen phosphate dihydrate solved in ultra pure water (specific electrical resistivity $> 18\,\mathrm{M\Omega cm}$) was used as subphase. The fusogenic peptides (GeneCust, $> 90\,\%$ purity) were dissolved in 1 mL buffer and then

injected underneath the monolayer, resulting in a final peptide concentration of 2 µM. The sample temperature was 20 °C for all measurements.

5.3 Experimental setup

Combined GID and XRR experiments were conducted using synchrotron radiation at beamline ID10 [158] of ESRF with a photon energy of 22 keV ($\lambda = 0.564$ Å) and a beam size of 150 µm (horizontal) × 11 µm (vertical). The setup at ID10 can be seen in figure 5.1. The GID signal was captured with a vertically aligned Mythen 2K 1D detector [297] scanning the horizontal scattering angle 2θ, yielding 2D diffraction patterns. A GID scan took three and a half minutes. For XRR, the specularly reflected and diffusely scattered intensity was monitored simultaneously with a horizontally aligned Mythen 1K 1D detector. To avoid overexposure of the detector, the incoming intensity was adjusted with an attenuator wheel. With increasing angle, the attenuation was incrementally reduced during XRR scans. Including motor movements and attenuator adjustments, the recording of an XRR curve took five minutes. The angular resolution was defined by slits between the sample and the detector in both setups. Further XRR measurements were performed with a Bruker D8 diffractometer using copper K_α radiation with a photon energy of 8.05 keV ($\lambda = 1.541$ Å) and a beam size of 10 mm (horizontal) × 0.1 mm (vertical). The reflectivity curves were captured with a sodium iodide scintillation detector. The corresponding data were not corrected by subtracting an experimentally determined background. Instead, a constant background was set by an additional parameter in the course of the fitting procedure.

Langmuir troughs with a Wilhelmy paper plate microbalance and a movable barrier for a controlled adjustment of the surface pressure served as sample environment. For each measurement, a DPPC or DPPA film was compressed to a certain target pressure and a reference measurement was carried out. Then, a fusogenic peptide was injected and their interaction with the monolayer was investigated either at constant trough surface area or at constant surface pressure. The latter condition was achieved by an automatic

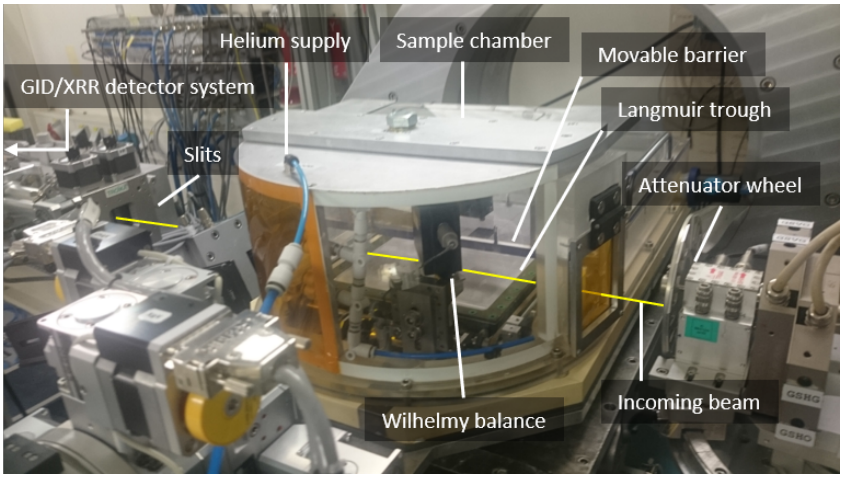

Figure 5.1: The GID and XRR setup at ID10 for the investigation of Langmuir films. The beam path is shown in *yellow*.

readjustment of the barrier. As the GID signal is very weak, the sample cell was flushed with helium during the experiments to suppress air scattering. This procedure also prevents oxidative radiation damage. Moreover, the samples were laterally shifted after every XRR or GID scan to reduce the radiation exposure of the examined sections of the monolayers and the beam was shaded during motor movements.

5.4 Adsorption of fusogenic peptides at the air-water interface

Before the interaction of the fusogenic peptides with Langmuir films will be analyzed, their adsorption behavior at a clean air-water interface is discussed in this section. The peptides were injected in concentrations of 2 µM into a Langmuir trough containing buffer solution and the vertical structure of the air-water interface was determined with XRR. Figure 5.2 shows the obtained reflectivity curves and the corresponding electron density profiles in comparison with an empty water surface. TBEV-FL and VSV-TMD showed no effect, while HA2-FP and VSV-FL accumulated at the interface, forming approximately 25 Å thick adsorbates. The adsorbates are divided into a part with a higher electron density than water and one with a much lower electron density. Presumably, the peptides arranged in monolayers and partially protruded from the water. In case of HA2-FP, the adsorption at the air-water interface was accompanied by an increase of the surface pressure to 27 mN/m. In contrast, the surface pressure only reached 4 mN/m after the injection of VSV-FL. The addition of TBEV-FL and VSV-TMD did not change the surface pressure, in agreement with the results of the XRR measurements.

VSV-TMD contains a high amount of hydrophobic residues. However, due to the anchor unit, it exhibits a net charge of +4. In contrast, HA2-FP, which also has a pronounced hydrophobic character, contains three acidic residues that decrease the net charge to +1. Therefore, the accumulation of VSV-TMD at the surface might be inhibited by electrostatic repulsion. The two FLs include more polar and charged amino acids but also contain highly hydrophobic aromatic residues. With +6, the net charge of TBEV-FL is much higher than the net charge of VSV-FL, which is +3 at pH 5, so that the repulsion between TBEV-FLs is expected to be stronger. Moreover, VSV-FL has a more flexible structure than TBEV-FL [128], which could facilitate an energetically favorable positioning at the surface.

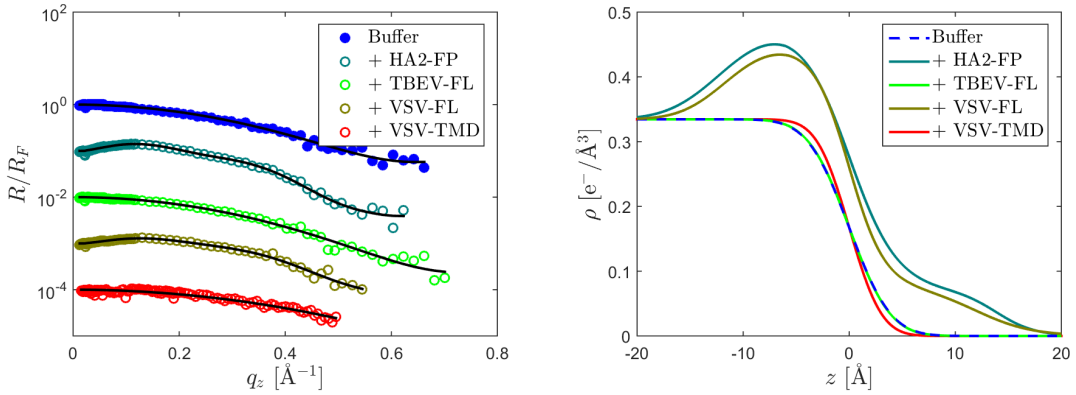

Figure 5.2: XRR data (*left*) of the aqueous solution-air interface in presence and absence of fusogenic peptides (*colored*) with fits (*black*) and the resulting electron density profiles (*right*).

5.5 Isotherms of Langmuir films interacting with fusogenic peptides

In order to evaluate the affinity of the fusogenic peptides to interact with DPPC and DPPA model membranes, their influence on the course of the isotherms of monolayers consisting of the two lipids was examined. For this purpose, the surface pressure was recorded as a function of the area per molecule during compression at a speed of 0.2 cm^2/s in presence and absence of the peptides.

The typical shape of a DPPC isotherm can be seen in figure 5.3 (*black*). In the gaseous state, the lipids are disordered and barely interact with each other. This changes as they are brought closer together during the compression. The regime where the surface pressure starts to increase is called the liquid-expanded (LE) phase. Here, the lipids are still conformationally disordered. At further reduction of the surface area, a plateau region is observed that can be attributed to a phase transition into the liquid-condensed (LC) phase. In this state, the space requirement of the lipids is reduced due to the formation of a crystalline order. In the plateau region, LE and LC phase coexist and the increase in surface pressure is restrained by a growing amount of LC domains. Once the crystallites are big enough to interact with each other, the surface pressure increases strongly until the film collapses. In this regime, the LC phase is predominant, but between the randomly shaped and oriented crystallites gaps occur, in which LE-like domains still remain. Even at 20 mN/m, these domains can constitute half of the surface area [43]. Due to the rather large headgroups, the hydrocarbon chains of DPPC are tilted against the monolayer normal in the LC phase. The tilt angle decreases with growing surface pressure from a maximum value of approximately 40° in the coexistence region. [298–301]

Fusogenic peptides were injected underneath the surface at a pressure of 5 mN/m and the compression was paused for at least 10 minutes until equilibrium was reached.

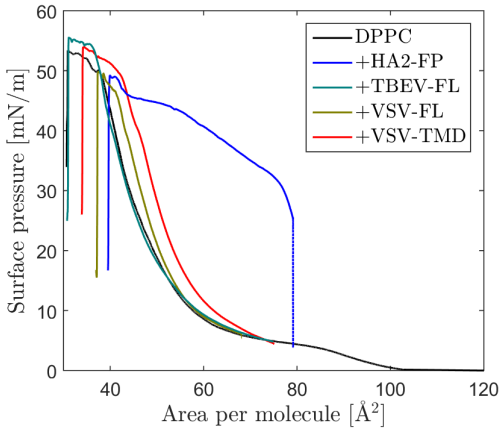

Figure 5.3: Isotherms of DPPC interacting with fusogenic peptides that were injected at a surface pressure of 5 mN/m.

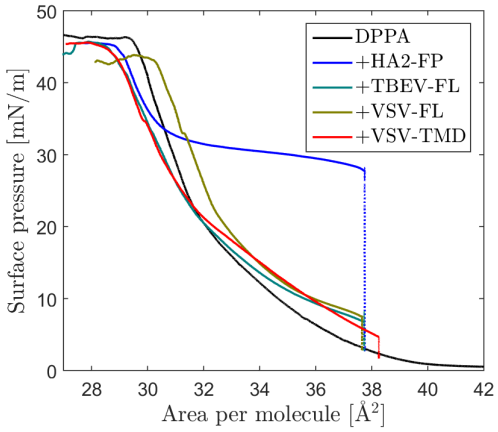

Figure 5.4: Isotherms of DPPA interacting with fusogenic peptides that were injected at a surface pressure of 3 mN/m.

The addition of HA2-FP showed the most pronounced effect (*blue*). In earlier studies, the FPs of HA2 were found to expand the surface area of membranes, indicating an occupied area per molecule of about 200 Å^2 [292, 293], which is in agreement with the V-shaped insertion model [196] described above (chapter 2.5). After the injection of HA2-FPs underneath the DPPC monolayer, their ability to drastically influence the surface area of a membrane was reflected in a strong increase of the surface pressure to almost 30 mN/m. With further compression, the pressure initially rose sharply, but the curve flattened out quickly. Subsequently, a region of linear increase followed and then a further flattening into a plateau region. Before the film finally collapsed, the slope increased again for a short interval. The gradual modulation of the compressibility could have initially been due to configurational changes of the packing of peptides and lipids at the surface and then, possibly, also to a displacement of peptides from the surface. However, the fact that the film collapsed earlier than the bare DPPC layer indicates that HA2-FPs remained incorporated in the monolayer to some extent. In contrast, the addition of TBEV-FL did not change the isotherm within the experimental resolution (*green*). The peptides of VSV showed minor effects (*brown* and *red*). The increase in pressure was slightly steeper and the film collapsed earlier.

Due to the smaller headgroups, the van der Waals interactions between DPPA molecules are stronger compared to DPPC. Therefore, the corresponding isotherm presented in figure 5.4 (*black*) exhibits different features. As a result of the pronounced van der Waals interactions, no LE phase is observed. The compressibility is modulated by phase transitions between different LC phases. In previous studies, it was found that the lipids rearrange between 10 and 30 mN/m from a tilted oblique via a distorted hexagonal to a non-tilted hexagonal phase. However, it should be noted that the occurring tilt angles are much smaller ($< 20°$) than those of DPPC and decrease fast upon compression. [178, 302, 303]

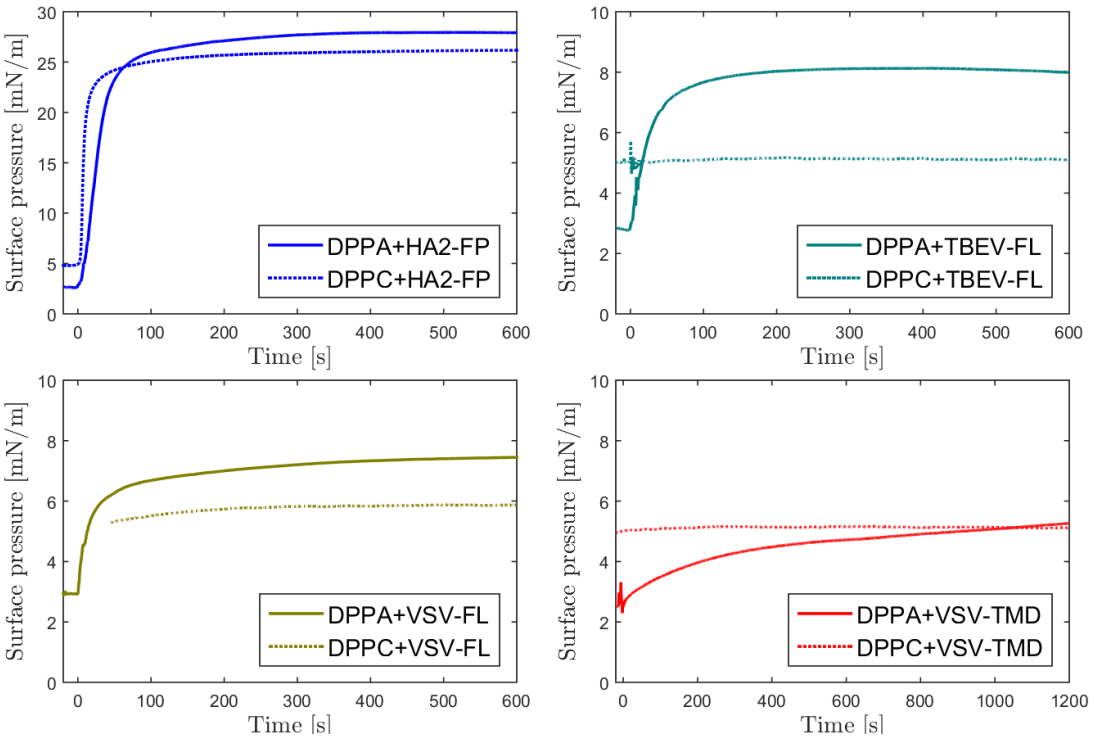

Figure 5.5: Surface pressure after the injection of fusogenic peptides underneath DPPC and DPPA films as a function of time. The peptides were added at $t = 0$.

Since DPPA already arranges in dense packing at low surface pressures, the fusogenic peptides were added at a slightly lower surface pressure of 3 mN/m. Similarly to DPPC, HA2-FP increased the surface pressure immediately to almost 30 mN/m (*blue*). However, at further compression, only two distinct compressibility regimes were found. After the injection, the isotherm entered a broad plateau region. Then, the pressure steeply increased again until the film collapsed. In contrast to DPPC, DPPA lipids are already fully stretched at a surface pressure of 30 mN/m. Therefore, the potential for an improvement of packing by conformational changes is probably lower. GID and XRR experiments presented in the next sections showed that HA2-FPs arrange very differently in DPPC and DPPA monolayers. Although the effects of the other three fusogenic peptides were much smaller (*green*, *brown*, and *red*), they also showed an affinity to interact with DPPA membranes. Their injection increased the surface pressure to different degrees. Due to the positively charged anchor unit, the peptide concentration near negatively charged monolayers increases locally. The increase in surface pressure is an indication that the peptides penetrate the lipid film and not just accumulate underneath it.

Figure 5.5 shows the increase of the surface pressure of DPPC and DPPA films after the injection of the different peptides as a function of time while the compression was paused. HA2-FP showed a very similar effect on the surface pressure of DPPC and

DPPA monolayers. In contrast, it seems that the interaction of the other three peptides with Langmuir monolayers has to be triggered by electrostatic attraction, as their addition increased the surface pressure of DPPA films but not of DPPC films. XRR and GID measurements confirmed this finding as they showed no structural changes of DPPC monolayers within the experimental resolution induced by those three peptides 40 minutes after their injection (see appendix A.2). As the positive net charge of the peptides mainly results from the four consecutive lysines that are part of the artificial anchor unit, the electrostatic attraction cannot be assigned to the actual fusogenic sequences. However, it was shown by Ben-Tal et al. [304] that model peptides consisting of 5 lysine residues adsorb at anionic monolayers but do not penetrate them and do not affect the surface pressure. Therefore, it can be assumed that structural changes of the lipid films, especially in the hydrophobic region, that are visible in GID and XRR measurements are not induced by the anchor unit.

5.6 The interaction of HA2-FP with DPPC Langmuir films

Figure 5.6 shows a typical GID pattern of DPPC in the LC phase. In this phase, the lipids arrange in a distorted hexagonal lattice with $a \neq b = c$ (formula symbols as defined in chapter 3.3, figure 3.5) [301, 305]. The in-plane reflection at $q_z = 0\,\text{Å}^{-1}$ originates from the lattice planes parallel to $\boldsymbol{a}$ as the hydrocarbon chains are tilted towards their neighbor molecules along $\boldsymbol{a}$. The scattering at lattice planes that are parallel to $\boldsymbol{b}$ and $\boldsymbol{c}$ is modulated by the tilt angle resulting in a two-fold degenerate out-of-plane reflection at $q_z > 0\,\text{Å}^{-1}$ [306]. In the LE phase, no crystalline order exists and thus, no reflections are observed with GID.

The intensity distributions of the Bragg rods along $q_{\|}$ and q_z were analyzed to determine lattice parameters and tilt angles. For this purpose, only small regions around the maxima were considered. In this regions, the intensity was integrated along q_z to obtain the scattering distribution as a function of $q_{\|}$ and vice versa. The dimensions of the regions can be seen in figure 5.6. The horizontal intensity distributions of the Bragg rods of DPPC films at different surface pressures in presence and absence of HA2-FP are shown in figure 5.7 and the vertical profiles in figure 5.8. The data were evaluated as described in chapter 3.3. The obtained fit functions are included in the illustrations.

After the addition of HA2-FP, the trough area was kept constant. GID and XRR scans were performed before and 40 minutes after the injection. In agreement with the results of section 5.5, the surface pressure increased to almost 30 mN/m once the FPs were injected underneath DPPC films that were compressed to 5, 15 or 25 mN/m. At an initial compression of 35 mN/m, the FPs did not affect the surface pressure. At 5 mN/m, DPPC is in the LE phase and no reflections occurred in the corresponding GID scans. However, as shown in figures 5.7 and 5.8, reflections appeared after the FPs were injected. At 15 and 25 mN/m, the Bragg reflections shifted to higher $q_{\|}$ values due to the addition of HA2-FP, indicating that the unit cell area reduced. Simultaneously, the tilt angle decreased as the maximum of the out-of-plane reflection moved to lower q_z values (see figure 5.8). At an initial film pressure of 35 mN/m, the GID patterns barely

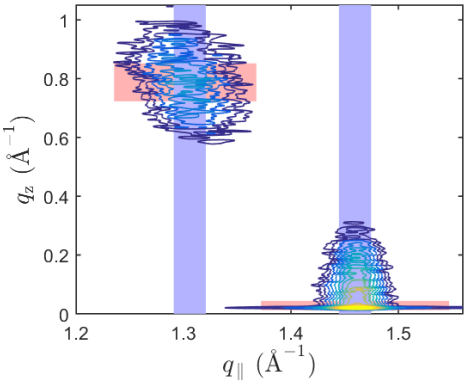

Figure 5.6: Typical GID patten of DPPC in the LC phase. The colored rectangles illustrate the regions of interest that were considered for the analysis of the Bragg rods. The red areas were integrated vertically yielding the intesity as a function of $q_\parallel$ and the blue areas were integrated horizontally yielding the intensity as a function of q_z.

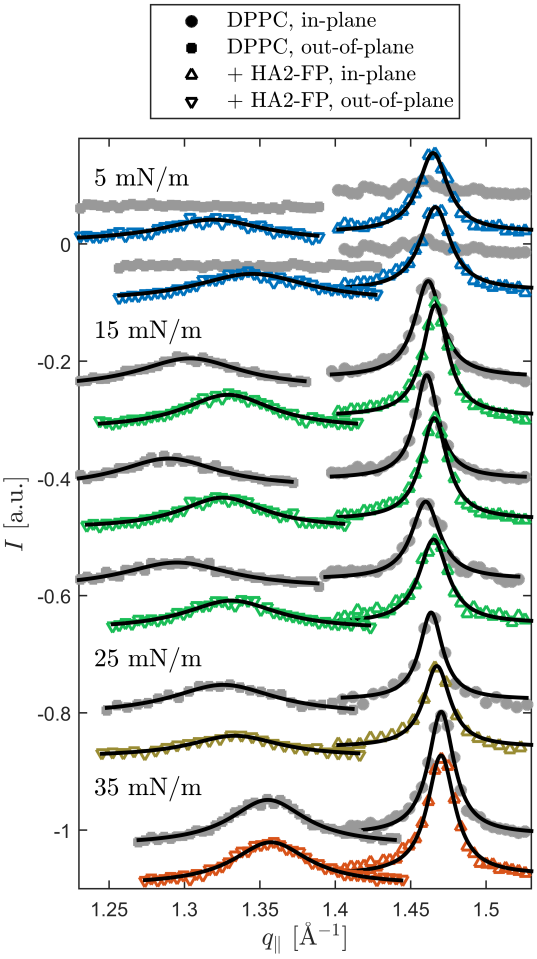

Figure 5.7: GID reflections of DPPC films before (*gray symbols*) and after (*colored symbols*) the injection of HA2-FP as a function of $q_\parallel$ and fits (*black lines*).

changed after the injection of HA2-FP.

Figure 5.9 shows the area of the unit cell A, the tilt angle τ and the mean crystallite size L_1 perpendicular to $\boldsymbol{a}$ as a function of the surface pressure. The mean crystallite size L_2 perpendicular to $\boldsymbol{b}$ and $\boldsymbol{c}$ cannot be reliably determined, since a broadening of the reflection due to a slight asymmetry of the two directions of the 2D crystal cannot be distinguished from actual size effects. After the peptides were added, A and τ adopted the values that would be expected in case of a compression by a reduction of the trough surface. Only L_1 tended to be slightly smaller in presence of the peptides. These observations suggest that HA2-FPs mainly penetrate the LE regions between the LC domains and affect the LC crystallites only indirectly, as the insertion of HA2-FPs into the loosely packed regions leads to an increase of the surface pressure. Evidence of preferential interaction with LE domains was also found for the class I fusion peptide of the human immunodeficiency virus HIV-1 [43].

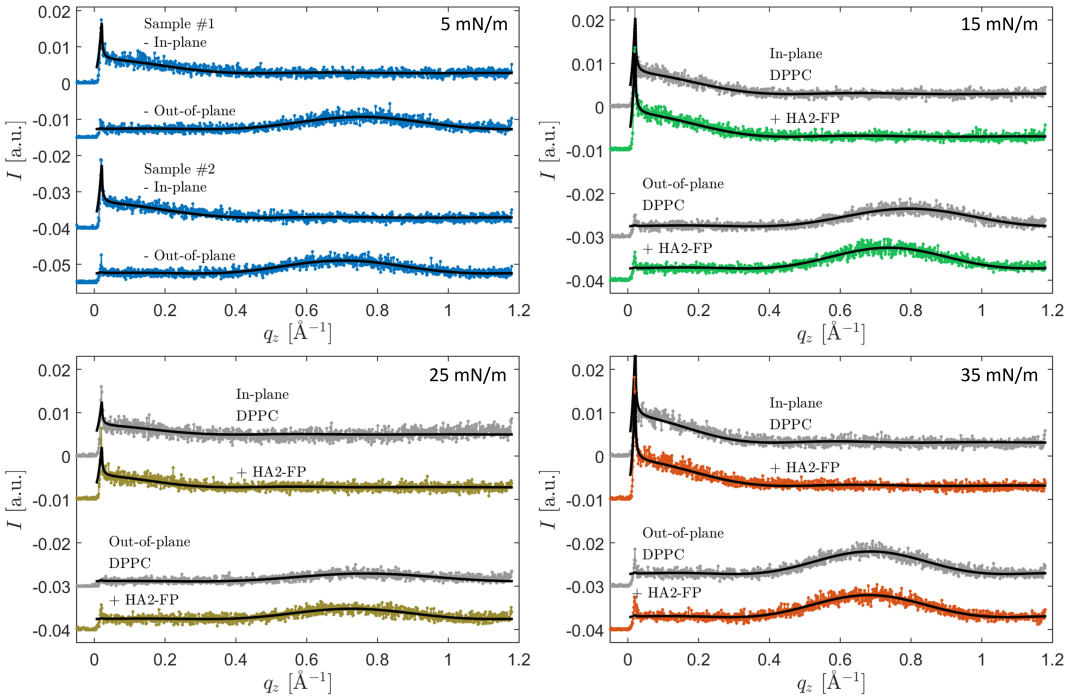

Figure 5.8: Vertical intensity distribution along the Bragg rods of DPPC films before (*gray symbols*) and after (*colored symbols*) the injection of HA2-FP and fits (*black lines*).

Figure 5.10 shows the obtained reflectivity data and the corresponding electron density profiles on the interaction of HA2-FP with DPPC monolayers. Also in these measurements, no effects of the peptides on a highly compressed DPPC film at 35 mN/m were observed. At an initial compression of 5, 15, and 25 mN/m, the electron density of the tailgroups strongly increased, indicating that the HA2-FPs inserted deeply into the hydrophobic region. At the same time, the maximum electron density of the headgroups decreased, which can be assigned to a lateral displacement of lipids. Scans at different positions at the surface showed that the peptides did not spread evenly over the whole surface. At larger distances to the location where the peptides were injected, the electron density profiles were more similar to compressed DPPC films in absence of FPs. However, as the electron density in the headgroups was always smaller or equal compared to a pure DPPC monolayer at a similar surface pressure, while the electron density of the tailgroups was always larger or equal, it is evident that the peptides are mainly located in the hydrophobic region. This insertion mode implies that HA2-FP tends to induce negative curvature in DPPC membranes [291].

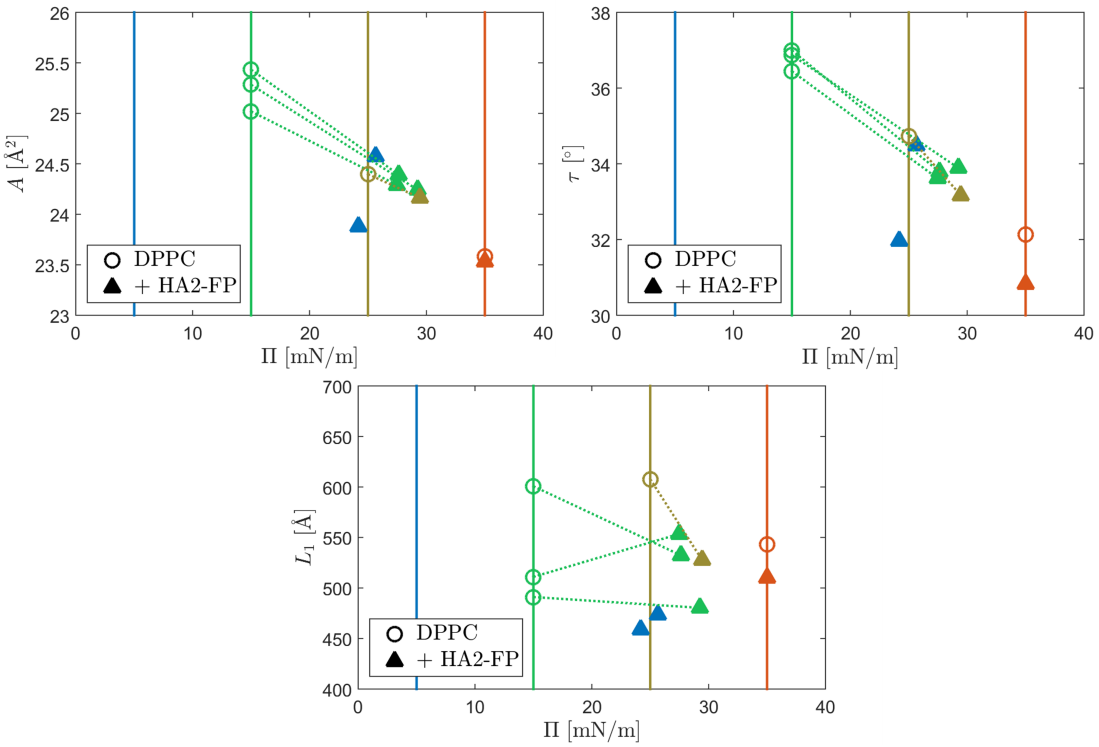

Figure 5.9: Area per unit cell A, tilt angle τ, and mean crystallite dimension L_1 before and after the injection of HA2-FP shown as a function of the surface pressure Π. The *colors* represent the different starting pressures of 5 mN/m (*blue*), 15 mN/m (*green*), 25 mN/m (*brown*), and 35 mN/m (*red*). At 5 mN/m, before the injection of HA2-FP, no crystalline structure was observed.

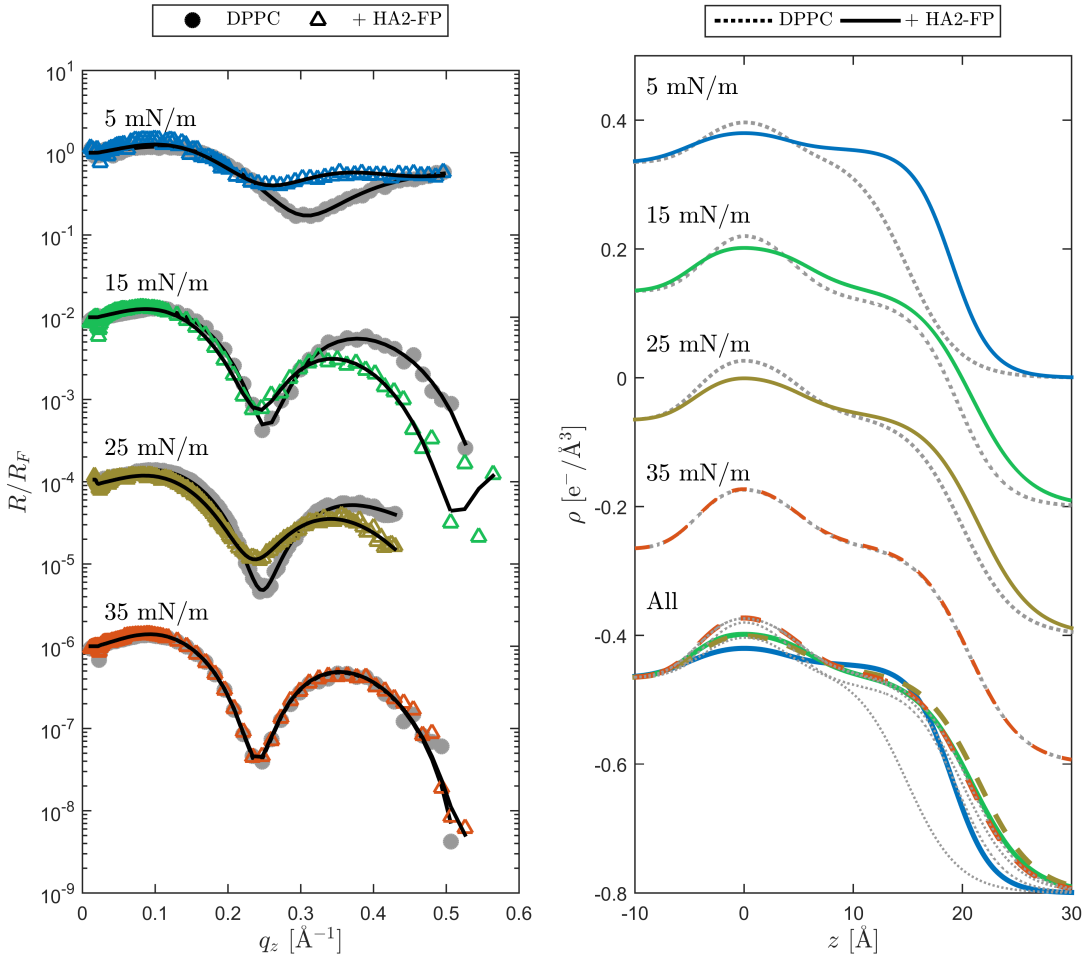

Figure 5.10: XRR data (*left*) and electron density profiles (*right*) of DPPC films before (*gray*) and after (*colored*) the addition of HA2-FP and fits (*black*). Reflectivity curves and electron density profiles are shifted vertically for better visualization. For better comparability, the profiles of all surface pressures are additionally displayed overlaid.

5.7 The interaction of HA2-FP with DPPA Langmuir films

Typical GID patterns of DPPA can be seen in figure 5.11. At high compression of 35 mN/m, the tilt angle is zero and the molecules are arranged in a hexagonal lattice. Therefore, only a three-fold degenerate in-plane reflection is observed. At 15 mN/m, a distorted hexagonal lattice in combination with a tilt towards the nearest neighbor lipid along $\boldsymbol{a}$ results in a two-fold degenerate out-of-plane and an in-plane reflection similar to DPPC [178]. However, for DPPA, the reflections strongly overlap. As the in-plane maximum is more pronounced, it was possible to fit its lateral and vertical intensity distribution by the usual approach. For the out-of-plane maximum, the procedure had to be adapted. The overlap of the Bragg rods was included into the models by superposing the corresponding fit functions with the in-plane profiles, multiplied by an adjustable scaling factor. The phase transition between tilted and untilted phase was found to proceed very slowly at 25 mN/m, so that both phases were observed at this surface pressure.

Figure 5.12 and 5.13 summarize the results of the GID and XRR measurements on HA2-FPs that interact with anionic DPPA Langmuir films at surface pressures of 15, 25, and 35 mN/m. Additionally, the time course of the surface pressure or the trough surface area during the experiments is shown in figure 5.13. The investigations on DPPA monolayers were conducted at constant surface pressure for all peptides with exception of the 15 and 25 mN/m measurements with HA2-FP. It was found that the propensity of HA2-FPs to insert into monolayers at surface pressures below 30 mN/m is so high that at the applied concentration, even the maximum available trough area was not sufficient to keep the surface pressure at the desired values. Therefore, the trough area was kept constant at those starting surface pressures instead. At both starting pressures, the injection of HA2-FP led to a fast rising of the surface pressure to approximately 26 mN/m. For a few minutes, the pressure stayed at this level, before a slower increase occurred. During the observation period of 2-3 hours, the slope decreased, but a saturation value was not reached. The two different time scales in which the pressure increased suggest that there are two distinct processes of how HA2-FPs penetrate the lipid layer.

The GID data show that the insertion of HA2-FPs into the DPPA monolayer reduced the size of the unit cell, induced a transition into an untilted state, and increased the mean crystallite size. Comparing the lattice parameters of the DPPA films after the injection of HA2-FP with the reference measurements of DPPA at 35 mN/m reveals that the shape and size of the crystallites depends mainly on the surface pressure, regardless if it was caused by reduction of the trough area or addition of the peptides. This is in agreement with the observations for DPPC in section 5.6. Again, it is assumed that HA2-FP mainly inserts into gap regions between crystalline domains. The injection of peptides at 35 mN/m at constant surface pressure led to a slight increase of the trough area, indicating that the peptides were able to penetrate even highly compressed DPPA films. However, the GID measurements showed no effects on the lateral organization of the LC phase.

The XRR measurements showed drastic changes of the vertical layer structure after the insertion of HA2-FP in all cases. The peptides accumulated underneath the film

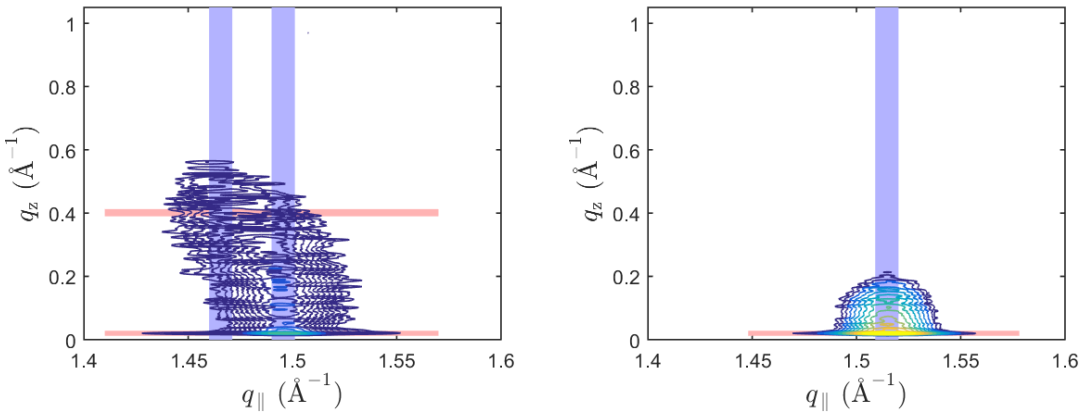

Figure 5.11: Typical GID patterns of DPPA in a tilted (*left*) and an untilted (*right*) LC phase. The colored rectangles illustrate the regions of interest that were considered for the analysis of the Bragg rods. The red areas were integrated vertically yielding the intensity as a function of $q_\parallel$ and the blue areas were integrated horizontally yielding the intensity as a function of q_z.

due to electrostatic interactions. Their effect on the headgroup region was relatively low. The electron density altered by a few percent and it broadened slightly. The most pronounced effect occurred in the tailgroup area, as its electron density decreased dramatically. At an initial compression of 25 and 35 mN/m, a maximum reduction by approximately 35 % was observed, at 15 mN/m even by 65 %.

The decrease of the electron density in the tail region can be explained by a formation of HA2-FP clusters that displace the lipid molecules. As it was shown in figure 5.2, the electron density of the layer that formed above the surface when HA2-FP was injected underneath a clean water surface was less than $0.1\,e^-/Å^3$. Therefore, the different levels of decrease of the tailgroup electron density can be understood as an average of different proportions of DPPA domains and HA2-FP clusters in which the peptides align similarly as at a lipid-free surface. Presumably, the peptides did not spread homogeneously over the whole monolayer, so that the electron density profile was similar to a compressed DPPA layer in large distances to the location where the peptides have been injected. The assumption of an accumulation of the peptides between the LC domains is in good agreement with the minor influence of the presence of HA2-FP on the lattice parameters found with GID. Based on these observations, the two different regimes in the increase of the surface pressure upon the addition of HA2-FP at 15 and 25 mN/m could be explained by a fast insertion of the peptides into defect regions of the LC structures and a slow incorporation into transient gaps, which emerge in the course of the cluster formation.

Besides electrostatic contributions, the reason for the different insertion behavior of HA2-FP in DPPC and DPPA membranes presumably lies in their different ratio of headgroup to tailgroup cross section [307]. While both lipids consist of equally constructed hydrocarbon chains, their hydrophilic heads strongly differ in size. The headgroup of DPPC occupies a larger area compared to the area requirement by its hydrophobic segment. For DPPA, the situation is the opposite and the hydrocarbon chains tend to have

a slightly higher cross section than the headgroups. Presumably, it is energetically favorable for the HA2-FP to mix with lipids that are able to shield its hydrophobic regions in addition to their own tailgroups from interactions with water. At the air-water interface, this property is only provided by DPPC and not by DPPA. In membrane systems that allow the formation of curvature, the hydrophobic space shielded by the headgroups can be increased by the development of a negative curvature. Although no accumulation of HA2-FP in the hydrophobic region of DPPA films was observed, it is thus likely that the presence of molecules with small headgroups tends to promote the ability of HA2-FP to induce negative curvature.

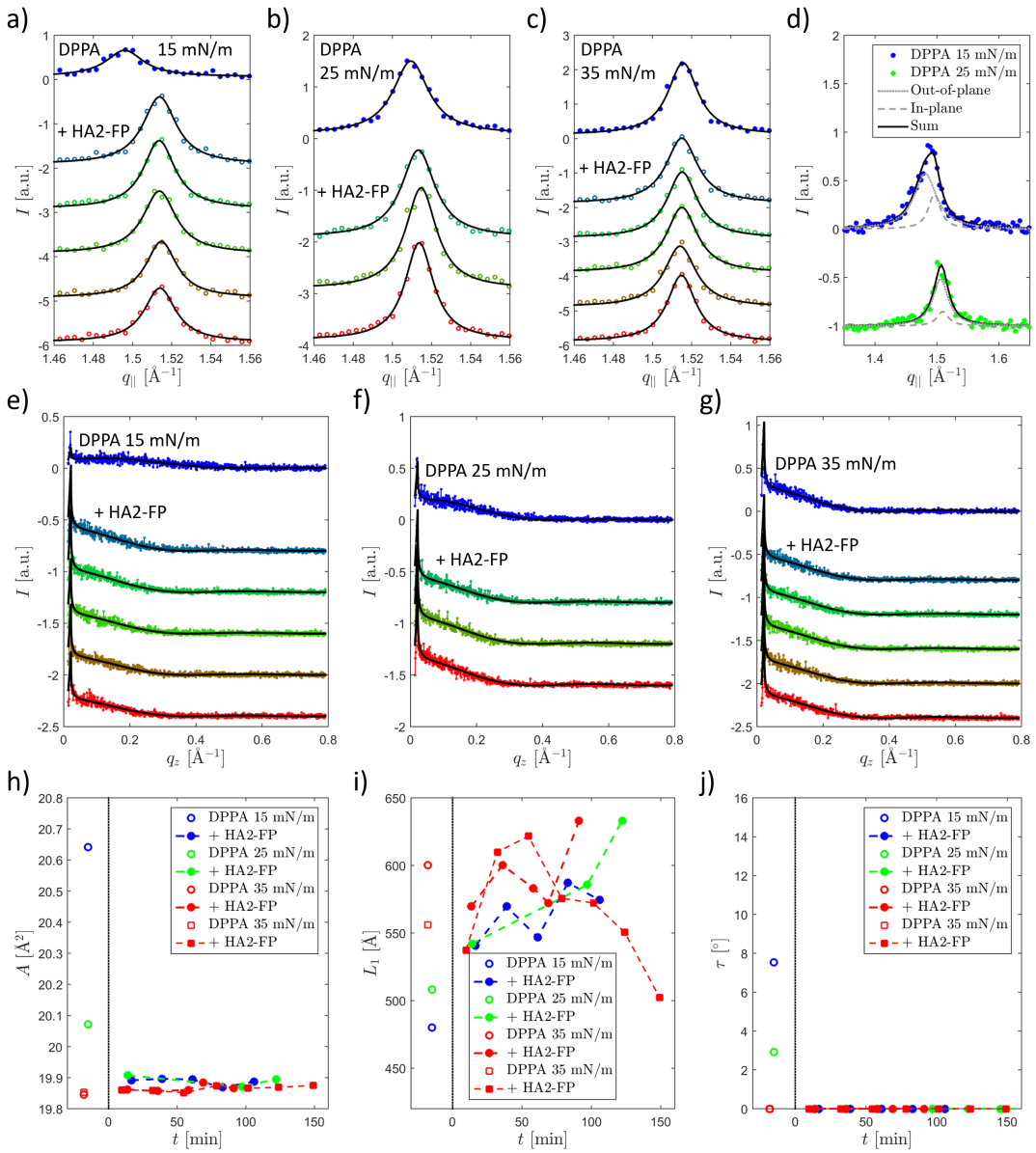

Figure 5.12: Intensity distribution of in-plane GID reflections of DPPA films in absence and presence of HA2-FP (*colored*) and fits (*black*) at starting pressures of a) 15 mN/m, b) 25 mN/m and c) 35 mN/m. d) Out-of-plane reflections. Intensity distribution along the Bragg rods that occurred at the smallest $q_{||}$ value (*colored*) and fits (*black*) at starting pressures of e) 15 mN/m, f) 25 mN/m and g) 35 mN/m. h) Unit cell area A, i) mean crystallite size L_1 and j) tilt angle τ obtained from the GID data as a function of time t. The injection of HA2-FP was conducted at $t = 0$.

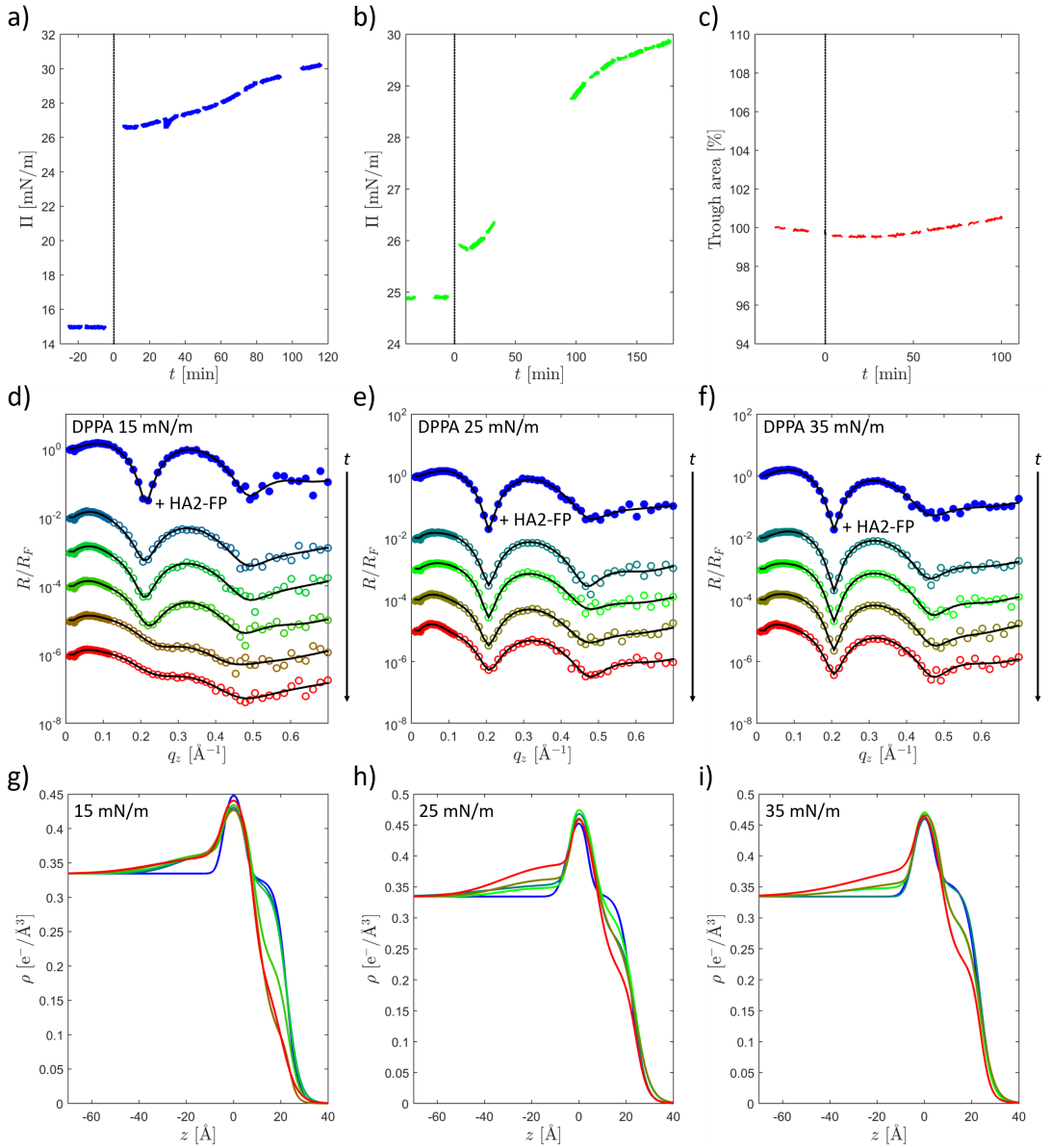

Figure 5.13: Surface pressure of DPPA films interacting with HA2-FP as a function of time t at starting pressures of a) 15 mN/m and b) 25 mN/m. c) Percentage adjustment of the trough area to keep a DPPA film that interacts with HA2-FP at a constant surface pressure of 35 mN/m as a function of time t. The peptides were injected at $t = 0$. XRR scans taken before and after the addition of HA2-FP (*colored*) and fits (*black*) at starting pressures of d) 15 mN/m, e) 25 mN/m and f) 35 mN/m. Corresponding electron density profiles at starting pressures of g) 15 mN/m, h) 25 mN/m and i) 35 mN/m.

5.8 The interaction of the fusion loops of TBEV and VSV with DPPA Langmuir films

Figure 5.14 to 5.17 summarize the results of the GID and XRR measurements on TBEV-FLs and VSV-FLs interacting with DPPA Langmuir films at surface pressures of 15, 25, and 35 mN/m. The time course of the trough surface area during the experiments is shown in figures 5.15 and 5.17. Pronounced changes of the trough surface area that were required to maintain a constant surface pressure after the addition of peptides were only observed at 15 mN/m. Three hours after the injection of VSV-FL, the area expanded by 4.2 %. For TBEV-FL, the slope of the trough area as a function of time increased slightly and the surface enlarged by 1 % between one and three hours after the injection. At higher surface pressures, the area was mostly constant. The area increase at 15 mN/m was accompanied by structural changes of the crystalline order for both FLs. The injection of TBEV-FL reduced the mean crystallite size and increased the size of the unit cell and the tilt angle. For VSV-FL, the changes of the unit cell and the crystallite size were small, but the tilt angle increased strongly. Therefore, it is assumed that the FLs do not exclusively interact with gap regions between LC crystallites.

Pronounced changes of the lattice parameters of a DPPA film at 15 mN/m in presence of TBEV-FL occurred after approximately one hour, coincident with the begin of the increase of the trough surface. The electron density profiles obtained from the XRR scans show that the peptides accumulated underneath the headgroups, forming an about 10 Å thick layer. This was also observed at 25 and 35 mN/m, but the adsorbate layer formed immediately after the injection, accompanied by a slight increase of the unit cell area. Presumably, the anchor unit contributes to the adsorption of the peptides underneath the DPPA film, as it increases the electrostatic attraction. However, it was found that small peptides with a high amount of positively charged residues, like lysine, tend to reduce the repulsion between negatively charged lipids in Langmuir films in the LC phase, causing a condensing effect [308]. Therefore, it is likely that the increase of the lattice spacing was induced by the actual FL sequence, not by the anchor unit. In fact, the electron density profiles show that the peptides inserted into the DPPA layer with a limited penetration depth at all surface pressures, as the electron density of the hydrophobic region increased close to the headgroups, while it reduced at the end of the hydrocarbon chains. This reduction was not very pronounced and can be assigned to the enlargement of the unit cell. The increase close to the headgroups is an indication for the insertion of the aromatic anchors of TBEV-FL W101 and F108 that is thought to be limited to a maximum penetration depth into the hydrocarbon layer of 6 Å [205]. A rough estimation of the penetration depths based on the electron density profiles shows that our results are in good agreement with this value. For this purpose, the reference profiles and the profiles that showed the most pronounced effect after the addition of TEBV-FL were shifted, so that their inflection points in the transition area between tailgroups and air are at $z = 0$ Å (like it was done in figure 5.15). Then, the point of intersection in the hydrophobic region between the profile obtained before and after the addition of TBEV-FLs was determined and the absolute value of the corresponding

z position was subtracted from the total thickness of the hydrophobic region of the reference profile. In case of the 15 mN/m measurement, the thickness was corrected by the changed tilt angle. This procedure yields penetration depths of about 7, 6 and 4 Å at 15, 25 and 35 mN/m. Presumably, the insertion of the aromatic residues caused the increase of the unit cell area due to steric interactions and contributes to the stability of the pronounced adsorbate layer.

The VSV-FLs accumulated underneath the headgroups, forming an approximately 25 Å thick layer at all surface pressures. At 35 mN/m, the GID measurements showed no major changes of the lattice parameters induced by VSV-FLs. This observation is confirmed by the electron density profiles that show no modulations of the electron density within the lipid layer. The reduction of the unit cell area and the tilt angle that occurred at 25 mN/m was most likely due to a slow transition from a tilted into an untilted phase and cannot be assigned to the interaction with the FLs. However, the reflectivity data showed a penetration of the peptides into the hydrophobic area. The effect is similar to the behavior of TBEV-FL, suggesting an insertion of aromatic residues. The penetration depth is estimated to be 5 Å. It should be mentioned again that the investigated peptide only contains the residues Y116 and A117 and not W72 and Y73, which constitute the bipartite FL of VSV. Further, the sequence contains the aromatic amino acids W104 and F109 that could also contribute to the observed insertion. At 15 mN/m, the electron density profiles show more drastic changes in the hydrophobic area. To obtain an adequate fit, it was necessary to split the hydrophobic region into two separated sublayers, an approximately 8 Å thick layer with a high electron density close to the headgroups and a layer with low electron density at the end of the hydrocarbon chains. The minor changes of the unit cell area and the crystallite size compared to the drastic reduction of the electron density in the tailgroups suggest that the peptides did not only penetrate the membrane via aromatic anchors. Possibly, the peptides also inserted in gap regions between crystallites and displaced the lipids by forming clusters like it was observed for HA2-FP. This seems likely as, in contrast to TBEV-FL, VSV-FL was found to form layers at a clean water surface (see section 5.4).

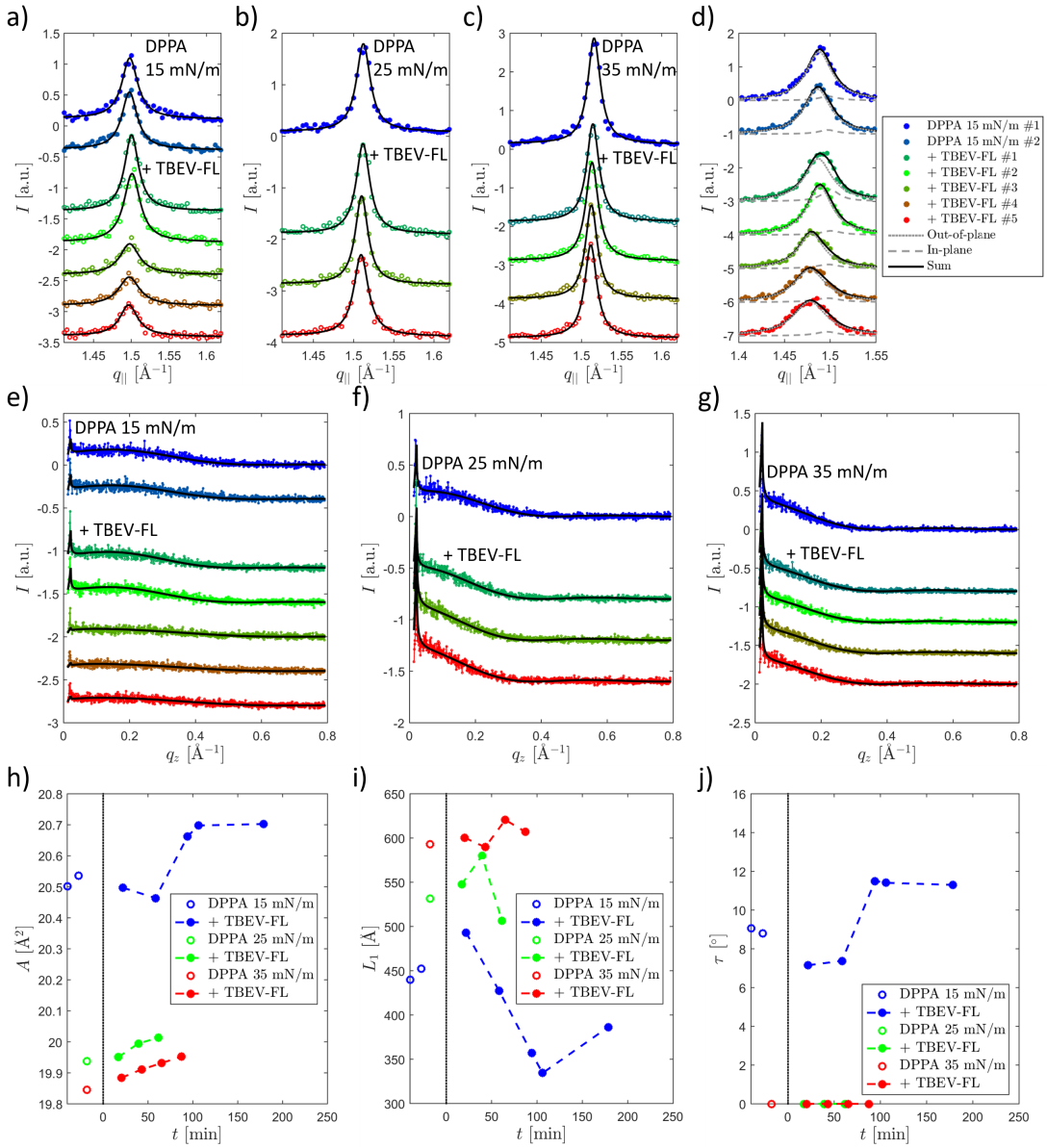

Figure 5.14: Intensity distribution of in-plane GID reflections of DPPA films in absence and presence of TBEV-FL (*colored*) and fits (*black*) at surface pressures of a) 15 mN/m, b) 25 mN/m and c) 35 mN/m. d) Out-of-plane reflections. Intensity distribution along the Bragg rods that occurred at the smallest $q_{||}$ value (*colored*) and fits (*black*) at surface pressures of e) 15 mN/m, f) 25 mN/m and g) 35 mN/m. h) Unit cell area A, i) mean crystallite size L_1 and j) tilt angle τ obtained from the GID data as a function of time t. The injection of TBEV-FL was conducted at $t = 0$.

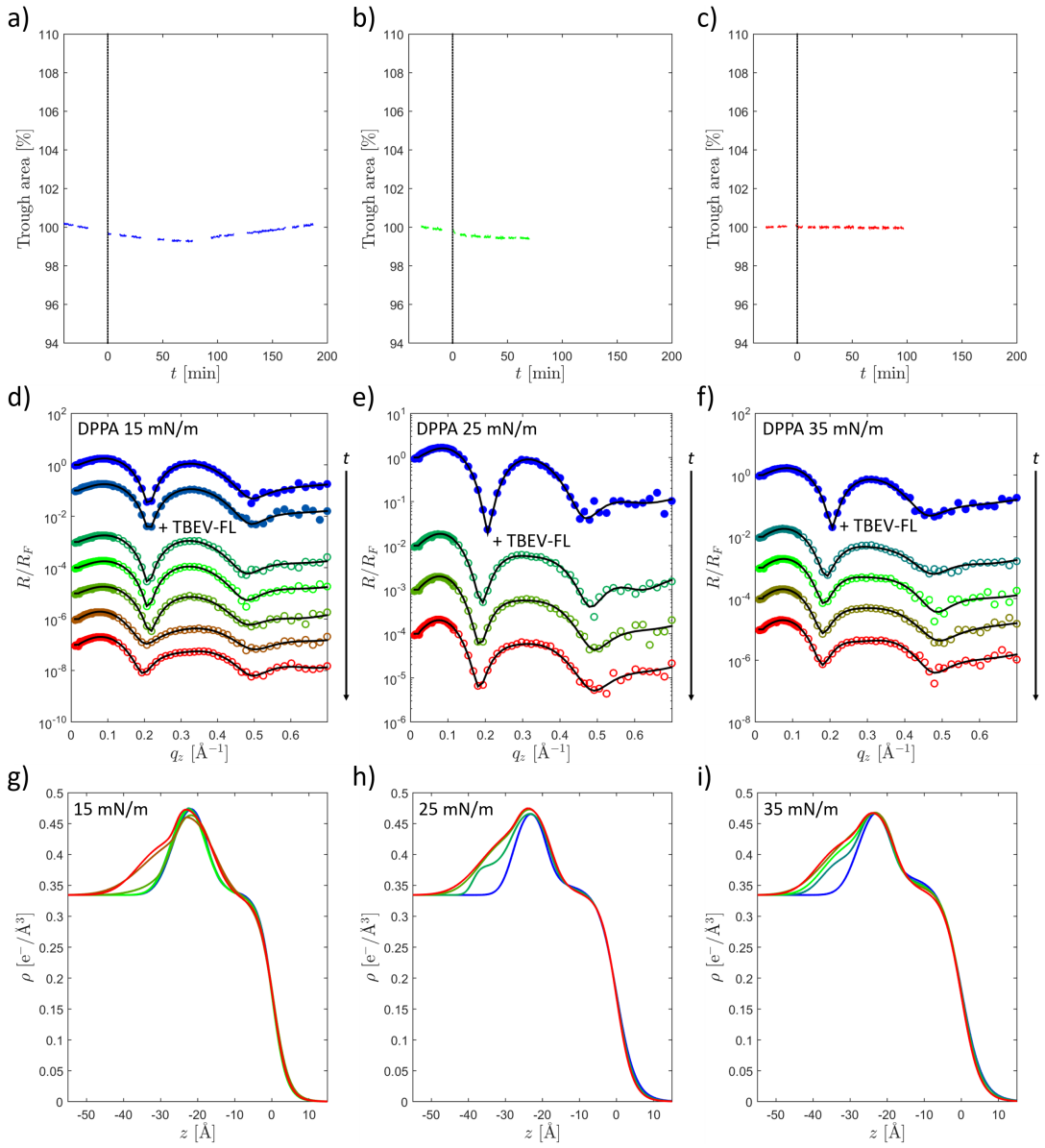

Figure 5.15: Percentage adjustment of the trough area to keep DPPA films interacting with TBEV-FL at constant surface pressures of a) 15 mN/m, b) 25 mN/m and c) 35 mN/m as a function of time t. The peptides were injected at $t = 0$. XRR scans taken before and after the addition of TBEV-FL (*colored*) and fits (*black*) at surface pressures of d) 15 mN/m, e) 25 mN/m and f) 35 mN/m. Corresponding electron density profiles at surface pressures of g) 15 mN/m, h) 25 mN/m and i) 35 mN/m.

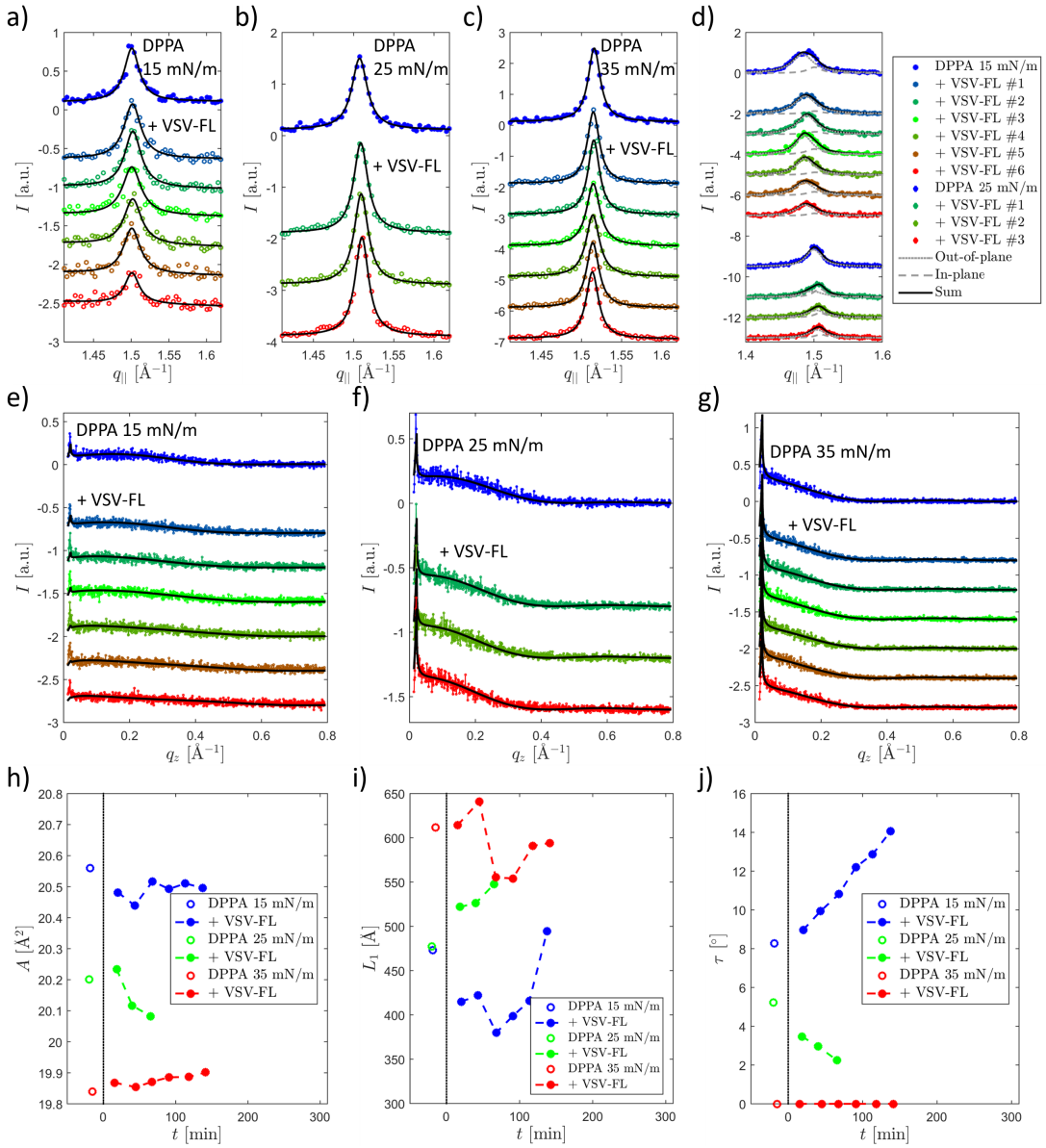

Figure 5.16: Intensity distribution of in-plane GID reflections of DPPA films in absence and presence of VSV-FL (*colored*) and fits (*black*) at surface pressures of a) 15 mN/m, b) 25 mN/m and c) 35 mN/m. d) Out-of-plane reflections. Intensity distribution along the Bragg rods that occurred at the smallest $q_{||}$ value (*colored*) and fits (*black*) at surface pressures of e) 15 mN/m, f) 25 mN/m and g) 35 mN/m. h) Unit cell area A, i) mean crystallite size L_1 and j) tilt angle τ obtained from the GID data as a function of time t. The injection of VSV-FL was conducted at $t = 0$.

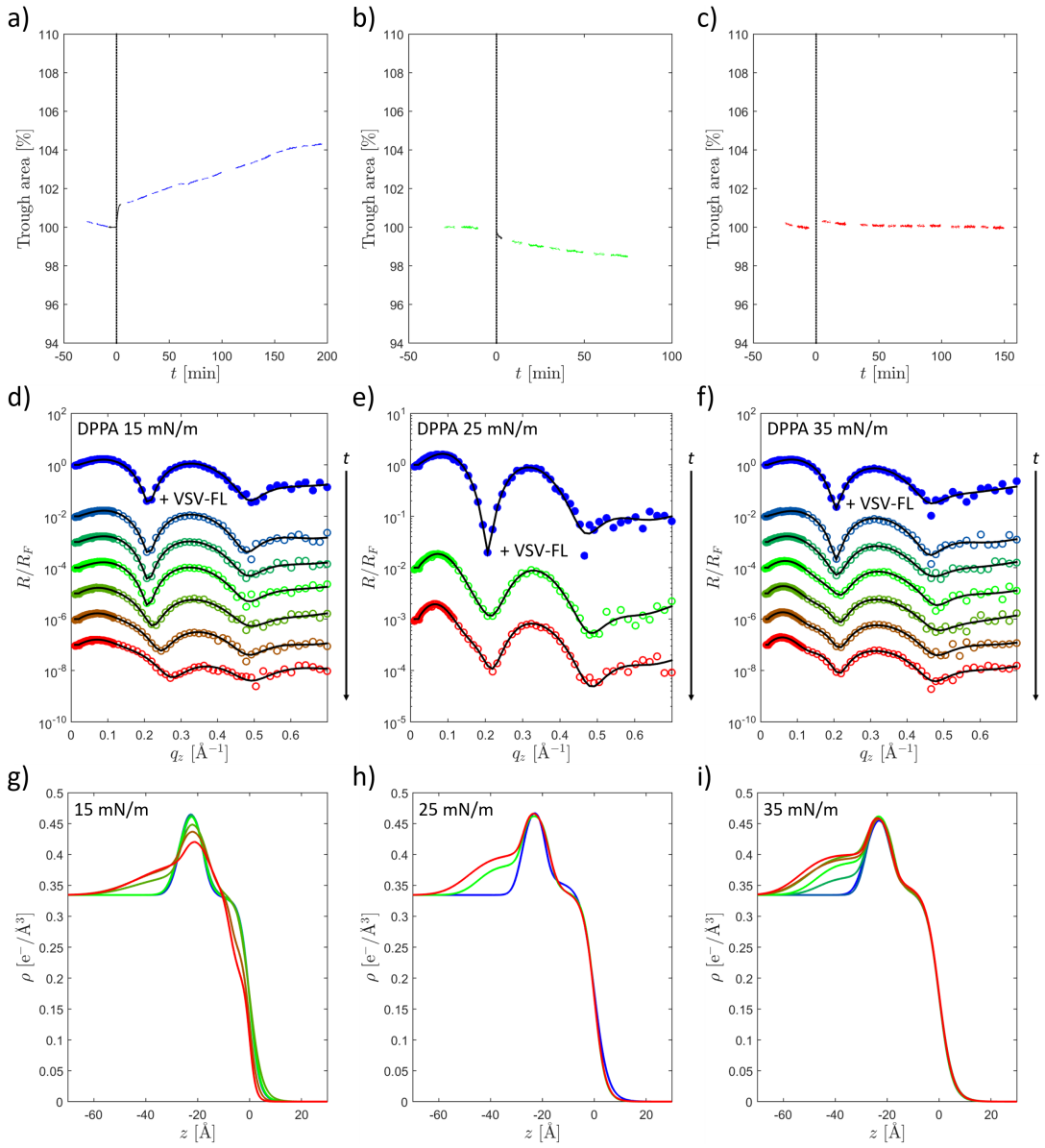

Figure 5.17: Percentage adjustment of the trough area to keep DPPA films interacting with VSV-FL at constant surface pressures of a) 15 mN/m, b) 25 mN/m and c) 35 mN/m as a function of time t. The peptides were injected at $t = 0$. XRR scans taken before and after the addition of VSV-FL (*colored*) and fits (*black*) at surface pressures of d) 15 mN/m, e) 25 mN/m and f) 35 mN/m. Corresponding electron density profiles at surface pressures of g) 15 mN/m, h) 25 mN/m and i) 35 mN/m.

5.9 The interaction of VSV-TMD with DPPA Langmuir films

Figure 5.18 and 5.19 summarize the results of the GID and XRR experiments on VSV-TMDs interacting with DPPA Langmuir films at surface pressures of 15 and 35 mN/m. The time course of the trough surface area during the experiments is shown in figure 5.19. At 15 mN/m, the injection of VSV-TMD caused a strong increase of the surface area. After two and a half hours, an expansion of 8 % was necessary to stabilize the surface pressure. The opening speed of the barrier was almost constant over the whole period, indicating that the equilibrium was not reached. The effects on the crystalline structure observed with GID were low: the size of the unit cell remained constant and the tilt angle increased only slightly. However, most of the scans revealed a reduced mean crystallite size after the addition of VSV-TMD, indicating that the insertion of the peptides decreased the order of the LC phase. The electron density profiles show that the peptides inserted deeply into the hydrophobic area, as the electron density increased in the corresponding region. A pronounced adsorption layer underneath the headgroups like it has been observed for the other peptides, did not occur. However, a slight increase of the electron density underneath the headgroups in a range of less than 10 Å was still observed.

At a surface pressure of 35 mN/m, trough area, lateral film structure, tilt angle, and mean crystallite size did not change after the injection of VSV-TMD. The electron density profiles show that the high film pressure inhibited the insertion of peptides into the hydrophobic regime and the observed structure did not change at all. Apparently, the peptides did not accumulate underneath the anionic lipid monolayer despite their net charge of +4 at pH 5. Therefore, it is assumed that this also did not happen at 15 mN/m. Instead, the slight increase of the electron density underneath the headgroups at 15 mN/m might be caused by hydrophilic segments of the peptides protruding from the monolayer. This is consistent with the assumption of an α-helical insertion of VSV-TMD. With a length of about 22.5 Å [309], the 15 residues of the TMD of VSV would be able to traverse the whole hydrophobic region of the monolayer forming a single α-helix. The dimensions of the hydrophilic anchor unit are sufficient to span the headgroup region and reach into the subphase.

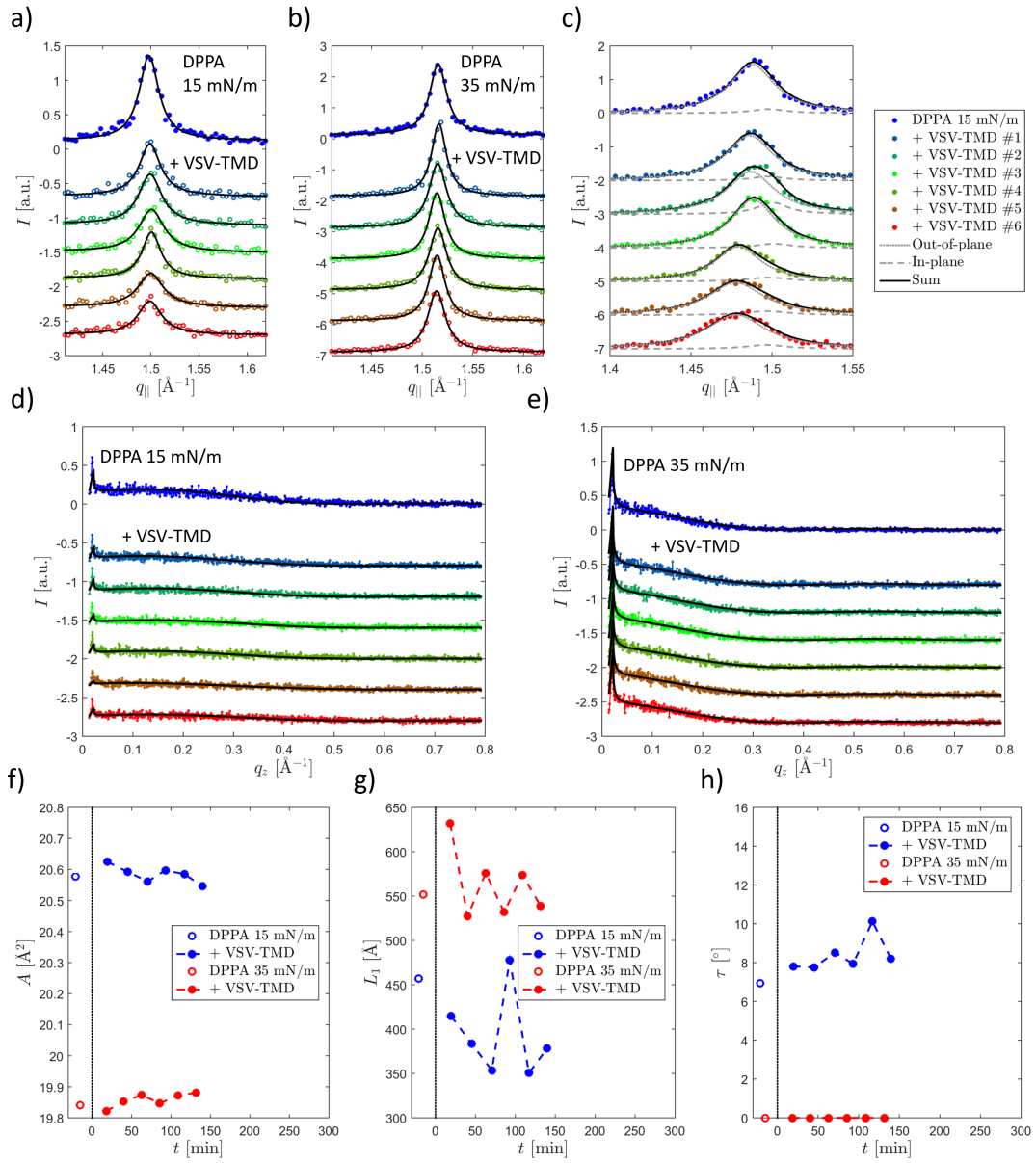

Figure 5.18: Intensity distribution of in-plane GID reflections of DPPA films in absence and presence of VSV-TMD (*colored*) and fits (*black*) at surface pressures of a) 15 mN/m and b) 35 mN/m. c) Out-of-plane reflections. Intensity distribution along the Bragg rods that occurred at the smallest $q_{||}$ value (*colored*) and fits (*black*) at surface pressures of d) 15 mN/m and e) 35 mN/m. f) Unit cell area A, g) mean crystallite size L_1 and h) tilt angle τ obtained from the GID data as a function of time t. The injection of VSV-TMD was conducted at $t = 0$.

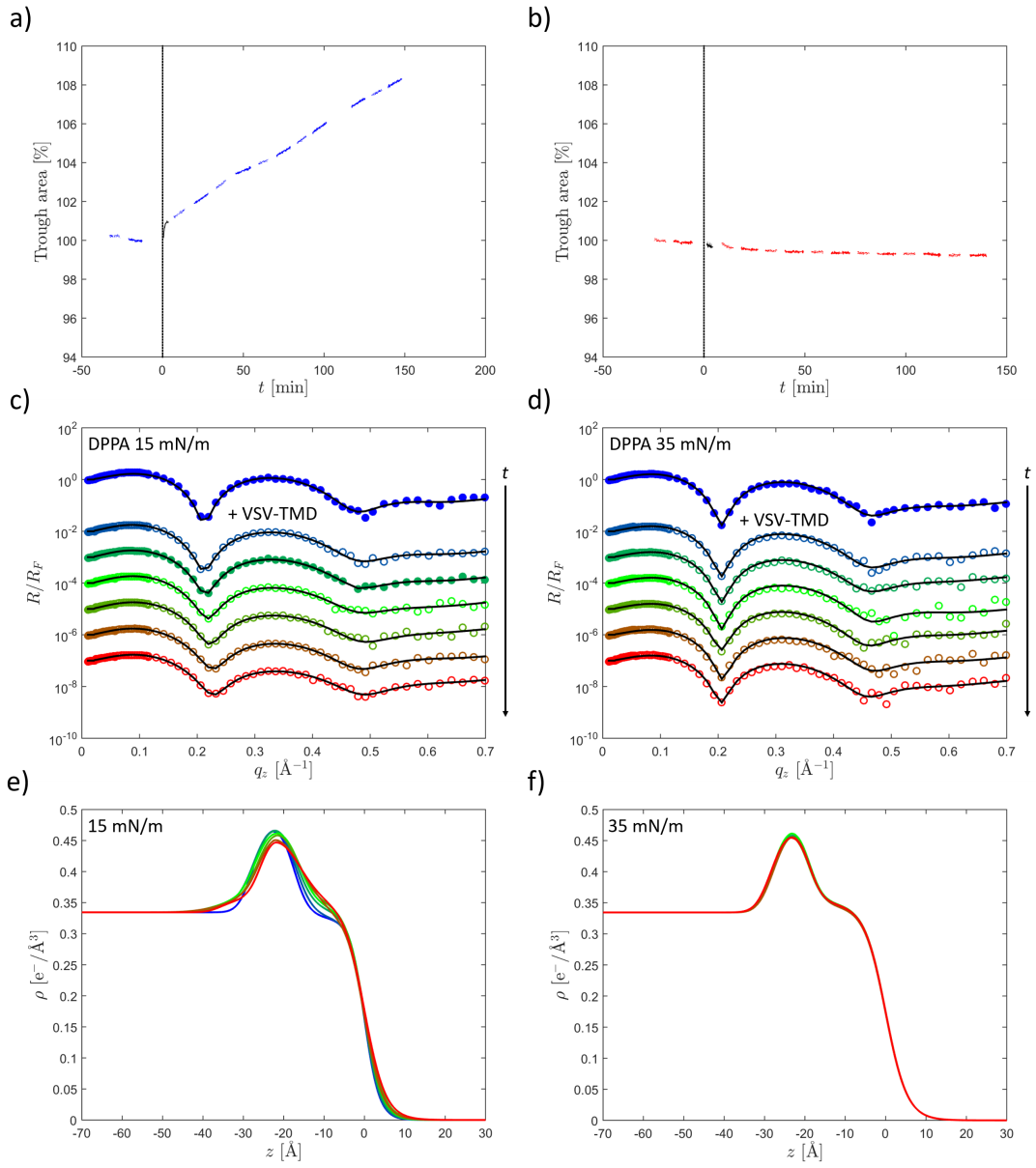

Figure 5.19: Percentage adjustment of the trough area to keep DPPA films interacting with VSV-TMD at constant surface pressures of a) 15 mN/m and b) 35 mN/m as a function of time t. The peptides were injected at $t = 0$. XRR scans taken before and after the addition of VSV-TMD (*colored*) and fits (*black*) at surface pressures of c) 15 mN/m and d) 35 mN/m. Corresponding electron density profiles at surface pressures of e) 15 mN/m and f) 35 mN/m.

5.10 Conclusion

In this chapter, the interaction of fusogenic peptides with Langmuir monolayers was investigated. It was found that the insertion mode of HA2-FP strongly depends on the membrane composition. The peptide was incorporated in the hydrophobic region of DPPC membranes, while there are indications that it formed clusters in DPPA monolayers. However, in both cases, HA2-FP had a high propensity to penetrate the monolayer and to increase the surface pressure by displacing the lipid molecules.

In contrast, the effects on the surface pressure of the FLs of TBEV and VSV were more subtle. In agreement with the assumption that both sequences mainly interact with membranes via aromatic anchors, a penetration depth of a few Ångströms that reduced with increasing surface pressure was determined for these peptides [125, 205]. Both FLs formed a highly defined adsorbate layer underneath the headgroups. Possibly, this effect is caused by electrostatic interactions of the cationic anchor unit with the anionic DPPA monolayer. However, it was found that VSV-TMD does not adsorb at the Langmuir film despite the anchor unit and a positive net charge of +4. Therefore, the tendency of TBEV-FL and VSV-FL to attach to the membrane surface might be characteristic for the actual fusogenic sequences and part of their function in the viral membrane fusion process. While VSV-TMD did not affect the structure of highly compressed DPPA monolayers, it inserted deeply into the hydrophobic region of DPPA films at 15 mN/m, reducing the mean crystallite size of the LC phase.

While in the first project high pressure techniques were applied to induce and examine membrane remodeling processes, the high structural resolution of surface-sensitive methods was exploited in this study to investigate interaction mechanisms of membranes at ambient pressure. Combining both experimental approaches to study membrane processes at high hydrostatic pressures is a difficult task. Obviously, high pressure studies are not possible at the air-water interface and thus model membrane systems are needed that are stable on a solid substrate at full hydration. In the next chapter, an XRR study on the influence of cholesterol on the behavior of solid-supported DMPC multilayers at high hydrostatic pressure is presented. It was found that cholesterol promotes the stability of multilayer stacks at full hydration and it was possible to resolve the vertical electron density profile of lipid membranes at pressures of up to 4 kbar.

Chapter 6

DMPC/cholesterol membranes at high hydrostatic pressure

6.1 Objective

In this chapter, the experimental procedure for the investigation of DMPC/cholesterol membranes at high hydrostatic pressures is described in detail and the obtained results are presented and discussed. The study aims on the determination of how cholesterol modulates the pressure-response of phospholipid membranes. A particular focus is the examination of solid-supported DMPC/cholesterol multilayers in order to explore their potential as model systems for high pressure studies. To evaluate the influence of the substrate, the pressure-dependent behavior of multilayers is compared to single bilayers on a solid support and multi-lamellar vesicles in bulk solution. The results have already been published in [153].

6.2 Sample preparation

Solid-supported lipid multilayers were produced on a silicon substrate via spin-coating. For this purpose, silicon wafers were sonicated in 2-propanol (Sigma Aldrich), acetone (Sigma Aldrich) and chloroform (Sigma Aldrich) for 15 min each to remove organic residues from the surface. Then, they were placed in piranha solution (3 parts sulphuric acid (95 %, CHEMSOLUTE) and 1 part hydrogen peroxide (35 %, J. T. Baker)) for 30-45 min. This treatment removes further contaminants and causes the formation of silanol groups at the silicon surface. Thus, the wafers become highly hydrophilic with contact angles below 10°. As the silanol groups are not stable at air, the wafers were stored in ultra pure water (specific electrical resistivity $> 18\,\mathrm{M\Omega cm}$) after this procedure.

Cholesterol (Sigma Aldrich) and DMPC (Sigma Aldrich) in the desired ratios were dissolved in 2-propanol so that the total lipid concentration was 10 wt%. The proportion of cholesterol in the total lipid mass was between 0 and 23.1 wt%. Mennicke and Salditt [144] demonstrated that the number of lipid layers of the resulting multilayer stack is proportional to the concentration of the spin-coating solution. The concentration applied

here led to a deposition of 10-15 bilayers. For the spin-coating process, the wafers were taken out of the storage liquid and fixed in the center of a rotatable disc. Due to their high hydrophilicity, their surfaces remained fully wetted. The water residue was removed by a gas stream. After this, 60 µL of the lipid solution were pipetted onto the wafer surface immediately to avoid that the silanol groups have contact with air. Then, the wafers were rotated with 4000 rpm for 30 s. During this process, the solvent and excess lipids are removed and only an ordered stack of oriented multilayers remains on the surface. After the preparation, the samples were stored in a desiccator where they were stable for several days.

For the experiments, the wafers were mounted in a sample cell and the cell was filled with aqueous buffer solution. To achieve a constant pH value of 7 also at high pressures, Bis-Tris (Sigma Aldrich) buffer with a concentration of 25 mmol/L was used [310].

It was found that the bottom layers of the multilayer stacks were highly stable, while the upper layers partly tended to detach locally, e.g, due to radiation damage. This provided the opportunity to obtain information on the behavior of single bilayers on a solid support. The corresponding procedure of data evaluation is discussed in detail in section 6.5.

For the preparation of multi-lamellar vesicles, DMPC and cholesterol were mixed in the desired ratios by dissolving them in chloroform. The applied cholesterol contents again ranged from 0 and 23.1 mol%. Subsequently, the solvent was removed again. A major amount of the chloroform was dried under a gentle stream of nitrogen and the rest was extracted with a desiccator. Afterwards, the same buffer solution was added as used for the multilayer measurements. The final water content of all samples was 80 wt%. By conducting five freeze-thaw cycles, the mixture was homogenized. For this purpose, the samples were alternately immersed in liquid nitrogen and sonicated at 60 °C.

6.3 Experimental setup

The solid-supported DMPC/cholesterol membranes were investigated with XRR at beamline ID31 [159] of ESRF (Grenoble, France) with a photon energy of 70 keV ($\lambda = 0.177$ Å) and at beamline BL9 [157] of DELTA (Dortmund, Germany) with a photon energy of 27 keV ($\lambda = 0.459$ Å). Figure 6.1 shows a picture of the setup at ID31. At ID31, the beamsize was 50 µm horizontal × 5 µm vertical. Therefore, it was possible to shift the sample laterally after every scan to prevent radiation damage. The beam dimensions at BL9 were 1000 µm horizontal × 100 µm vertical. Here, the lateral sample position was not changed. The specularly reflected and diffusely scattered intensity were recorded simultaneously with the area detectors MAXIPIX [311] (ID31) and PILATUS 100K [312] (BL9). The sample temperature was 20 °C and pressures of 50 to 5000 bar were applied with the high hydrostatic pressure XRR cell introduced in chapter 3.4.

The multi-lamellar vesicles were studied at beamline BL9 [156] of DELTA with a photon energy of 10 keV ($\lambda = 1.240$ Å) via SAXS. The diffraction patterns were captured with a MAR345 image plate detector covering a q range of 0.03 to 0.6 Å^{-1}. For the calibration of the setup, silver behenate [287] was used. The sample temperature was

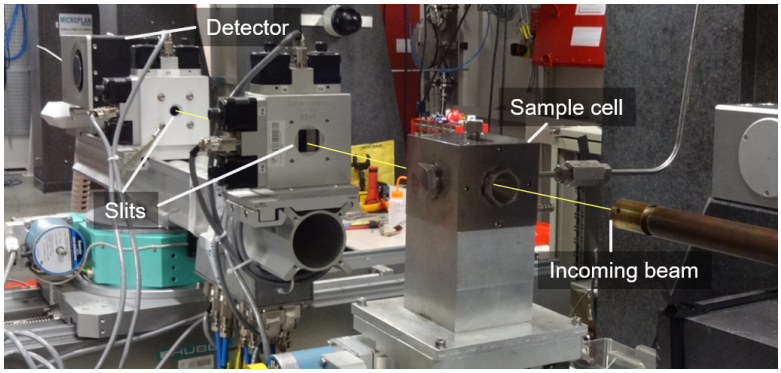

Figure 6.1: The high hydrostatic pressure XRR setup at ID31. The beam path is shown in *yellow*.

20 °C and pressures of 50 to 3500 bar were applied with the high hydrostatic pressure SAXS cell introduced in chapter 3.4.

6.4 Multi-lamellar DMPC/cholesterol vesicles

Figure 6.2 shows a SAXS pattern of multi-lamellar DMPC vesicles at 50 bar that was recorded at BL9. The intensity of the primary beam was blocked with a lead beam stop. Before further processing of the data, the area around the beam stop was masked. Then the intensity was azimuthally integrated and considered as a function of the momentum transfer q. For the determination of the spacing $d = 2\pi/q_{\mathrm{Bragg}}$ of the multi-lamellar structures, the positions of the first order Bragg reflections q_{Bragg} were determined. For this purpose, a linear background was subtracted in a region around the maxima and Pearson type VII distributions [313] were fitted to the data. The corresponding fits can be seen in figure 6.3. Figure 6.4 summarizes the resulting values of the lamellar spacing as a function of pressure for all considered cholesterol concentrations. Based on this data, the phase behavior of the membranes can be determined by comparison with literature values [133–135, 170].

For pure DMPC vesicles, two reflexes were observed indicating a coexistence of two

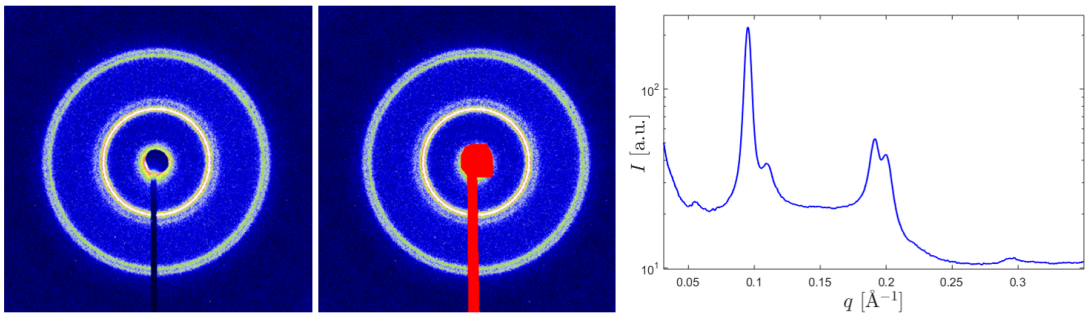

Figure 6.2: SAXS intensity of multi-lamellar DMPC vesicles at 50 bar shown as a raw 2D detector image (*left*), after masking the beam stop (*center*) and as a function of q after azimuthal integration (*right*).

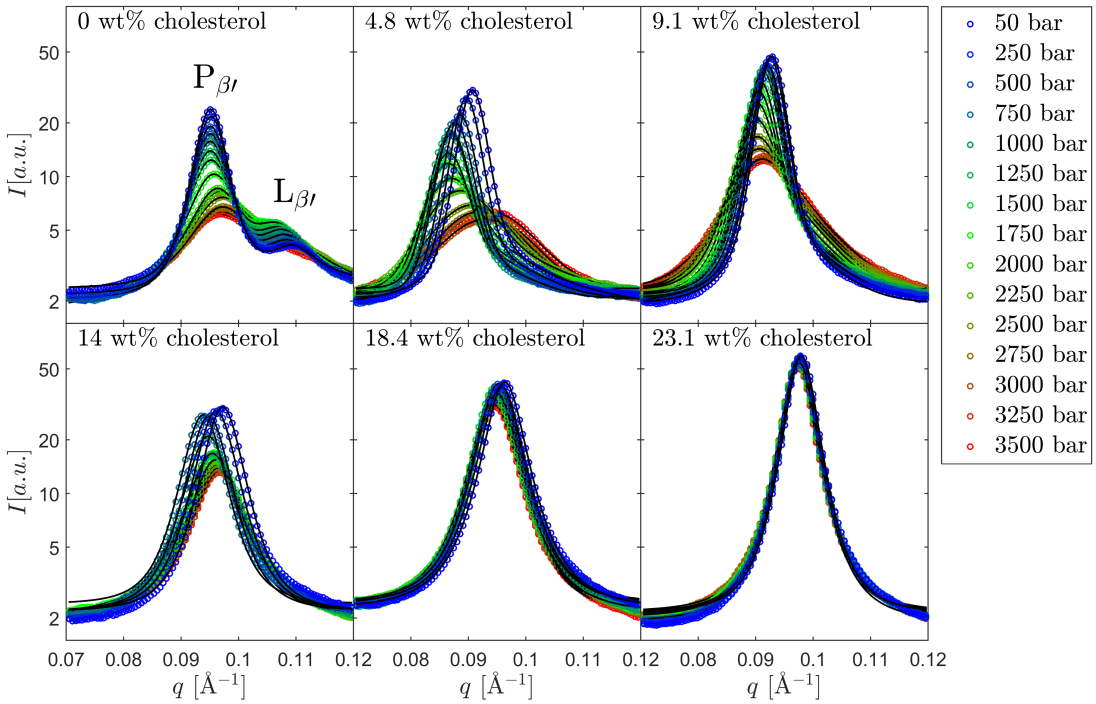

Figure 6.3: SAXS data (*colored points*) and fits (*black lines*) of first order Bragg reflections of multi-lamellar DMPC vesicles that incorporate different amounts of cholesterol upon pressurization.

phases. With a spacing of 66 Å and 58 Å, these can be identified as $P_{\beta\prime}$ and $L_{\beta\prime}$ phase. The $P_{\beta\prime}$ reflection was much more pronounced at 50 bar, but its maximum intensity decreased and its width increased at pressurization. This indicates a reduction of the coherence length of the $P_{\beta\prime}$ phase vertical to the bilayer surfaces. At the same time, the $L_{\beta\prime}$ reflex shifted towards the $P_{\beta\prime}$ reflex, so that both strongly overlapped and were barely distinguishable above approximately 1.5 kbar.

The $L_{\beta\prime}$ phase disappeared already with the addition of low cholesterol concentrations. However, at 4.8 wt% and 9.1 wt% cholesterol, the $P_{\beta\prime}$ reflections exhibited an asymmetry that can be described by the assumption of a second reflection on the right flank of the maxima. This might be caused by a slight separation of a cholesterol-poor phase, which was also observed for DPPC vesicles containing 10 mol% cholesterol [314]. As the intensity of this feature was very weak, it is difficult to determine the spacing accurately. However, the corresponding phase seemed to be almost unresponsive to pressure and had a spacing of 66-68 Å. This behavior is similar to that observed for pure DMPC vesicles in the $P_{\beta\prime}$ phase, which supports the assumption that the origin of the additional reflections lies in cholesterol-poor domains. The lattice constant of the dominant phase increased strongly at pressurization, especially at a cholesterol content of 4.8 wt%. Beyond 2 kbar, this behavior was reversed and a compression occurred. Dur-

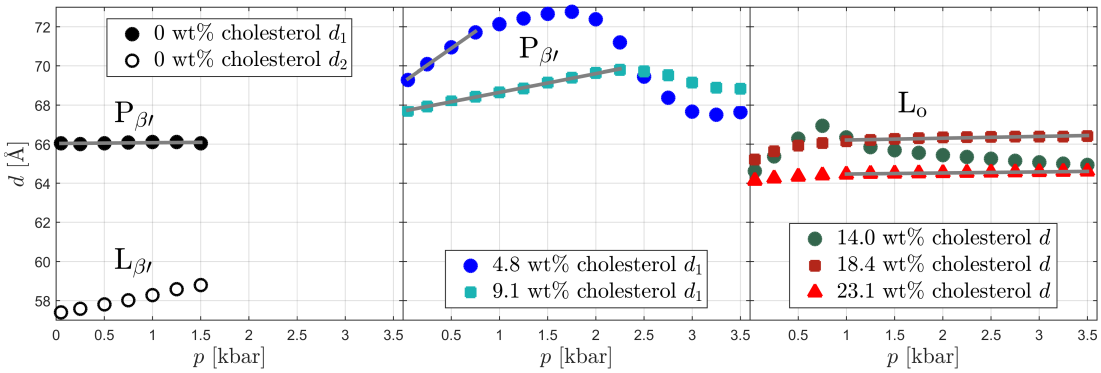

Figure 6.4: Pressure-dependence of the spacing d for different cholesterol concentrations. If two reflections occurred, d_1 denotes the more intense and d_2 the less intense reflection. The gray lines mark the linear regions that were considered for determining the compressibilities. Reprinted with permission from [153]. Copyright © 2019 Elsevier B.V.

ing this compression, the weak reflection disappeared. At a cholesterol concentration of 9.1 wt%, the behavior was similar, but the gradients of the spacing as a function of pressure were smaller and the reversal of slope occurred later at approximately 2.25 kbar. Like in case of pure DMPC vesicles, pressurization caused a broadening of the reflections and a decrease of the maximum intensity at both concentrations.

This changed with a further increase of the cholesterol concentration to 14.0 wt% and more. At 14.0 wt%, the sign of the compressibility was abruptly reversed at 0.75 kbar. Above this pressure, the shape of the reflections hardly changed. For higher concentrations, this stability was evident over the entire pressure range. This behavior indicates that the vesicles entered the liquid ordered L_o phase [139, 170].

6.5 Solid-supported DMPC/cholesterol multilayers

Figure 6.5 shows selected reflectivity curves of solid-supported DMPC multilayers containing different amounts of cholesterol. The curves exhibit three main features: pronounced Bragg reflections at positions that are directly related to the multilayer spacing, short oscillations with a period length $\lesssim 0.01\,\text{Å}^{-1}$ that is related to the thickness of the whole multilayer, and long oscillations with a period length $\gtrsim 0.1\,\text{Å}^{-1}$ that is related to the thickness of the bottom layer. A suppression of the higher-order Bragg reflections and the occurrence of wide oscillations at high q values can be a result of inhomogeneities in the surface coverage and a reduced vertical long-range order of the multilayer [315, 316]. However, repetitive measurements at the same spot on the sample showed that a decline of the Bragg reflections and an increase of the long oscillations can also happen with time. This is most likely due to detachment of bilayers induced by radiation damage [317, 318]. In X-ray experiments, the sample can be damaged by the beam as a result of the formation of free radicals in the water phase or local heating of the sample.

The intensity of the presented reflectivity curves covers approximately 8 orders of

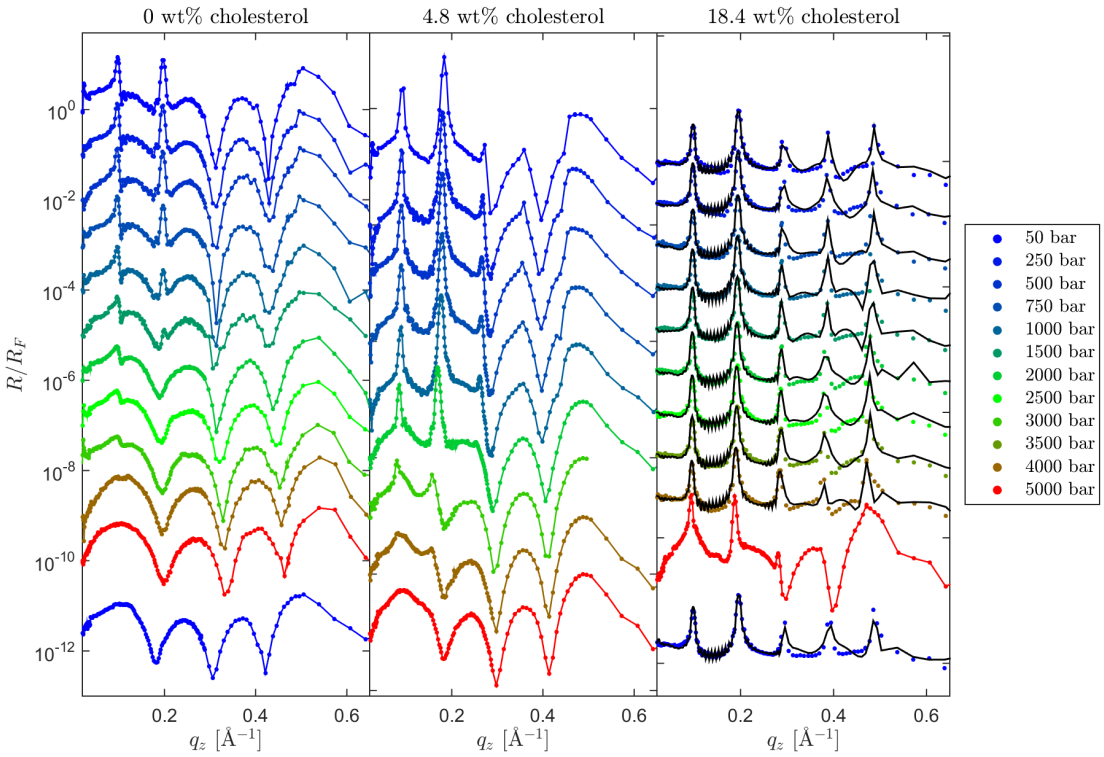

Figure 6.5: XRR data of solid-supported DMPC multilayers containing different amounts of cholesterol upon pressurization. The reflectivity curves are shifted vertically for better visualization. In the 18 wt% cholesterol subfigure, fits are shown in black.

magnitude in the scanned angular range. The incoming intensity was adjusted q-dependent with attenuators. Therefore, the radiation exposure per measuring point increases at high q. At the same time, the footprint of the beam at the sample surface becomes smaller increasing the radiation density even more. This implies that there is a spatially uneven radiation exposure of the sample. In conclusion, multilayer measurements that show distinct long oscillations often cannot be analyzed under the assumption of stationarity and homogeneity. If this is the case, they can no longer be modeled with the fitting procedure described in chapter 3.2. However, calculations of the spacing or the bilayer thickness based on reflex positions and oscillation distances are still possible. The experiments showed that in addition to radiation damage also a pressure-induced detachment of bilayers occurs, especially at low cholesterol content. At a high cholesterol concentration of 18.4 wt%, the stability of the multilayers was sufficient to extract vertical electron density profiles by reconstructing the reflectivity curves with simulations in a pressure range from 50 bar to 4 kbar. In the following, the behavior of the solid-supported membranes at all cholesterol concentrations is first compared on the basis of Bragg reflection positions and oscillation periods and then the obtained electron

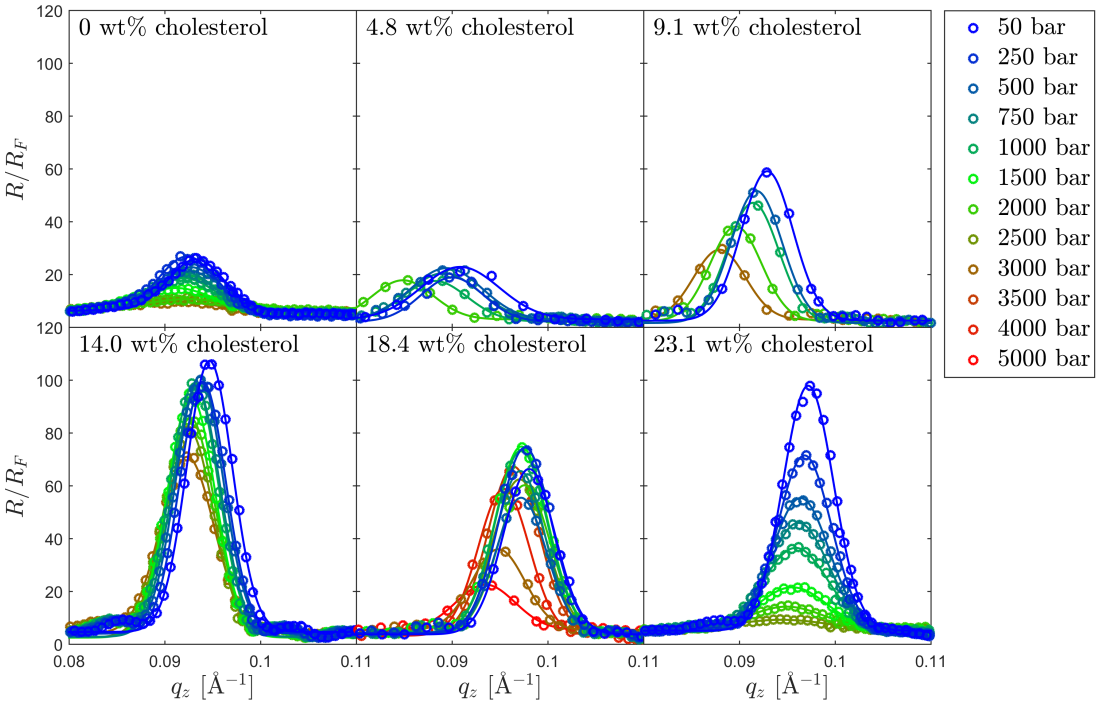

Figure 6.6: First order Bragg reflections of reflectivity curves (*colored points*) and fits (*colored lines*) of solid-supported DMPC multilayers that incorporate different amounts of cholesterol upon pressurization.

density profiles are discussed.

For the calculation of the multilayer spacing, Gaussian distributions were fitted to the first order Bragg reflections. Figure 6.6 shows the corresponding regions of the reflectivity curves with the Gaussian fits. It can be seen that coexistence of phases was not observed in multilayers in contrast to multi-lamellar vesicles. However, the comparison of vesicle and multilayer spacing at 50 bar in figure 6.7 demonstrates that both systems still behaved very similarly. When coexisting phases occurred in vesicles, only the spacing that corresponds to the more intense reflection was considered here. The spacing increased by approximately 4 Å when low amounts of cholesterol were incorporated. Further addition of cholesterol decreased the spacing again slightly below the value of pure DMPC. The good agreement of vesicle and multilayer data indicates that the deposition of 10-15 bilayers is sufficient to largely suppress the influence of the substrate.

Figure 6.8 shows the pressure-dependence of the spacing of multilayers (*filled markers*) for all concentrations. It can be seen that multilayers containing low amounts of cholesterol (*blue symbols*) were highly pressure-responsive and expanded strongly at pressurization compared to pure DMPC (*black symbols*). Apparently, the expansion reduced the stability of the multilayers and led to a detachment of bilayers from the sample surface. A partial detachment of multilayers decreased the intensity of the Bragg

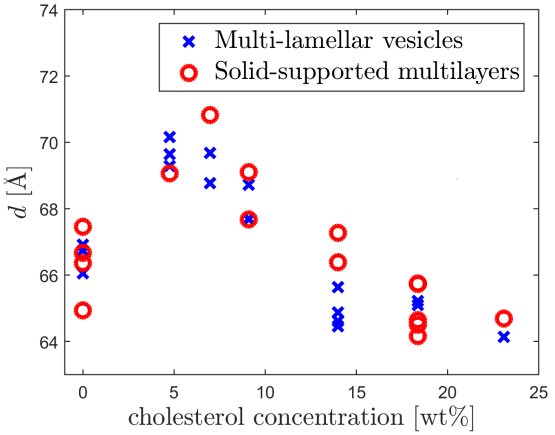

Figure 6.7: Spacing of multi-lamellar vesicles and solid-supported multilayers at 50 bar. Different data points at the same concentration represent different samples. At concentrations where two Bragg reflections were observed in the SAXS data, only the spacing corresponding to the dominant phase is shown. Reprinted with permission from [153]. Copyright © 2019 Elsevier B.V.

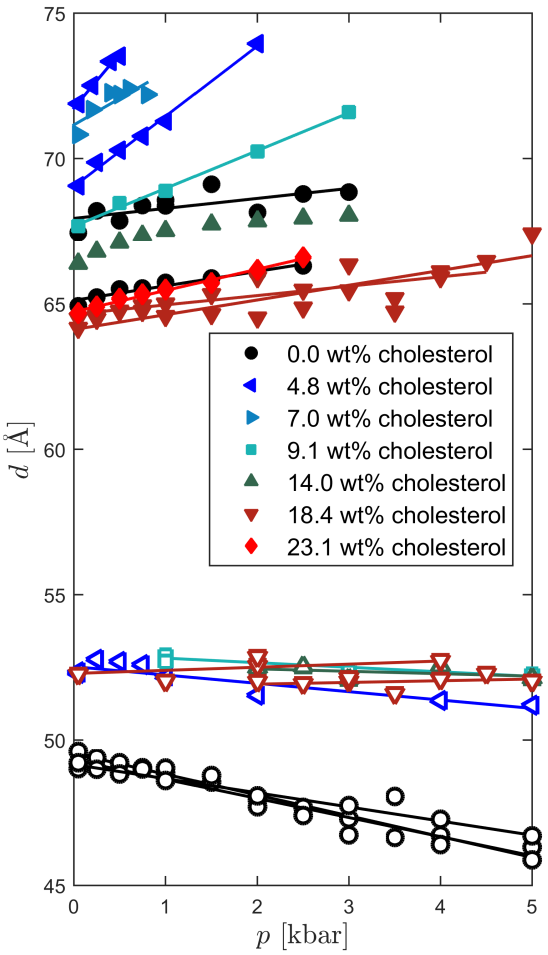

Figure 6.8: Spacing of solid-supported multilayers (*filled markers*) and thickness of solid-supported bilayers (*open markers*) as functions of pressure with linear fits (*lines*) used for the determination of compressibilities. Adapted with permission from [153]. Copyright © 2019 Elsevier B.V.

reflections and is evident in figure 6.6. If a multilayer was damaged so much that no reflexes were observed, this can be seen from missing data points at high pressures in figure 6.8. In this case, typically only the bottom layer remained on the surface.

In contrast, the incorporation of high cholesterol concentrations (*red symbols*) improved the stability of the multilayer stack. The membranes became less pressure-responsive and the pressure-induced vertical expansion diminished. As the reflectivity curves in figure 6.5 prove, no indications of a pressure-induced detachment of layers was observed at 18.4 wt% and the multilayer maintained stability and homogeneity up to 4 kbar. Therefore, it was possible to reconstruct the reflectivity curves in simulations, yielding detailed vertical electron density profiles. The multilayer was modeled under the assumption that the structure of all bilayers is identically (see chapter 3.2). The quality of the fits confirms that this approach is adequate. In figure 6.9, the electron density profiles of the obtained bilayer structure is shown for all pressures. It can be seen that the electron density increased in all sublayers at pressurization. However, this effect was

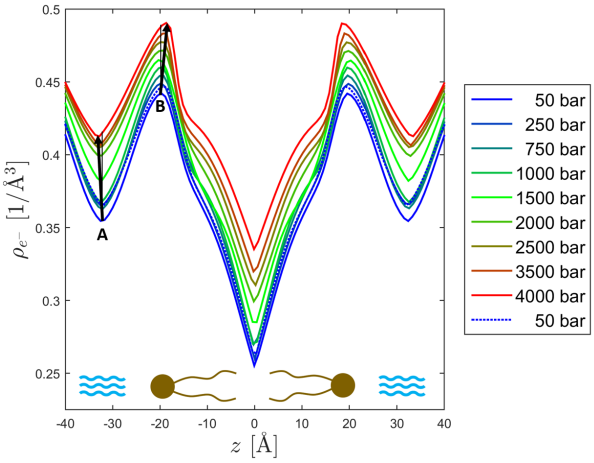

Figure 6.9: Electron density profiles of one repetition unit of DMPC multilayers containing 18.4 wt% cholesterol corresponding to the fits shown in figure 6.5. The *black arrows* highlight the slight shifts of the minima and maxima at increasing pressures. Adapted with permission from [153]. Copyright © 2019 Elsevier B.V.

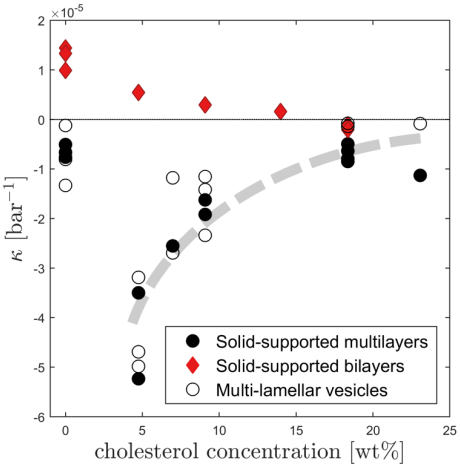

Figure 6.10: Comparison of compressibilities of different types of model membranes. The dashed line illustrates the course of the data points. Reprinted with permission from [153]. Copyright © 2019 Elsevier B.V.

most pronounced in the hydrophobic area. Moreover, the profiles show that the slight expansion of the multilayer with increasing pressures is due to an enlargement of the water-filled region between adjacent bilayers. This is illustrated by the *black arrows* in figure 6.9. The shift of the maxima **B** of the headgroup region towards the center of the bilayer indicates that the lipid layer itself is slightly compressed. The minima **A** in the water layer, however, move outwards so that an effective vertical expansion of the multilayer results.

The XRR measurements on multilayer samples where a detachment of bilayers occurred show that the bottom layer in direct contact to the substrate was highly stable and remained attached to the solid support. This is evident from the fact that in all cases still long oscillations are observed in the reflectivity curve, which indicate the presence of a $\backsim 50$ Å thick layer on the surface (see figure 6.5). For these samples, the thickness of the remaining single solid-supported bilayers was determined as $d = 8\pi/q_4$ from the position of the fourth oscillation maximum q_4, which was obtained by fitting a Gaussian distribution.

While vesicles and multilayers shared many characteristics, single bilayers behaved very differently upon pressurization (figure 6.8, *open markers*). Pure DMPC bilayers with direct contact to the solid support exhibited a slight vertical compression upon pressurization (*black symbols*). The incorporation of cholesterol made the membranes almost unresponsive to pressure and the bilayer thickness barely changed over the whole pressure range at all concentrations. These observations indicate that pressure-induced changes of the membrane structure are mostly suppressed in substrate-bound bilayers.

The reason why the bilayer thickness is always 15-20 Å smaller than the spacing of the multilayers is that the multilayer spacing comprises the thickness of a lipid bilayer and the thickness of the water layer between two bilayers. In addition, direct binding to a substrate compresses phospholipid bilayers by a few Ångströms [319].

To conduct a quantitative comparison of the pressure-response of all three types of model membranes that were considered in this study, their linear compressibility

$$\kappa = -\frac{1}{d_0}\frac{\Delta d}{\Delta p} \tag{6.1}$$

was determined. For this purpose, a linear model was fitted to the spacing or bilayer thickness d as a function of pressure p. The linear regions that were taken into account are indicated in figures 6.4 and 6.8. The solid-supported membranes showed a linear pressure-dependence in the whole pressure range in which they were stable. In the corresponding pressures ranges, multi-lamellar vesicles with the same cholesterol content also exhibited a linear behavior. However, the linearity did not extend over the entire measured pressure range. Therefore, only the linear increase in the low-pressure regime was taken into account for vesicle with low cholesterol content. Due to the phase transition that occurred in the low pressure regime at 14 wt% cholesterol, this concentration is not considered here. The resulting compressibilities of multi-lamellar vesicles, solid-supported multilayers, and solid-supported bilayers are presented in figure 6.10. The compressibility of unbound DMPC bilayers in vesicles assumed large negative values at low concentrations and approached zero when more cholesterol was added. In contrast, the compressibility of bilayers in direct contact to the substrate was almost zero independent of their cholesterol content. However, the cholesterol-dependence of the compressibility of solid-supported multilayers was similar to that of vesicles. It can be concluded that the influence of the substrate on the pressure-response of lipid bilayers is widely suppressed in a stack of 10-15 bilayers.

6.6 Conclusion

In this chapter, the pressure-dependent behavior of different types of DMPC model membranes containing varying amounts of cholesterol was examined. Multi-lamellar vesicles with low cholesterol contents exhibited a strong expansion of the spacing upon pressurization accompanied by a reduction of the long-range order perpendicular to the surface of the lamellae. At 14 wt% cholesterol, a phase transition from the $P_{\beta'}$ into the L_o was observed at 0.75 kbar. The structure of vesicles in the liquid ordered phase barely changed with increasing pressure as the position and width of the observed Bragg reflections were highly constant throughout the entire pressure range.

It was found that the behavior of solid-supported multilayers resemble that of multi-lamellar vesicles. However, the strong pressure-response upon the incorporation of low amounts of cholesterol reduced their stability. The similarity regarding spacing and compressibility between solid-supported multilayers and unbound bilayers in vesicles demonstrates that the deposition of 10-15 bilayers is sufficient to effectively reduce the

influence of the substrate. In contrast, the investigation of single bilayers revealed how strongly the solid support affects membranes in close proximity. Their pressure-response was small and almost independent of the cholesterol content due to the strong substrate-lipid interaction that confines the vertical flexibility [147, 320].

The presented study shows that cholesterol can improve the stability of solid-supported multilayers and can reduce their tendency to detach even under pressurization stress. This opens the way to the application of solid-supported multilayers for a variety of experiments that are based on surface-sensitive methods and require stable model membranes under full hydration, e.g, on the interaction of membranes with proteins at high pressure conditions.

Chapter 7

Conclusion and outlook

In this thesis, X-ray scattering methods were used to investigate how fusogenic peptides, cellular solutes and cholesterol affect the structure of lipid membranes. In a pressure-jump study on monoolein model membranes, the influence of different osmolytes, molecular crowding and fusogenic peptides of viral envelope proteins on the equilibration of cubic lipid structures was examined. Moreover, the adsorption and insertion behavior of the fusogenic peptides was investigated at phospholipid Langmuir monolayers. In a further study, the effect of cholesterol on the pressure-response of DMPC membranes was explored and the behavior of solid-supported model systems at high hydrostatic pressures was compared to vesicles.

In the first project, the effects of additives on pressure-induced remodeling processes of monoolein structures in excess water were examined with SAXS. After a pressure-jump across the lamellar-to-cubic phase boundary, the cubic phase formed with an increased lattice constant and released excess water until equilibrium was reached within a few hours. Urea strongly decelerated the reduction of the lattice constant, so that it took, three times longer until a threshold of 110 % of the equilibrium value was reached. Thus, the affinity of urea to interact with the surface of lipid structures, which promotes states with large headgroup areas [30, 71], does not only shift the equilibrium curvature of lipid structures, but also reduces the speed of dynamic processes that involve an increase of negative curvature. In presence of TMAO and sucrose, 110 % of the equilibrium lattice constants were in most cases reached after less than half an hour. The strong interactions of these molecules with water cause a displacement from lipid structures [26]. The fast release of excess water from the monoolein phase can be explained by the resulting osmotic pressure between the interior of the cubic structure and the surrounding water. Although cellular membrane processes typically do not involve the formation of channel systems like they are found in bicontinuous cubic phases, the approaching of two membranes prior to a fusion process still forms a confined water layer where it is unfavorable for molecules like TMAO and sucrose to reside. The results presented in this thesis show that TMAO and sucrose can accelerate the dehydration of such confined spaces, which is essential for a fusion event. For urea and TMAO in a 2:1 ratio, a compensation of the effects of both molecules on the equilibration process was found.

Similar to TMAO and sucrose, PEG reduced the lattice constant of cubic monoolein structures and accelerated the dynamics after a pressure-jump. Both effects increased with the size of the polymers, although it is known that the osmotic pressure exerted by PEG decreases with the molecular weight at constant mass concentration [266]. As the radius of the water channels of monoolein structures is in the same order of magnitude as the radii of gyration of the examined PEGs, this can be explained by an increasing concentration gradient between hydration and excess water. The larger the polymers are, the more unfavorable is the confinement by the channel system. For PEG with a radius of gyration that is larger than the radius of the monoolein water channels ($M \geq 4000\,\mathrm{g/mol}$), a transition into the Ia3d phase was induced. As a further increase of the polymer size did not lead to a further compression of the lipid structures, it is assumed that PEG was fully displaced from the cubic structure in the whole Ia3d regime.

The interaction of membranes with viral peptide sequences was examined with two different approaches. The results of the first and second project provide a consistent view on the interaction of fusogenic peptides with lipid membranes, and existing assumptions concerning interaction modes and penetration depths were experimentally confirmed in this thesis. In the second project, the effect of fusogenic peptides on the structure of phospholipid monolayers was investigated with XRR and GID. It was found that HA2-FP has a high affinity for the hydrophobic air-water interface and it accumulated at the surface in presence and absence of lipids until a surface pressure of approximately 30 mN/m was reached. HA2-FP was able to penetrate even highly compressed DPPA films at 35 mN/m. For DPPC, an insertion of peptides into the lipid layer was only found below 30 mN/m. In DPPA films, HA2-FP accumulated at the polar-apolar interface while it was found in the hydrophobic region of DPPC monolayers. The deep insertion into DPPC membranes can be explained by the ability of the large headgroups to wrap around incorporated peptides, which promotes a mixing of lipids and peptides. The experimental results suggest that the small headgroups of DPPA rather cause the formation of HA2-FP clusters. However, both insertion modes indicate that HA2-FP is able to induce negative curvature in lipid membranes.

An interaction with the FLs of TBEV and VSV was only observed with DPPA and not with DPPC films. They attached underneath the headgroups forming defined layers. TBEV-FL showed also slight effects on the hydrophobic region indicating a maximum insertion depth of approximately 7 Å at 15 mN/m that decreased to approximately 4 Å at 35 mN/m. At 25 mN/m, VSV-FL showed a similar behavior with an insertion depth of approximately 5 Å. At 35 mN/m, a pronounced accumulation layer underneath the surface was still observed, but the hydrophobic region was not affected at all. In contrast, VSV-FL had a strong effect on the whole layer profile at 15 mN/m. Presumably, the peptides filled void spaces of the monolayer and displaced crystalline lipid structures. The observed behavior of TBEV-FL and VSV-FL confirms the assumption that the peptides interact mainly with the surface of membranes and only penetrate them via aromatic anchors [125, 205]. The TMD of VSV did not attach to DPPA monolayers despite the electrostatic attraction. At 15 mN/m, it inserted deep into the hydrophobic region, while it was not able to penetrate the monolayer at 35 mN/m.

In good agreement with the results of the Langmuir monolayer study, the peptides

showed different effects on the behavior of monoolein upon pressure-jumps. Similar to urea, the preferred interaction of TBEV-FL and VSV-FL with the surface of membranes caused an increase of the equilibrium lattice constant of the Pn3m phase and a deceleration of the release of excess water after a pressure-jump. HA2-FP, VSV-TMD and L16 strongly accelerated the equilibration process. In contrast to TMAO, sucrose and PEG, the three peptides did not dehydrate the cubic phase at equilibrium, so that the effect of the peptides cannot be explained by depletion. Instead, it is assumed that the sequences modulate the structure and dynamics of monoolein by penetrating the lipid layers. For HA2-FP and VSV-TMD, the assumption is supported by the results of the second project. The ability of the peptides to insert into phospholipid monolayers at the air-water interface, however, reduced at high surface pressures. This is in agreement with the observation that the peptides are displaced from monoolein structures in the L_c phase at 1000 bar. Presumably, the acceleration of the reduction of the lattice parameter after a pressure-jump is primarily due to an increase of the area of the Pn3m surface that is induced by a reinsertion of the peptides.

Pressure-jumps in the opposite direction from 50 bar to 1500 bar revealed that the presence of TBEV-FL induces a fast transition into the L_c phase. This confirms that the peptide promotes structures with large headgroup areas and thus low negative curvature due to a preferential interaction with the surface of membranes. Surprisingly, HA2-FP induced a fast formation of a highly swollen Pn3m phase with a lattice constant of approximately 150 Å that was stable for at least 16 hours. For a deeper understanding of this observation, pressure-jumps from the cubic into the lamellar regime in presence of VSV-TMD and L16 will be performed in future experiments. The results will reveal if the observed stability of the swollen Pn3m phase at 1500 bar is induced by the unique structural properties of HA2-FP, which is thought to induce negative Gaussian curvature in membranes [51, 198], or if comparable effects can also be induced by other hydrophobic peptides. Moreover, further additives like urea and TMAO should be included into the study. Exploring how the interaction of urea with monoolein headgroups affects the behavior of metastable Pn3m structures in contrast to TBEV-FL might help to asses the role of the aromatic anchors of TBEV-FL for causing the fast cubic-to-lamellar transition. Experiments with TMAO or PEG would shed light on the influence of depletion on the cubic-to-lamellar transition.

In the third project, it was explored how cholesterol modulates the pressure-response of DMPC membranes. It was found that the spacing of multi-lamellar DMPC structures that contain low amounts of cholesterol expands strongly upon pressurization. Above a cholesterol content of 14 wt%, DMPC membranes entered the L_o phase and their structure barely changed when hydrostatic pressures were applied. Spacing and compressibility of solid-supported multilayers were very similar to multi-lamellar vesicles, indicating that the preparation of 10-15 bilayers is sufficient to suppress the influence of the substrate. Single bilayers in direct contact to the substrate showed a very different behavior, as their compressibility was almost zero at all cholesterol concentrations.

It was shown that the addition of cholesterol can improve the stability of DMPC multilayers, as their tendency to detach from the substrate reduced in the liquid ordered phase. In the corresponding concentration regime, it was possible to obtain detailed

electron density profiles of the vertical structure of the bilayers with XRR. On the basis of these results, new approaches can be designed to study, e.g., the interaction of lipid membranes with proteins or deep-sea osmolytes at high pressure conditions taking advantage of the potential of surface-sensitive methods.

Appendix A

Supplementary information

A.1 SAXS data and fits of the pressure-jump experiments

In this section, integrated SAXS patterns and the obtained fits of the pressure-jump study discussed in chapter 4 are presented. Figures A.1 to A.10 show data of monoolein samples with a water content of 80 and 90 wt% in absence of additives and monolein samples containing urea, TMAO, PEG 400, PEG 1500, PEG 4000, PEG 35000, HA2-FP and TBEV-FL.

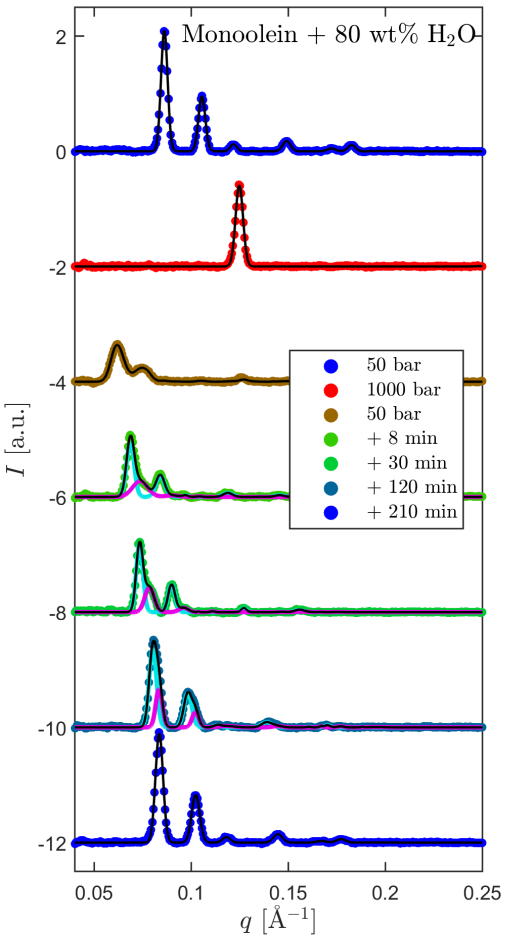

Figure A.1: SAXS data (*colored points*) and fits (*black lines*) of monoolein samples with a water content of 80 wt% at 50 bar before pressurization (*top*), at 1000 bar immediately before and at 50 bar immediately and at different times after the pressure-jump. At 50 bar the cubic Pn3m phase occurred and at 1000 bar the lamellar L_c phase. When domains with different Pn3m lattice constants were observed, the separate contributions are illustrated in *teal* and *pink*.

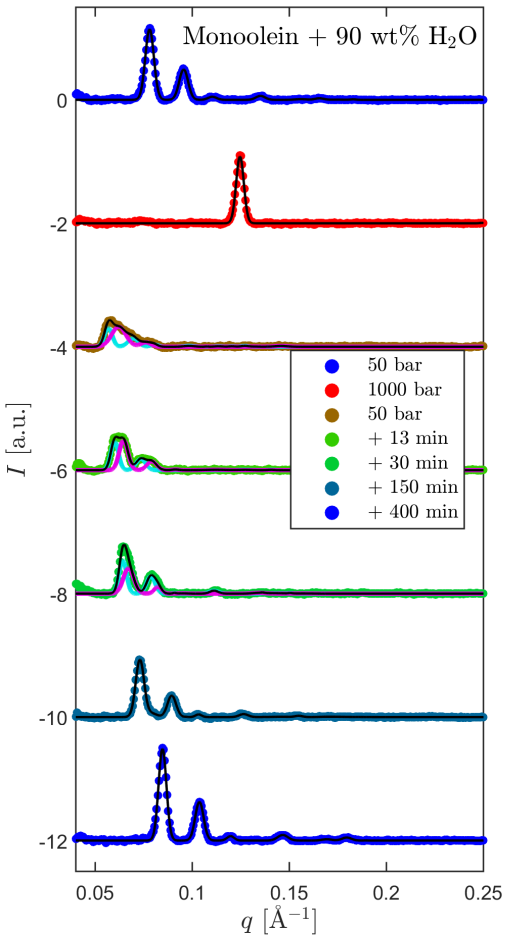

Figure A.2: SAXS data (*colored points*) and fits (*black lines*) of monoolein samples with a water content of 90 wt% at 50 bar before pressurization (*top*), at 1000 bar immediately before and at 50 bar immediately and at different times after the pressure-jump. At 50 bar the cubic Pn3m phase occurred and at 1000 bar the lamellar L_c phase. When domains with different Pn3m lattice constants were observed, the separate contributions are illustrated in *teal* and *pink*.

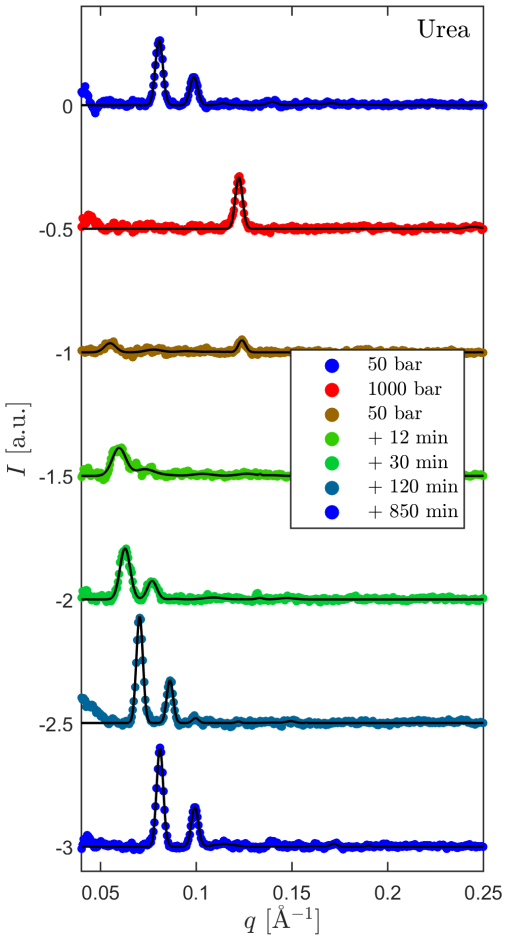

Figure A.3: SAXS data (*colored points*) and fits (*black lines*) of monoolein samples containing 1 M urea at 50 bar before pressurization (*top*), at 1000 bar immediately before and at 50 bar immediately and at different times after the pressure-jump. At 50 bar the cubic Pn3m phase occurred and at 1000 bar the lamellar L_c phase.

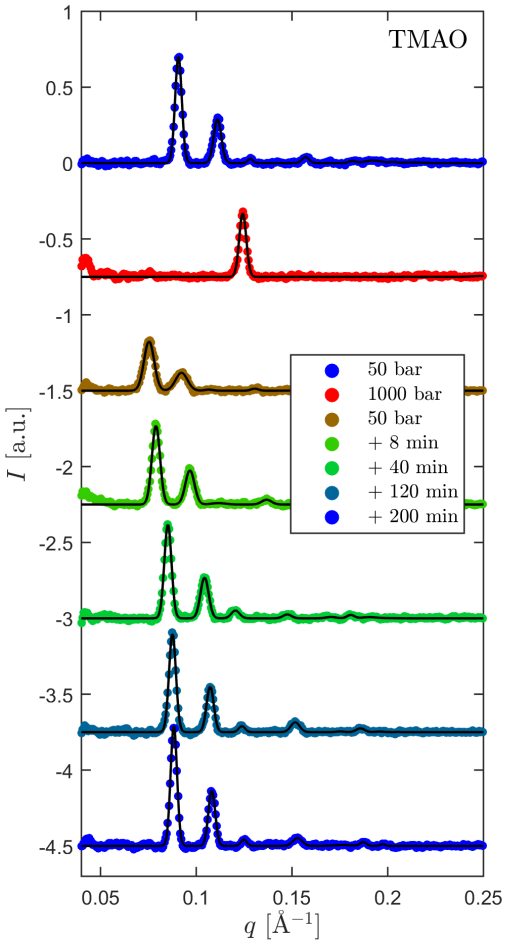

Figure A.4: SAXS data (*colored points*) and fits (*black lines*) of monoolein samples containing 1 M TMAO at 50 bar before pressurization (*top*), at 1000 bar immediately before and at 50 bar immediately and at different times after the pressure-jump. At 50 bar the cubic Pn3m phase occurred and at 1000 bar the lamellar L_c phase.

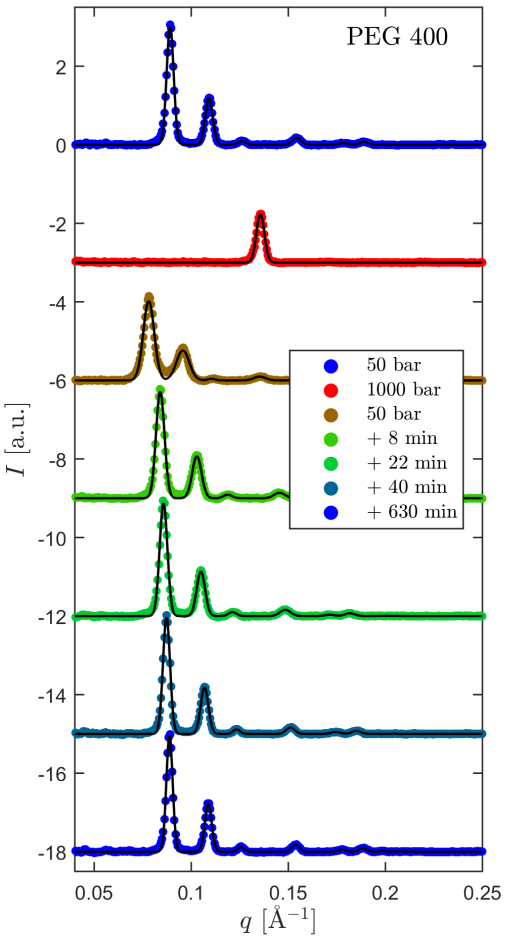

Figure A.5: SAXS data (*colored points*) and fits (*black lines*) of monoolein samples containing 150 g/L PEG 400 at 50 bar before pressurization (*top*), at 1000 bar immediately before and at 50 bar immediately and at different times after the pressure-jump. At 50 bar the cubic Pn3m phase occurred and at 1000 bar the lamellar L_c phase.

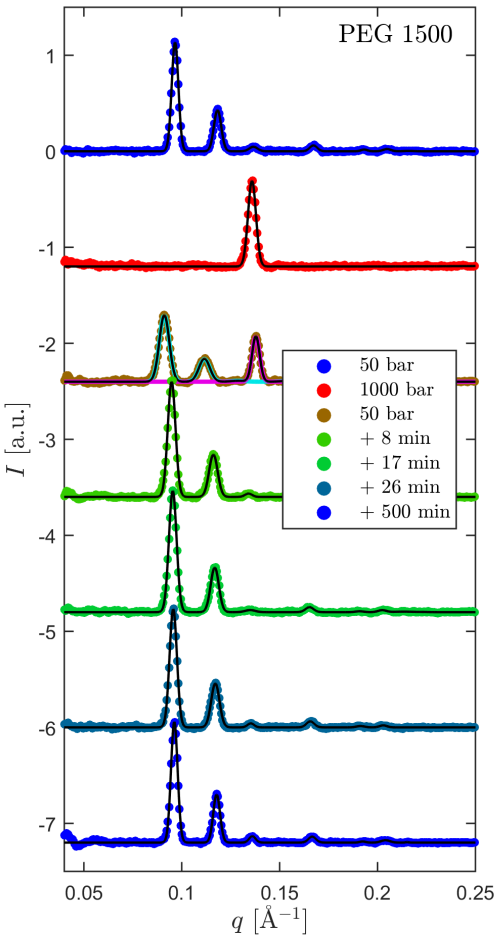

Figure A.6: SAXS data (*colored points*) and fits (*black lines*) of monoolein samples containing 150 g/L PEG 1500 at 50 bar before pressurization (*top*), at 1000 bar immediately before and at 50 bar immediately and at different times after the pressure-jump. At 50 bar the cubic Pn3m phase occurred and at 1000 bar the lamellar L_c phase. Immediately after the pressure-jump both phases coexisted. The separate contributions are illustrated in *teal* (Pn3m) and *pink* (L_c).

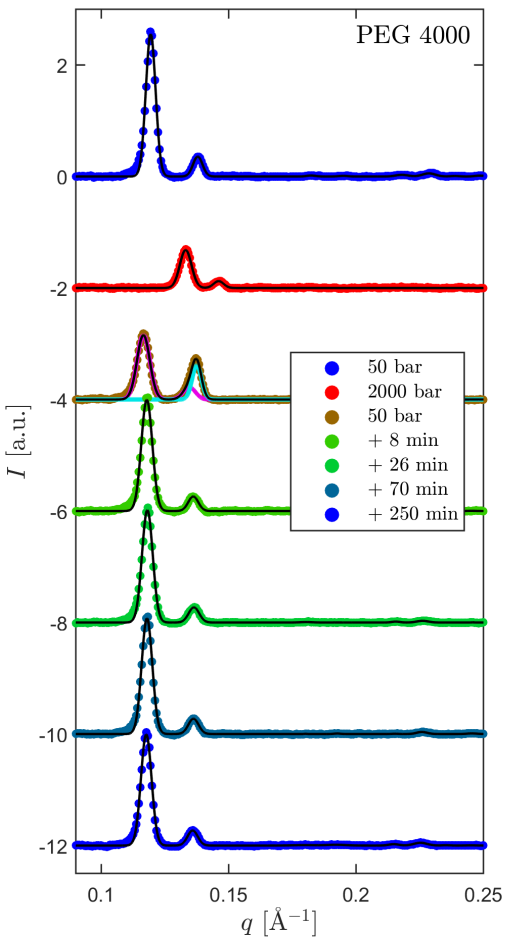

Figure A.7: SAXS data (*colored points*) and fits (*black lines*) of monoolein samples containing 150 g/L PEG 4000 at 50 bar before pressurization (*top*), at 2000 bar immediately before and at 50 bar immediately and at different times after the pressure-jump. At 50 bar the cubic Ia3d phase occurred and at 2000 bar the lamellar L_c and L_m phase. Immediately after the pressure-jump Ia3d and L_c phase coexisted. The separate contributions are illustrated in *teal* (Ia3d) and *pink* (L_c).

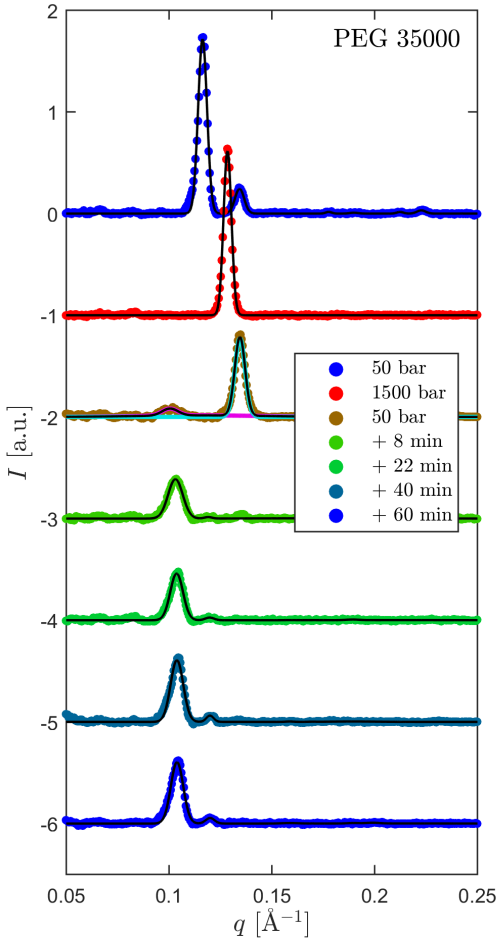

Figure A.8: SAXS data (*colored points*) and fits (*black lines*) of monoolein samples containing 150 g/L PEG 35000 at 50 bar before pressurization (*top*), at 1500 bar immediately before and at 50 bar immediately and at different times after the pressure-jump. At 50 bar the cubic Ia3d phase occurred and at 1500 bar the lamellar L_c phase. Immediately after the pressure-jump both phases coexisted. The separate contributions are illustrated in *teal* (Ia3d) and *pink* (L_c).

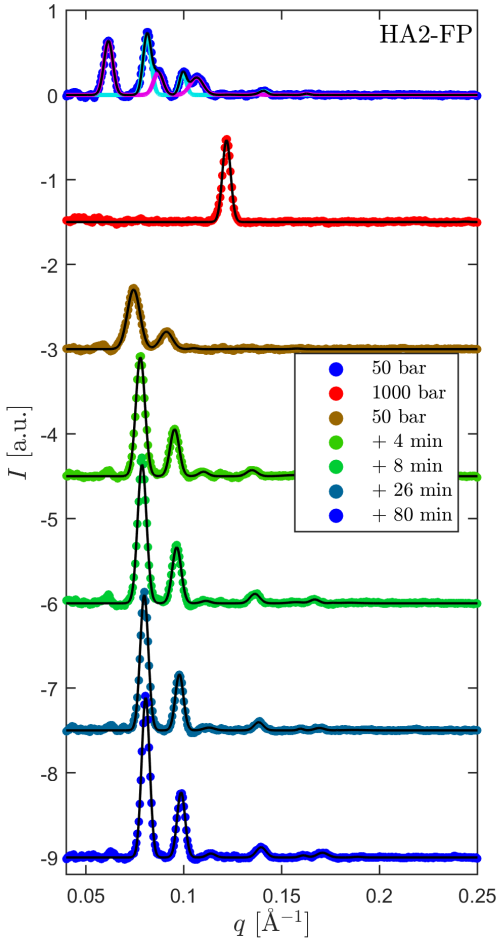

Figure A.9: SAXS data (*colored points*) and fits (*black lines*) of monoolein samples containing 2 wt% HA2-FP at 50 bar before pressurization (*top*), at 1000 bar immediately before and at 50 bar immediately and at different times after the pressure-jump. At 50 bar the cubic Pn3m phase occurred and at 1000 bar the lamellar L_c phase. Before pressurization Pn3m and Im3m phase coexisted. The separate contributions are illustrated in *teal* (Pn3m) and *pink* (Im3m).

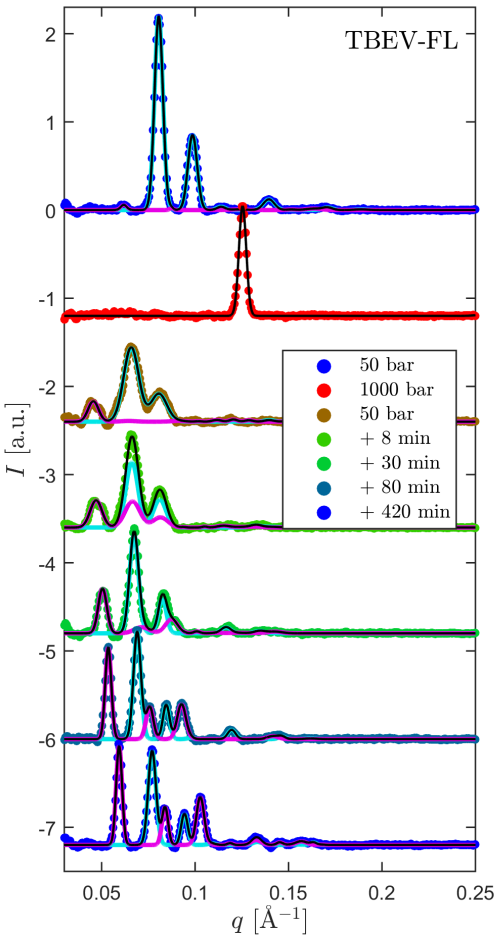

Figure A.10: SAXS data (*colored points*) and fits (*black lines*) of monoolein samples containing 2 wt% TBEV-FL at 50 bar before pressurization (*top*), at 1000 bar immediately before and at 50 bar immediately and at different times after the pressure-jump. At 50 bar the cubic Pn3m and Im3m phases occurred. The separate contributions are illustrated in *teal* (Pn3m) and *pink* (Im3m). At 1000 bar the lamellar L_c phase was observed.

A.2 The interaction of TBEV-FL, VSV-FL and VSV-TMD with DPPC Langmuir films

The injection of TBEV-FL, VSV-FL and VSV-TMD into the subphase barely affected the structure of DPPC Langmuir films at constant surface area. The surface pressure remained unchanged in all cases. Figure A.11 to A.16 show the results of XRR and GID scans conducted 40 minutes after the injection. The lattice constants typically changed by less than 0.1 %. Modifications of the electron density profiles were only observed at 5 mN/m. However, these are possibly due to the instability of low-compressed DPPC films and cannot be clearly assigned to an interaction with the peptides. In conclusion, these data do not provide evidence of a distinct influence of the peptides on the structure of DPPC monolayers at the corresponding time scale.

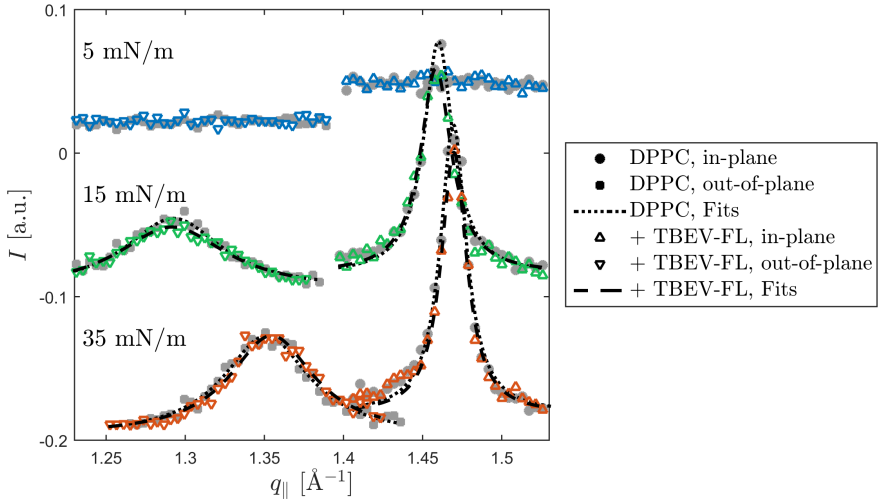

Figure A.11: GID reflections of DPPC films before (*gray symbols*) and after (*colored symbols*) the injection of TBEV-FL as a function of $q_\parallel$ and fits (*black*).

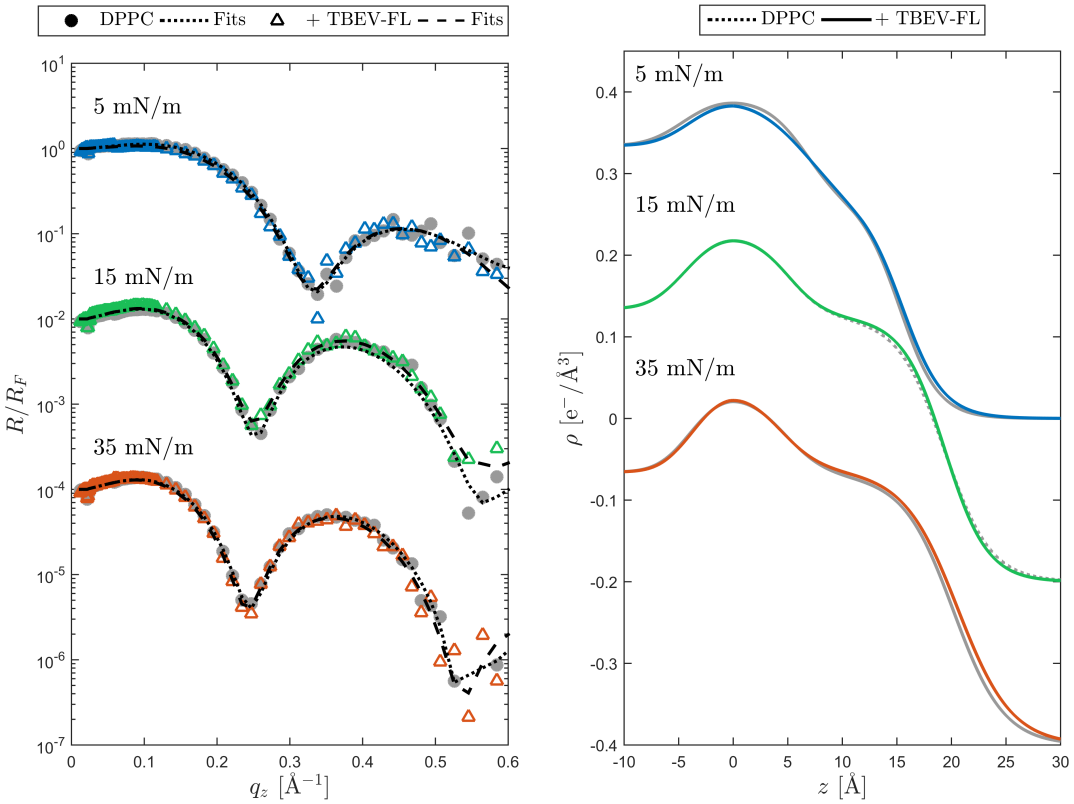

Figure A.12: XRR data (*left*) and electron density profiles (*right*) of DPPC films before (*gray*) and after (*colored*) the addition of TBEV-FL and fits (*black*). Reflectivity curves and electron density profiles are shifted vertically for better visualization.

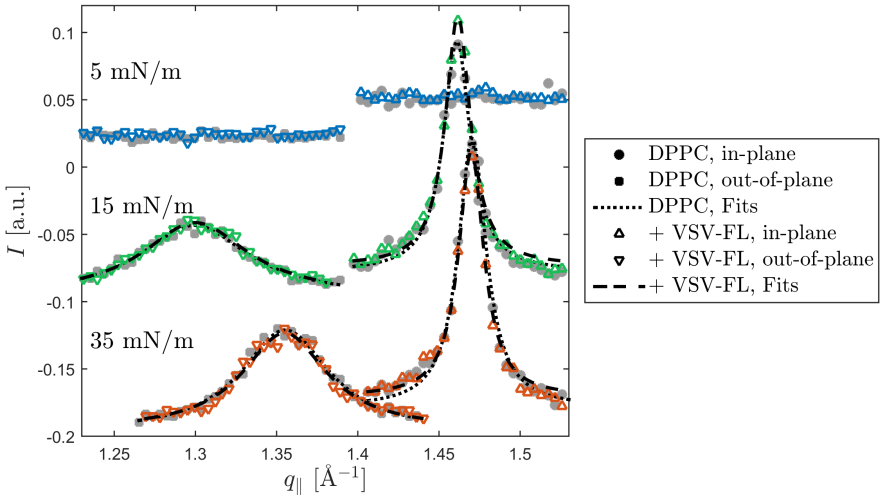

Figure A.13: GID reflections of DPPC films before (*gray symbols*) and after (*colored symbols*) the injection of VSV-FL as a function of $q_{\parallel}$ and fits (*black*).

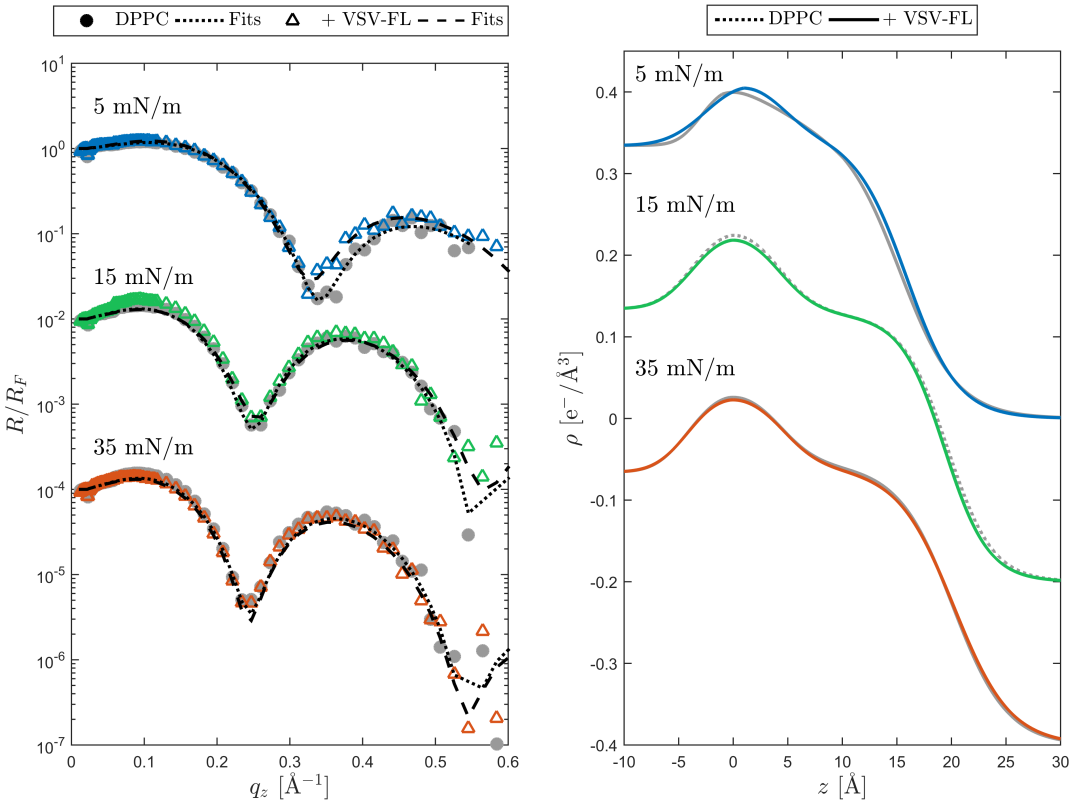

Figure A.14: XRR data (*left*) and electron density profiles (*right*) of DPPC films before (*gray*) and after (*colored*) the addition of VSV-FL and fits (*black*). Reflectivity curves and electron density profiles are shifted vertically for better visualization.

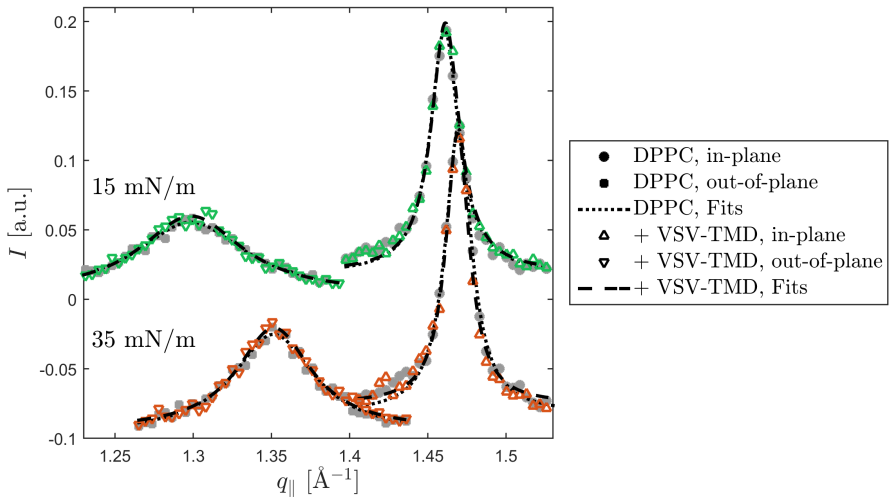

Figure A.15: GID reflections of DPPC films before (*gray symbols*) and after (*colored symbols*) the injection of VSV-TMD as a function of $q_{\|}$ and fits (*black*).

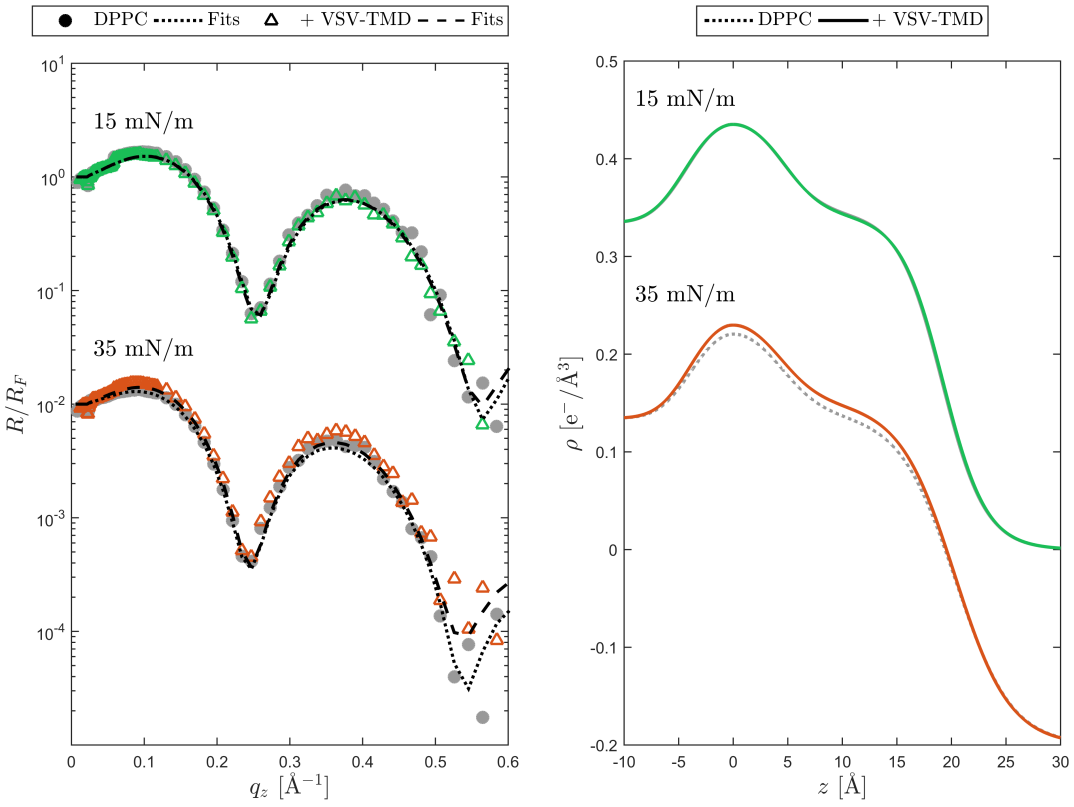

Figure A.16: XRR data (*left*) and electron density profiles (*right*) of DPPC films before (*gray*) and after (*colored*) the addition of VSV-TMD and fits (*black*). Reflectivity curves and electron density profiles are shifted vertically for better visualization.

List of Figures

List of Tables

Bibliography

[1] Charles Tanford, "The hydrophobic effect and the organization of living matter", in: *Science* 200.4345 (1978), pp. 1012–1018.

[2] Pieter R Cullis, Michael J Hope, and Colin PS Tilcock, "Lipid polymorphism and the roles of lipids in membranes", in: *Chemistry and physics of lipids* 40.2-4 (1986), pp. 127–144.

[3] Vadim A Frolov, Anna V Shnyrova, and Joshua Zimmerberg, "Lipid polymorphisms and membrane shape", in: *Cold Spring Harbor perspectives in biology* 3.11 (2011), a004747.

[4] Mónica Fernández-Vidal, Stephen H White, and Alexey S Ladokhin, "Membrane partitioning:"classical" and "nonclassical" hydrophobic effects", in: *The Journal of membrane biology* 239.1-2 (2011), pp. 5–14.

[5] S Jonathan Singer and Garth L Nicolson, "The fluid mosaic model of the structure of cell membranes", in: *Science* 175.4023 (1972), pp. 720–731.

[6] Sean D Conner and Sandra L Schmid, "Regulated portals of entry into the cell", in: *Nature* 422.6927 (2003), pp. 37–44.

[7] Yoko Shibata et al., "Mechanisms shaping the membranes of cellular organelles", in: *Annual Review of Cell and Developmental* 25 (2009), pp. 329–354.

[8] Tom Misteli, "The concept of self-organization in cellular architecture", in: *J Cell Biol* 155.2 (2001), pp. 181–186.

[9] John F Nagle, "Theory of the main lipid bilayer phase transition", in: *Annual Review of Physical Chemistry* 31.1 (1980), pp. 157–196.

[10] John F Nagle and Stephanie Tristram-Nagle, "Structure of lipid bilayers", in: *Biochimica et Biophysica Acta (BBA)-Reviews on Biomembranes* 1469.3 (2000), pp. 159–195.

[11] Roland Winter and Christoph Jeworrek, "Effect of pressure on membranes", in: *Soft Matter* 5.17 (2009), pp. 3157–3173.

[12] Philippe M Oger and Mohamed Jebbar, "The many ways of coping with pressure", in: *Research in microbiology* 161.10 (2010), pp. 799–809.

[13] R Winter and W Dzwolak, "Exploring the temperature–pressure configurational landscape of biomolecules: from lipid membranes to proteins", in: *Philosophical Transactions of the Royal Society A: Mathematical, Physical and Engineering Sciences* 363.1827 (2005), pp. 537–563.

[14] George N Somero, "Adaptations to high hydrostatic pressure", in: *Annual review of physiology* 54.1 (1992), pp. 557–577.

[15] Sergey A Kotenkov et al., "Effect of Cholesterol and Curcumin on Ordering of DMPC Bilayers", in: *Applied Magnetic Resonance* 50.1-3 (2019), pp. 511–520.

[16] Yuichi Harano, Takashi Yoshidome, and Masahiro Kinoshita, "Molecular mechanism of pressure denaturation of proteins", in: *The Journal of chemical physics* 129.14 (2008), 10B607.

[17] Paul H Yancey, "Organic osmolytes as compatible, metabolic and counteracting cytoprotectants in high osmolarity and other stresses", in: *Journal of Experimental Biology* 208.15 (2005), pp. 2819–2830.

[18] Paul H Yancey et al., "Trimethylamine oxide counteracts effects of hydrostatic pressure on proteins of deep-sea teleosts", in: *Journal of Experimental Zoology* 289.3 (2001), pp. 172–176.

[19] Karin Julius et al., "Water-mediated protein-protein interactions at high pressures are controlled by a deep-sea osmolyte", in: *Physical review letters* 121.3 (2018), p. 038101.

[20] Robert H Kelly and Paul H Yancey, "High contents of trimethylamine oxide correlating with depth in deep-sea teleost fishes, skates, and decapod crustaceans", in: *The Biological Bulletin* 196.1 (1999), pp. 18–25.

[21] PH Yancey et al., "Trimethylamine oxide, betaine and other osmolytes in deep-sea animals: depth trends and effects on enzymes under hydrostatic pressure", in: *Cellular and molecular biology* 50.4 (2004), pp. 371–376.

[22] Martin A Schroer et al., "Exploring the piezophilic behavior of natural cosolvent mixtures", in: *Angewandte Chemie International Edition* 50.48 (2011), pp. 11413–11416.

[23] Mimi Gao et al., "Crowders and cosolvents—major contributors to the cellular milieu and efficient means to counteract environmental stresses", in: *ChemPhysChem* 18.21 (2017), pp. 2951–2972.

[24] Qin Zou et al., "The molecular mechanism of stabilization of proteins by TMAO and its ability to counteract the effects of urea", in: *Journal of the American Chemical Society* 124.7 (2002), pp. 1192–1202.

[25] Vladimir Voloshin et al., "Dynamics of TMAO and urea in the hydration shell of the protein SNase", in: *Physical Chemistry Chemical Physics* 21.35 (2019), pp. 19469–19479.

[26] Shahar Sukenik et al., "TMAO mediates effective attraction between lipid membranes by partitioning unevenly between bulk and lipid domains", in: *Physical Chemistry Chemical Physics* 19.44 (2017), pp. 29862–29871.

[27] Magiliny Manisegaran et al., "Effects of the deep-sea osmolyte TMAO on the temperature and pressure dependent structure and phase behavior of lipid membranes", in: *Physical Chemistry Chemical Physics* 21.34 (2019), pp. 18533–18540.

[28] Agnieszka Nowacka et al., "Small polar molecules like glycerol and urea can preserve the fluidity of lipid bilayers under dry conditions", in: *Soft Matter* 8.5 (2012), pp. 1482–1491.

[29] J Valerio, S Bernstorff, and SS Funari, "Effect of urea and tmao on lipid bilayers", in: *European Pharmaceutical Journal* 64.2 (2017), pp. 24–27.

[30] Quoc Dat Pham et al., "Effects of Urea and TMAO on Lipid Self-Assembly under Osmotic Stress Conditions", in: *The Journal of Physical Chemistry B* 122.25 (2018), pp. 6471–6482.

[31] Kimby N Barton, Mary M Buhr, and James S Ballantyne, "Effects of urea and trimethylamine N-oxide on fluidity of liposomes and membranes of an elasmobranch", in: *American Journal of Physiology-Regulatory, Integrative and Comparative Physiology* 276.2 (1999), R397–R406.

[32] Jahur A Mondal, "Effect of trimethylamine N-oxide on interfacial electrostatics at phospholipid monolayer–water interfaces and its relevance to cardiovascular disease", in: *The journal of physical chemistry letters* 7.9 (2016), pp. 1704–1708.

[33] Judith M White and Gary R Whittaker, "Fusion of enveloped viruses in endosomes", in: *Traffic* 17.6 (2016), pp. 593–614.

[34] Stephen C Harrison, "Viral membrane fusion", in: *Virology* 479 (2015), pp. 498–507.

[35] Stephen C Harrison, "Viral membrane fusion", in: *Nature structural & molecular biology* 15.7 (2008), pp. 690–698.

[36] Reinhard Jahn, Thorsten Lang, and Thomas C Südhof, "Membrane fusion", in: *Cell* 112.4 (2003), pp. 519–533.

[37] Sander Boonstra et al., "Hemagglutinin-mediated membrane fusion: A biophysical perspective", in: *Annual review of biophysics* 47 (2018), pp. 153–173.

[38] Yorgo Modis, "Relating structure to evolution in class II viral membrane fusion proteins", in: *Current opinion in virology* 5 (2014), pp. 34–41.

[39] Eduard Baquero, Aurélie AV Albertini, and Yves Gaudin, "Recent mechanistic and structural insights on class III viral fusion glycoproteins", in: *Current opinion in structural biology* 33 (2015), pp. 52–60.

[40] Margaret Kielian, "Class II virus membrane fusion proteins", in: *Virology* 344.1 (2006), pp. 38–47.

[41] José L Nieva and Aitziber Agirre, "Are fusion peptides a good model to study viral cell fusion?", in: *Biochimica et Biophysica Acta (BBA)-Biomembranes* 1614.1 (2003), pp. 104–115.

[42] Richard M Epand, "Fusion peptides and the mechanism of viral fusion", in: *Biochimica et Biophysica Acta (BBA)-Biomembranes* 1614.1 (2003), pp. 116–121.

[43] Andrey Ivankin, Ivan Kuzmenko, and David Gidalevitz, "Cholesterol mediates membrane curvature during fusion events", in: *Physical review letters* 108.23 (2012), p. 238103.

[44] Yali Ci et al., "Vesicular stomatitis virus G protein transmembrane region is crucial for the hemi-fusion to full fusion transition", in: *Scientific reports* 8.1 (2018), pp. 1–11.

[45] Liang Shang, Ling Yue, and Eric Hunter, "Role of the membrane-spanning domain of human immunodeficiency virus type 1 envelope glycoprotein in cell-cell fusion and virus infection", in: *Journal of virology* 82.11 (2008), pp. 5417–5428.

[46] R Todd Armstrong, Anna S Kushnir, and Judith M White, "The transmembrane domain of influenza hemagglutinin exhibits a stringent length requirement to support the hemifusion to fusion transition", in: *The Journal of cell biology* 151.2 (2000), pp. 425–438.

[47] Britta Schroth-Diez et al., "The role of the transmembrane and of the intraviral domain of glycoproteins in membrane fusion of enveloped viruses", in: *Bioscience reports* 20.6 (2000), pp. 571–595.

[48] Jinwoo Lee et al., "Structure of the Ebola virus envelope protein MPER/TM domain and its interaction with the fusion loop explains their fusion activity", in: *Proceedings of the National Academy of Sciences* 114.38 (2017), E7987–E7996.

[49] Ding-Kwo Chang et al., "Membrane interaction and structure of the transmembrane domain of influenza hemagglutinin and its fusion peptide complex", in: *BMC biology* 6.1 (2008), p. 2.

[50] Tanusree Sengupta, Hirak Chakraborty, and Barry R Lentz, "The transmembrane domain peptide of vesicular stomatitis virus promotes both intermediate and pore formation during PEG-mediated vesicle fusion", in: *Biophysical journal* 107.6 (2014), pp. 1318–1326.

[51] Artem Levin et al., "Lipid Phase Control and Secondary Structure of Viral Fusion Peptides Anchored in Monoolein Membranes", in: *The Journal of Physical Chemistry B* 121.36 (2017), pp. 8492–8502.

[52] Sourav Haldar et al., "Lipid-dependence of target membrane stability during influenza viral fusion", in: *J Cell Sci* 132.4 (2019), jcs218321.

[53] Luis GM Basso et al., "SARS-CoV fusion peptides induce membrane surface ordering and curvature", in: *Scientific reports* 6 (2016), p. 37131.

[54] Sung-Tae Yang et al., "The role of cholesterol in membrane fusion", in: *Chemistry and physics of lipids* 199 (2016), pp. 136–143.

[55] Geetanjali Meher and Hirak Chakraborty, "Membrane composition modulates fusion by altering membrane properties and fusion peptide structure", in: *The Journal of membrane biology* 252.4-5 (2019), pp. 261–272.

[56] Adriana Ganem-Quintanar, David Quintanar-Guerrero, and Pierre Buri, "Monoolein: a review of the pharmaceutical applications", in: *Drug development and industrial pharmacy* 26.8 (2000), pp. 809–820.

[57] Jaymin C Shah, Yogesh Sadhale, and Dakshina Murthy Chilukuri, "Cubic phase gels as drug delivery systems", in: *Advanced drug delivery reviews* 47.2-3 (2001), pp. 229–250.

[58] Xavier Mulet, Ben J Boyd, and Calum J Drummond, "Advances in drug delivery and medical imaging using colloidal lyotropic liquid crystalline dispersions", in: *Journal of colloid and interface science* 393 (2013), pp. 1–20.

[59] Ewa Nazaruk et al., "Lyotropic cubic phases for drug delivery: diffusion and sustained release from the mesophase evaluated by electrochemical methods", in: *Langmuir* 31.46 (2015), pp. 12753–12761.

[60] Ivo Lopes et al., "Monoolein-based nanocarriers for enhanced folate receptor-mediated RNA delivery to cancer cells", in: *Journal of liposome research* 26.3 (2016), pp. 199–210.

[61] Cecília Leal et al., "Highly efficient gene silencing activity of siRNA embedded in a nanostructured gyroid cubic lipid matrix", in: *Journal of the American Chemical Society* 132.47 (2010), pp. 16841–16847.

[62] Hojun Kim and Cecilia Leal, "Cuboplexes: Topologically active siRNA delivery", in: *ACS nano* 9.10 (2015), pp. 10214–10226.

[63] Minjee Kang and Cecilia Leal, "Soft Nanostructured Films for Actuated Surface-Based siRNA Delivery", in: *Advanced Functional Materials* 26.31 (2016), pp. 5610–5620.

[64] Hojun Kim et al., "Microfluidics synthesis of gene silencing cubosomes", in: *ACS nano* 12.9 (2018), pp. 9196–9205.

[65] Abhishek Gupta et al., "Nanoassemblies of Gd–DTPA–monooleyl and glycerol monooleate amphiphiles as potential MRI contrast agents", in: *Journal of Materials Chemistry B* 2.9 (2014), pp. 1225–1233.

[66] Urszula Bazylińska et al., "Polymer-free cubosomes for simultaneous bioimaging and photodynamic action of photosensitizers in melanoma skin cancer cells", in: *Journal of colloid and interface science* 522 (2018), pp. 163–173.

[67] Alexandru Zabara et al., "Design of ultra-swollen lipidic mesophases for the crystallization of membrane proteins with large extracellular domains", in: *Nature communications* 9.1 (2018), pp. 1–9.

[68] C-Y Huang et al., "In meso in situ serial X-ray crystallography of soluble and membrane proteins", in: *Acta Crystallographica Section D: Biological Crystallography* 71.6 (2015), pp. 1238–1256.

[69] Vadim Cherezov, "Lipidic cubic phase technologies for membrane protein structural studies", in: *Current opinion in structural biology* 21.4 (2011), pp. 559–566.

[70] Vadim Cherezov et al., "Membrane protein crystallization in meso: lipid type-tailoring of the cubic phase", in: *Biophysical journal* 83.6 (2002), pp. 3393–3407.

[71] Vadim Cherezov et al., "Room to move: crystallizing membrane proteins in swollen lipidic mesophases", in: *Journal of molecular biology* 357.5 (2006), pp. 1605–1618.

[72] Valentina Grippo et al., "Cellobiose dehydrogenase hosted in lipidic cubic phase to improve catalytic activity and stability", in: *Bioelectrochemistry* 125 (2019), pp. 134–141.

[73] Wenjie Sun et al., "Lyotropic liquid crystalline cubic phases as versatile host matrices for membrane-bound enzymes", in: *The journal of physical chemistry letters* 7.8 (2016), pp. 1507–1512.

[74] Jijo J Vallooran et al., "Lipidic cubic phases as a versatile platform for the rapid detection of biomarkers, viruses, bacteria, and parasites", in: *Advanced functional materials* 26.2 (2016), pp. 181–190.

[75] Ewa Nazaruk et al., "Cubic phases in biosensing systems", in: *Analytical and bioanalytical chemistry* 391.5 (2008), p. 1569.

[76] Chandrashekhar V Kulkarni et al., "Monoolein: a magic lipid?", in: *Physical Chemistry Chemical Physics* 13.8 (2011), pp. 3004–3021.

[77] Hong Qiu and Martin Caffrey, "The phase diagram of the monoolein/water system: metastability and equilibrium aspects", in: *Biomaterials* 21.3 (2000), pp. 223–234.

[78] Anan Yaghmur et al., "Tuning curvature and stability of monoolein bilayers by designer lipid-like peptide surfactants", in: *PLoS One* 2.5 (2007).

[79] Julia Kraineva, Vytautas Smirnovas, and Roland Winter, "Effects of lipid confinement on insulin stability and amyloid formation", in: *Langmuir* 23.13 (2007), pp. 7118–7126.

[80] David P Siegel, "Fourth-Order Curvature Energy Model for the Stability of Bicontinuous Inverted Cubic Phases in Amphiphile- Water Systems", in: *Langmuir* 26.11 (2010), pp. 8673–8683.

[81] David P Siegel, "The Gaussian curvature elastic energy of intermediates in membrane fusion", in: *Biophysical journal* 95.11 (2008), pp. 5200–5215.

[82] David P Siegel and MM Kozlov, "The Gaussian curvature elastic modulus of N-monomethylated dioleoylphosphatidylethanolamine: relevance to membrane fusion and lipid phase behavior", in: *Biophysical journal* 87.1 (2004), pp. 366–374.

[83] DP Siegel and RM Epand, "Effect of influenza hemagglutinin fusion peptide on lamellar/inverted phase transitions in dipalmitoleoylphosphatidylethanolamine: implications for membrane fusion mechanisms", in: *Biochimica et Biophysica Acta (BBA)-Biomembranes* 1468.1-2 (2000), pp. 87–98.

[84] Stephanie Tristram-Nagle and John F Nagle, "HIV-1 fusion peptide decreases bending energy and promotes curved fusion intermediates", in: *Biophysical journal* 93.6 (2007), pp. 2048–2055.

[85] A Colotto and RM Epand, "Structural study of the relationship between the rate of membrane fusion and the ability of the fusion peptide of influenza virus to perturb bilayers", in: *Biochemistry* 36.25 (1997), pp. 7644–7651.

[86] Mariya Chavarha et al., "Hydrophobic surfactant proteins induce a phosphatidylethanolamine to form cubic phases", in: *Biophysical journal* 98.8 (2010), pp. 1549–1557.

[87] JM Seddon, "Lyotropic phase behaviour of biological amphiphiles", in: *Berichte der Bunsengesellschaft für physikalische Chemie* 100.3 (1996), pp. 380–393.

[88] Raghuveer Parthasarathy and Jay T Groves, "Curvature and spatial organization in biological membranes", in: *Soft Matter* 3.1 (2006), pp. 24–33.

[89] Iris K Jarsch, Frederic Daste, and Jennifer L Gallop, "Membrane curvature in cell biology: An integration of molecular mechanisms", in: *Journal of Cell Biology* 214.4 (2016), pp. 375–387.

[90] Juliette Jouhet, "Importance of the hexagonal lipid phase in biological membrane organization", in: *Frontiers in plant science* 4 (2013), p. 494.

[91] Bruno Antonny, "Mechanisms of membrane curvature sensing", in: *Annual review of biochemistry* 80 (2011), pp. 101–123.

[92] James H Hurley et al., "Membrane budding", in: *Cell* 143.6 (2010), pp. 875–887.

[93] Göran Lindblom and Leif Rilfors, "Cubic phases and isotropic structures formed by membrane lipids—possible biological relevance", in: *Biochimica et Biophysica Acta (BBA)-Reviews on Biomembranes* 988.2 (1989), pp. 221–256.

[94] Daisuke Miyoshi and Naoki Sugimoto, "Molecular crowding effects on structure and stability of DNA", in: *Biochimie* 90.7 (2008), pp. 1040–1051.

[95] Steven B Zimmerman and Stefan O Trach, "Estimation of macromolecule concentrations and excluded volume effects for the cytoplasm of Escherichia coli", in: *Journal of molecular biology* 222.3 (1991), pp. 599–620.

[96] R John Ellis and Allen P Minton, "Join the crowd", in: *Nature* 425.6953 (2003), pp. 27–28.

[97] M Erlkamp et al., "Influence of pressure and crowding on the sub-nanosecond dynamics of globular proteins", in: *The Journal of Physical Chemistry B* 119.14 (2015), pp. 4842–4848.

[98] Karin Julius et al., "The effects of osmolytes and crowding on the pressure-induced dissociation and inactivation of dimeric LADH", in: *Physical Chemistry Chemical Physics* 20.10 (2018), pp. 7093–7104.

[99] Karin Julius et al., "Impact of Macromolecular Crowding and Compression on Protein–Protein Interactions and Liquid–Liquid Phase Separation Phenomena", in: *Macromolecules* 52.4 (2019), pp. 1772–1784.

[100] Huan-Xiang Zhou, Germán Rivas, and Allen P Minton, "Macromolecular crowding and confinement: biochemical, biophysical, and potential physiological consequences", in: *Annu. Rev. Biophys.* 37 (2008), pp. 375–397.

[101] Nicholas F Dupuis, Erik D Holmstrom, and David J Nesbitt, "Molecular-crowding effects on single-molecule RNA folding/unfolding thermodynamics and kinetics", in: *Proceedings of the National Academy of Sciences* 111.23 (2014), pp. 8464–8469.

[102] Jillian Tyrrell, Kevin M Weeks, and Gary J Pielak, "Challenge of mimicking the influences of the cellular environment on RNA structure by PEG-induced macromolecular crowding", in: *Biochemistry* 54.42 (2015), pp. 6447–6453.

[103] Duncan Kilburn et al., "Molecular crowding stabilizes folded RNA structure by the excluded volume effect", in: *Journal of the American Chemical Society* 132.25 (2010), pp. 8690–8696.

[104] Rumiana Dimova and Reinhard Lipowsky, "Lipid membranes in contact with aqueous phases of polymer solutions", in: *Soft Matter* 8.24 (2012), pp. 6409–6415.

[105] SW Hui et al., "Use of poly (ethylene glycol) to control cell aggregation and fusion", in: *Colloids and surfaces B: Biointerfaces* 14.1-4 (1999), pp. 213–222.

[106] Barry R Lentz, "PEG as a tool to gain insight into membrane fusion", in: *European Biophysics Journal* 36.4-5 (2007), pp. 315–326.

[107] Hidetoshi Terasawa et al., "Coupling of the fusion and budding of giant phospholipid vesicles containing macromolecules", in: *Proceedings of the National Academy of Sciences* 109.16 (2012), pp. 5942–5947.

[108] Minoru Nakano et al., "Small-angle X-ray scattering and 13C NMR investigation on the internal structure of "cubosomes"", in: *Langmuir* 17.13 (2001), pp. 3917–3922.

[109] Patrick T Spicer et al., "Bicontinuous cubic liquid crystalline phase and cubosome personal care delivery systems", in: *Personal Care Delivery Systems and Formulations* (2003).

[110] Aindrilla S Duttagupta et al., "Cubosomes: innovative nanostructures for drug delivery", in: *Current drug delivery* 13.4 (2016), pp. 482–493.

[111] Hanna MG Barriga, Margaret N Holme, and Molly M Stevens, "Cubosomes: the next generation of smart lipid nanoparticles?", in: *Angewandte Chemie International Edition* 58.10 (2019), pp. 2958–2978.

[112] Benjamin Podbilewicz, "Virus and cell fusion mechanisms", in: *Annual review of cell and developmental biology* 30 (2014), pp. 111–139.

[113] Jelle S Blijleven et al., "Mechanisms of influenza viral membrane fusion", in: *Seminars in cell & developmental biology*, vol. 60, Elsevier, 2016, pp. 78–88.

[114] Nathanial R Eddy and José N Onuchic, "Rotation-activated and cooperative zipping characterize class I viral fusion protein dynamics", in: *Biophysical journal* 114.8 (2018), pp. 1878–1888.

[115] Karen J Cross et al., "Composition and functions of the influenza fusion peptide", in: *Protein and peptide letters* 16.7 (2009), pp. 766–778.

[116] John J Skehel and Don C Wiley, "Receptor binding and membrane fusion in virus entry: the influenza hemagglutinin", in: *Annual review of biochemistry* 69.1 (2000), pp. 531–569.

[117] Ian A Wilson, John J Skehel, and DC Wiley, "Structure of the haemagglutinin membrane glycoprotein of influenza virus at 3 Å resolution", in: *Nature* 289.5796 (1981), pp. 366–373.

[118] Lauri IA Pulkkinen, Sarah J Butcher, and Maria Anastasina, "Tick-borne encephalitis virus: a structural view", in: *Viruses* 10.7 (2018), p. 350.

[119] Karin Stiasny et al., "Membrane interactions of the tick-borne encephalitis virus fusion protein E at low pH", in: *Journal of virology* 76.8 (2002), pp. 3784–3790.

[120] Jinhe Pan et al., "Synthetic fusion peptides of tick-borne encephalitis virus as models for membrane fusion", in: *Biochemistry* 49.2 (2010), pp. 287–296.

[121] Stéphane Roche et al., "Structure of the prefusion form of the vesicular stomatitis virus glycoprotein G", in: *Science* 315.5813 (2007), pp. 843–848.

[122] Irene S Kim et al., "Mechanism of membrane fusion induced by vesicular stomatitis virus G protein", in: *Proceedings of the National Academy of Sciences* 114.1 (2017), E28–E36.

[123] Melina Vallbracht et al., "Structure-function dissection of pseudorabies virus glycoprotein B fusion loops", in: *Journal of virology* 92.1 (2018), e01203–17.

[124] Xiangjie Sun, Sandrine Belouzard, and Gary R Whittaker, "Molecular architecture of the bipartite fusion loops of vesicular stomatitis virus glycoprotein G, a class III viral fusion protein", in: *Journal of Biological Chemistry* 283.10 (2008), pp. 6418–6427.

[125] Stéphane Roche et al., "Crystal structure of the low-pH form of the vesicular stomatitis virus glycoprotein G", in: *Science* 313.5784 (2006), pp. 187–191.

[126] Marija Backovic and Theodore S Jardetzky, "Class III viral membrane fusion proteins", in: *Current opinion in structural biology* 19.2 (2009), pp. 189–196.

[127] AT Da Poian, FA Carneiro, and F Stauffer, "Viral membrane fusion: is glycoprotein G of rhabdoviruses a representative of a new class of viral fusion proteins?", in: *Brazilian journal of medical and biological research* 38.6 (2005), pp. 813–823.

[128] Katrin Weise and Jennifer Reed, "Fusion peptides and transmembrane domains of fusion proteins are characterized by different but specific structural properties", in: *Chembiochem* 9.6 (2008), pp. 934–943.

[129] Zhou Zhou et al., "Enhanced nuclear delivery of anti-cancer drugs using micelles containing releasable membrane fusion peptide and nuclear-targeting retinoic acid", in: *Journal of Materials Chemistry B* 5.34 (2017), pp. 7175–7185.

[130] Salma N Tammam, Hassan ME Azzazy, and Alf Lamprecht, "How successful is nuclear targeting by nanocarriers?", in: *Journal of Controlled Release* 229 (2016), pp. 140–153.

[131] Rita Sala et al., "Collaborative membrane activity and receptor-dependent tumor cell targeting for precise nanoparticle delivery in CXCR4+ colorectal cancer", in: *Acta biomaterialia* 99 (2019), pp. 426–432.

[132] D Needham and E Evans, "Structure and mechanical properties of giant lipid (DMPC) vesicle bilayers from 20. degree. C below to 10. degree. C above the liquid crystal-crystalline phase transition at 24. degree. C", in: *Biochemistry* 27.21 (1988), pp. 8261–8269.

[133] J Eisenblätter and R Winter, "Pressure effects on the structure and phase behavior of DMPC-gramicidin lipid bilayers: a synchrotron SAXS and 2H-NMR spectroscopy study", in: *Biophysical journal* 90.3 (2006), pp. 956–966.

[134] S Krishna Prasad et al., "Pressure studies on two hydrated phospholipids-1, 2-dimyristoyl-phosphatidylcholine and 1, 2-dipalmitoyl-phosphatidylcholine", in: *Chemistry and physics of lipids* 43.3 (1987), pp. 227–235.

[135] Hayato Ichimori et al., "Barotropic phase transitions and pressure-induced interdigitation on bilayer membranes of phospholipids with varying acyl chain lengths", in: *Biochimica et Biophysica Acta (BBA)-Biomembranes* 1414.1-2 (1998), pp. 165–174.

[136] Patricia Losada-Pérez et al., "Effect of cholesterol on the phase behavior of solid-supported lipid vesicle layers", in: *The Journal of Physical Chemistry B* 119.15 (2015), pp. 4985–4992.

[137] Margus R Vist and James H Davis, "Phase equilibria of cholesterol/di"-palmitoyl"-phos"-phatidyl"-choline mixtures: deuterium nuclear magnetic resonance and differential scanning calorimetry", in: *Biochemistry* 29.2 (1990), pp. 451–464.

[138] Michael Rappolt et al., "Structural, dynamic and mechanical properties of POPC at low cholesterol concentration studied in pressure/temperature space", in: *European Biophysics Journal* 31.8 (2003), pp. 575–585.

[139] Judith Peters et al., "Thermodynamics of lipid multi-lamellar vesicles in presence of sterols at high hydrostatic pressure", in: *Scientific reports* 7.1 (2017), pp. 1–15.

[140] Kell Mortensen et al., "Structural properties of a phosphatidylcholine-cholesterol system as studied by small-angle neutron scattering: ripple structure and phase diagram", in: *Biochimica et Biophysica Acta (BBA)-Biomembranes* 945.2 (1988), pp. 221–245.

[141] Diether J Recktenwald and Harden M McConnell, "Phase equilibriums in binary mixtures of phosphatidylcholine and cholesterol", in: *Biochemistry* 20.15 (1981), pp. 4505–4510.

[142] Thalia T Mills et al., "Effects of cholesterol and unsaturated DOPC lipid on chain packing of saturated gel-phase DPPC bilayers", in: *General physiology and biophysics* 28.2 (2009), p. 126.

[143] Marcus Trapp et al., "High hydrostatic pressure effects investigated by neutron scattering on lipid multilamellar vesicles", in: *Physical Chemistry Chemical Physics* 15.48 (2013), pp. 20951–20956.

[144] Ulrike Mennicke and Tim Salditt, "Preparation of solid-supported lipid bilayers by spin-coating", in: *Langmuir* 18.21 (2002), pp. 8172–8177.

[145] Erich Sackmann, "Supported membranes: scientific and practical applications", in: *Science* 271.5245 (1996), pp. 43–48.

[146] Ralf P Richter, Rémi Bérat, and Alain R Brisson, "Formation of solid-supported lipid bilayers: an integrated view", in: *Langmuir* 22.8 (2006), pp. 3497–3505.

[147] Ulrike Mennicke, Doru Constantin, and Tim Salditt, "Structure and interaction potentials in solid-supported lipid membranes studied by x-ray reflectivity at varied osmotic pressure", in: *The European Physical Journal E* 20.2 (2006), pp. 221–230.

[148] L Perino-Gallice et al., "Dewetting of solid-supported multilamellar lipid layers", in: *The European Physical Journal E* 8.3 (2002), pp. 275–282.

[149] Wei-Chin Hung et al., "The condensing effect of cholesterol in lipid bilayers", in: *Biophysical journal* 92.11 (2007), pp. 3960–3967.

[150] TA Harroun et al., "Finite-size effects do not reduce the repeat spacing of phospholipid multibilayer stacks on a rigid substrate", in: *The European Physical Journal E* 13.4 (2004), pp. 359–362.

[151] Tim Salditt, "Thermal fluctuations and stability of solid-supported lipid membranes", in: *Journal of Physics: Condensed Matter* 17.6 (2005), R287.

[152] Benedikt Nowak et al., "Solid-supported lipid multilayers under high hydrostatic pressure", in: *Langmuir* 32.11 (2016), pp. 2638–2643.

[153] Göran Surmeier et al., "Cholesterol modulates the pressure response of DMPC membranes", in: *Biophysical chemistry* 252 (2019), p. 106210.

[154] Eric Schneider, "Aufbau eines Multilayer-Monochromators an der Strahllinie BL2", Master thesis, Technische Universität Dortmund, 2019.

[155] Eric Schneider et al., "The new wide and small angle scattering setup at beamline BL2 of DELTA", in: *DELTA Annual Report 2019* (2019), pp. 21–22.

[156] Christina Krywka et al., "The small-angle and wide-angle X-ray scattering set-up at beamline BL9 of DELTA", in: *Journal of synchrotron radiation* 14.3 (2007), pp. 244–251.

[157] Michael Paulus et al., "An access to buried interfaces: the X-ray reflectivity set-up of BL9 at DELTA", in: *Journal of synchrotron radiation* 15.6 (2008), pp. 600–605.

[158] D-M Smilgies et al., "Troika II: a versatile beamline for the study of liquid and solid interfaces", in: *Journal of synchrotron radiation* 12.3 (2005), pp. 329–339.

[159] Veijo Honkimäki, "Engineering materials research at ESRF", in: *Synchrotron Radiation News* 30.3 (2017), pp. 48–54.

[160] Harold A Scheraga, "Theory of hydrophobic interactions", in: *Journal of Biomolecular Structure and Dynamics* 16.2 (1998), pp. 447–460.

[161] B Widom, P Bhimalapuram, and Kenichiro Koga, "The hydrophobic effect", in: *Physical Chemistry Chemical Physics* 5.15 (2003), pp. 3085–3093.

[162] Jacob N Israelachvili, D John Mitchell, and Barry W Ninham, "Theory of self-assembly of hydrocarbon amphiphiles into micelles and bilayers", in: *Journal of the Chemical Society, Faraday Transactions 2: Molecular and Chemical Physics* 72 (1976), pp. 1525–1568.

[163] Sten Andersson et al., "Minimal surfaces and structures: from inorganic and metal crystals to cell membranes and biopolymers", in: *Chemical Reviews* 88.1 (1988), pp. 221–242.

[164] H Schwarz, "Monatsber", in: *Berlin Akad* 3 (1865), p. 149.

[165] Hermann Amandus Schwarz, "Über ein die Flächen kleinsten Flächeninhalts betreffendes Problem der Variationsrechnung", in: *Gesammelte Mathematische Abhandlungen*, Springer, 1890, pp. 223–269.

[166] AH Schoen, "Infinite periodic minimal surfaces without selfintersections NASA Technical Report TN D-5541", in: *Washington DC* (1970).

[167] Salvatore Assenza and Raffaele Mezzenga, "Curvature and bottlenecks control molecular transport in inverse bicontinuous cubic phases", in: *The Journal of Chemical Physics* 148.5 (2018), p. 054902.

[168] ST Hyde and Sten Andersson, "A cubic structure consisting of a lipid bilayer forming an infinite periodic minimum surface of the gyroid type in the glycerol-monooleat-water system", in: *Zeitschrift für Kristallographie-Crystalline Materials* 168.1-4 (1984), pp. 213–220.

[169] R Winter, "Effects of hydrostatic pressure on lipid and surfactant phases", in: *Current opinion in colloid & interface science* 6.3 (2001), pp. 303–312.

[170] Frédérick J-M de Meyer et al., "Molecular simulation of the DMPC-cholesterol phase diagram", in: *The Journal of Physical Chemistry B* 114.32 (2010), pp. 10451–10461.

[171] Todd PW McMullen, Ruthven NAH Lewis, and Ronald N McElhaney, "Differential scanning calorimetric study of the effect of cholesterol on the thermotropic phase behavior of a homologous series of linear saturated phosphatidylcholines", in: *Biochemistry* 32.2 (1993), pp. 516–522.

[172] S Halstenberg et al., "Cholesterol-induced variations in the volume and enthalpy fluctuations of lipid bilayers", in: *Biophysical journal* 75.1 (1998), pp. 264–271.

[173] Juan J Giner-Casares, Gerald Brezesinski, and Helmuth Möhwald, "Langmuir monolayers as unique physical models", in: *Current opinion in colloid & interface science* 19.3 (2014), pp. 176–182.

[174] Vladimir M Kaganer, Helmuth Möhwald, and Pulak Dutta, "Structure and phase transitions in Langmuir monolayers", in: *Reviews of Modern Physics* 71.3 (1999), p. 779.

[175] Ka Yee C Lee, "Collapse mechanisms of Langmuir monolayers", in: *Annu. Rev. Phys. Chem.* 59 (2008), pp. 771–791.

[176] Flávia Amanda Pedroso de Morais et al., "Hypericin photodynamic activity in DPPC liposomes–part II: stability and application in melanoma B16-F10 cancer cells", in: *Photochemical & Photobiological Sciences* 19.5 (2020), pp. 620–630.

[177] Ygara S Mendes et al., "The structural dynamics of the flavivirus fusion peptide–membrane interaction", in: *PLoS One* 7.10 (2012), e47596.

[178] Kerstin de Meijere, Gerald Brezesinski, and Helmuth Möhwald, "Polyelectrolyte coupling to a charged lipid monolayer", in: *Macromolecules* 30.8 (1997), pp. 2337–2342.

[179] RP Rand and VA Parsegian, "Physical force considerations in model and biological membranes", in: *Canadian journal of biochemistry and cell biology* 62.8 (1984), pp. 752–759.

[180] V Adrian Parsegian, Nola Fuller, and R Peter Rand, "Measured work of deformation and repulsion of lecithin bilayers", in: *Proceedings of the National Academy of Sciences* 76.6 (1979), pp. 2750–2754.

[181] George W Kemble, Tsafi Danieli, and Judith M White, "Lipid-anchored influenza hemagglutinin promotes hemifusion, not complete fusion", in: *Cell* 76.2 (1994), pp. 383–391.

[182] Leonid V Chernomordik and Michael M Kozlov, "Membrane hemifusion: crossing a chasm in two leaps", in: *Cell* 123.3 (2005), pp. 375–382.

[183] AE Spruce, A Iwata, and Wolfhard Almers, "The first milliseconds of the pore formed by a fusogenic viral envelope protein during membrane fusion.", in: *Proceedings of the National Academy of Sciences* 88.9 (1991), pp. 3623–3627.

[184] C Schoch and Robert Blumenthal, "Role of the fusion peptide sequence in initial stages of influenza hemagglutinin-induced cell fusion.", in: *Journal of Biological Chemistry* 268.13 (1993), pp. 9267–9274.

[185] Yuta Kanai et al., "Cell–cell fusion induced by reovirus FAST proteins enhances replication and pathogenicity of non-enveloped dsRNA viruses", in: *PLoS pathogens* 15.4 (2019), e1007675.

[186] Marta Ciechonska and Roy Duncan, "Reovirus FAST proteins: virus-encoded cellular fusogens", in: *Trends in microbiology* 22.12 (2014), pp. 715–724.

[187] Yves Gaudin, "Rabies virus-induced membrane fusion pathway", in: *The Journal of cell biology* 150.3 (2000), pp. 601–612.

[188] Aurélie A Albertini et al., "Characterization of monomeric intermediates during VSV glycoprotein structural transition", in: *PLoS pathogens* 8.2 (2012).

[189] Eduard Baquero et al., "Intermediate conformations during viral fusion glycoprotein structural transition", in: *Current opinion in virology* 3.2 (2013), pp. 143–150.

[190] Xing Han and Lukas K Tamm, "A host–guest system to study structure–function relationships of membrane fusion peptides", in: *Proceedings of the National Academy of Sciences* 97.24 (2000), pp. 13097–13102.

[191] Loredana Vaccaro et al., "Plasticity of influenza haemagglutinin fusion peptides and their interaction with lipid bilayers", in: *Biophysical journal* 88.1 (2005), pp. 25–36.

[192] Ding-Kwo Chang et al., "The Amino-terminal Region of the Fusion Peptide of Influenza Virus Hemagglutinin HA2 Inserts into Sodium Dodecyl Sulfate Micelle with Residues 16–18 at the Aqueous Boundary at Acidic pH - Oligomerization and the Conformational Flexibility", in: *Journal of Biological Chemistry* 275.25 (2000), pp. 19150–19158.

[193] Justin L Lorieau, John M Louis, and Ad Bax, "The complete influenza hemagglutinin fusion domain adopts a tight helical hairpin arrangement at the lipid: water interface", in: *Proceedings of the National Academy of Sciences* 107.25 (2010), pp. 11341–11346.

[194] Alex L Lai et al., "Fusion peptide of influenza hemagglutinin requires a fixed angle boomerang structure for activity", in: *Journal of Biological Chemistry* 281.9 (2006), pp. 5760–5770.

[195] Sho Takahashi, "Conformation of membrane fusion-active 20-residue peptides with or without lipid bilayers. Implication of alpha-helix formation for membrane fusion", in: *Biochemistry* 29.26 (1990), pp. 6257–6264.

[196] Xing Han et al., "Membrane structure and fusion-triggering conformational change of the fusion domain from influenza hemagglutinin", in: *Nature structural biology* 8.8 (2001), pp. 715–720.

[197] Shu-fang Cheng, Assen B Kantchev, and Ding-kwo Chang, "Fluorescence evidence for a loose self-assembly of the fusion peptide of influenza virus HA2 in the lipid bilayer", in: *Molecular membrane biology* 20.4 (2003), pp. 345–351.

[198] Boris G Tenchov, Robert C MacDonald, and Barry R Lentz, "Fusion peptides promote formation of bilayer cubic phases in lipid dispersions. An x-ray diffraction study", in: *Biophysical journal* 104.5 (2013), pp. 1029–1037.

[199] Pavel E Volynsky et al., "Effect of lipid composition on the "membrane response" induced by a fusion peptide", in: *Biochemistry* 44.44 (2005), pp. 14626–14637.

[200] Mingtao Ge and Jack H Freed, "Fusion peptide from influenza hemagglutinin increases membrane surface order: an electron-spin resonance study", in: *Biophysical journal* 96.12 (2009), pp. 4925–4934.

[201] Patrick Lagüe, Benoît Roux, and Richard W Pastor, "Molecular dynamics simulations of the influenza hemagglutinin fusion peptide in micelles and bilayers: conformational analysis of peptide and lipids", in: *Journal of molecular biology* 354.5 (2005), pp. 1129–1141.

[202] Julien Lescar et al., "The fusion glycoprotein shell of Semliki Forest virus: an icosahedral assembly primed for fusogenic activation at endosomal pH", in: *Cell* 105.1 (2001), pp. 137–148.

[203] Stéphane Bressanelli et al., "Structure of a flavivirus envelope glycoprotein in its low-pH-induced membrane fusion conformation", in: *The EMBO journal* 23.4 (2004), pp. 728–738.

[204] Steven L Allison et al., "Mutational evidence for an internal fusion peptide in flavivirus envelope protein E", in: *Journal of virology* 75.9 (2001), pp. 4268–4275.

[205] Yorgo Modis et al., "Structure of the dengue virus envelope protein after membrane fusion", in: *Nature* 427.6972 (2004), pp. 313–319.

[206] Brenda L Fredericksen and Michael A Whitt, "Vesicular stomatitis virus glycoprotein mutations that affect membrane fusion activity and abolish virus infectivity.", in: *Journal of Virology* 69.3 (1995), pp. 1435–1443.

[207] SE Delos, JM Gilbert, and JM White, "The central proline of an internal viral fusion peptide serves two important roles", in: *Journal of virology* 74.4 (2000), pp. 1686–1693.

[208] L Zhang and HARA P Ghosh, "Characterization of the putative fusogenic domain in vesicular stomatitis virus glycoprotein G.", in: *Journal of virology* 68.4 (1994), pp. 2186–2193.

[209] Dieter Langosch, Bettina Brosig, and Rüdiger Pipkorn, "Peptide mimics of the vesicular stomatitis virus G-protein transmembrane segment drive membrane fusion in vitro", in: *Journal of Biological Chemistry* 276.34 (2001), pp. 32016–32021.

[210] Suren A Tatulian and Lukas K Tamm, "Secondary structure, orientation, oligomerization, and lipid interactions of the transmembrane domain of influenza hemagglutinin", in: *Biochemistry* 39.3 (2000), pp. 496–507.

[211] Li-Ping Liu and Charles M Deber, "Uncoupling Hydrophobicity and Helicity in Transmembrane Segments - α-Helical Propensities of the Amino Acids in Non-Polar Environments", in: *Journal of Biological Chemistry* 273.37 (1998), pp. 23645–23648.

[212] Shun-Cheng Li and CHARLES M DEBER, "Influence of glycine residues on peptide conformation in membran environments", in: *International journal of peptide and protein research* 40.3-4 (1992), pp. 243–248.

[213] Arthur G Street and Stephen L Mayo, "Intrinsic β-sheet propensities result from van der Waals interactions between side chains and the local backbone", in: *Proceedings of the national academy of sciences* 96.16 (1999), pp. 9074–9076.

[214] Catherine K Smith, Jane M Withka, and Lynne Regan, "A thermodynamic scale for the. beta.-sheet forming tendencies of the amino acids", in: *Biochemistry* 33.18 (1994), pp. 5510–5517.

[215] Dieter Langosch et al., "Peptide mimics of SNARE transmembrane segments drive membrane fusion depending on their conformational plasticity", in: *Journal of molecular biology* 311.4 (2001), pp. 709–721.

[216] Diane Z Cleverley and John Lenard, "The transmembrane domain in viral fusion: essential role for a conserved glycine residue in vesicular stomatitis virus G protein", in: *Proceedings of the National Academy of Sciences* 95.7 (1998), pp. 3425–3430.

[217] Derek Odell et al., "Influence of membrane anchoring and cytoplasmic domains on the fusogenic activity of vesicular stomatitis virus glycoprotein G.", in: *Journal of virology* 71.10 (1997), pp. 7996–8000.

[218] Maurice B Burg and Joan D Ferraris, "Intracellular organic osmolytes: function and regulation", in: *Journal of Biological Chemistry* 283.12 (2008), pp. 7309–7313.

[219] Paul H Yancey et al., "Living with water stress: evolution of osmolyte systems", in: *Science* 217.4566 (1982), pp. 1214–1222.

[220] Maurice B Burg, Joan D Ferraris, and Natalia I Dmitrieva, "Cellular response to hyperosmotic stresses", in: *Physiological reviews* 87.4 (2007), pp. 1441–1474.

[221] Paul H Yancey, "Water stress, osmolytes and proteins", in: *American Zoologist* 41.4 (2001), pp. 699–709.

[222] R Gilles, ""Compensatory" organic osmolytes in high osmolarity and dehydration stresses: history and perspectives", in: *Comparative Biochemistry and Physiology Part A: Physiology* 117.3 (1997), pp. 279–290.

[223] Deepak R Canchi and Angel E García, "Cosolvent effects on protein stability", in: *Annual review of physical chemistry* 64 (2013), pp. 273–293.

[224] Tiao-Yin Lin and Serge N Timasheff, "Why do some organisms use a urea-methylamine mixture as osmolyte? Thermodynamic compensation of urea and trimethylamine N-oxide interactions with protein", in: *Biochemistry* 33.42 (1994), pp. 12695–12701.

[225] Jason R Treberg et al., "The accumulation of methylamine counteracting solutes in elasmobranchs with differing levels of urea: a comparison of marine and freshwater species", in: *Journal of experimental biology* 209.5 (2006), pp. 860–870.

[226] Martin C Stumpe and Helmut Grubmüller, "Interaction of urea with amino acids: implications for urea-induced protein denaturation", in: *Journal of the American Chemical Society* 129.51 (2007), pp. 16126–16131.

[227] Deepak R Canchi and Angel E García, "Backbone and side-chain contributions in protein denaturation by urea", in: *Biophysical journal* 100.6 (2011), pp. 1526–1533.

[228] Soyoung Lee, Yuen Lai Shek, and Tigran V Chalikian, "Urea interactions with protein groups: A volumetric study", in: *Biopolymers* 93.10 (2010), pp. 866–879.

[229] DW Bolen and Ilia V Baskakov, "The osmophobic effect: natural selection of a thermodynamic force in protein folding", in: *Journal of molecular biology* 310.5 (2001), pp. 955–963.

[230] D Wayne Bolen and George D Rose, "Structure and energetics of the hydrogen-bonded backbone in protein folding", in: *Annu. Rev. Biochem.* 77 (2008), pp. 339–362.

[231] Aijun Wang and DW Bolen, "A naturally occurring protective system in urea-rich cells: mechanism of osmolyte protection of proteins against urea denaturation", in: *Biochemistry* 36.30 (1997), pp. 9101–9108.

[232] Yufeng Liu and DW Bolen, "The peptide backbone plays a dominant role in protein stabilization by naturally occurring osmolytes", in: *Biochemistry* 34.39 (1995), pp. 12884–12891.

[233] Sandip Paul and Grenfell N Patey, "Structure and interaction in aqueous urea-trimethylamine-N-oxide solutions", in: *Journal of the American Chemical Society* 129.14 (2007), pp. 4476–4482.

[234] Sandip Paul and GN Patey, "The influence of urea and trimethylamine-N-oxide on hydrophobic interactions", in: *The Journal of Physical Chemistry B* 111.28 (2007), pp. 7932–7933.

[235] Pritam Ganguly et al., "Mutual exclusion of urea and trimethylamine N-oxide from amino acids in mixed solvent environment", in: *The journal of physical chemistry letters* 6.4 (2015), pp. 581–585.

[236] ED Kadtsyn, AV Anikeenko, and NN Medvedev, "Structure of Aqueous Solutions of Trimethylaminoxide, Urea, and Their Mixture", in: *Journal of Structural Chemistry* 59.2 (2018), pp. 347–354.

[237] Nikolai Smolin et al., "TMAO and urea in the hydration shell of the protein SNase", in: *Physical Chemistry Chemical Physics* 19.9 (2017), pp. 6345–6357.

[238] Wen Jun Xie et al., "Large hydrogen-bond mismatch between TMAO and urea promotes their hydrophobic association", in: *Chem* 4.11 (2018), pp. 2615–2627.

[239] Xiaojing Teng and Toshiko Ichiye, "Dynamical Effects of Trimethylamine N-Oxide on Aqueous Solutions of Urea", in: *The Journal of Physical Chemistry B* 123.5 (2019), pp. 1108–1115.

[240] Marius Herzog et al., "Effect of ectoine, hydroxyectoine and β-hydroxybutyrate on the temperature and pressure stability of phospholipid bilayer membranes of different complexity", in: *Colloids and Surfaces B: Biointerfaces* 178 (2019), pp. 404–411.

[241] Samy R Al-Ayoubi et al., "Combined effects of osmotic and hydrostatic pressure on multilamellar lipid membranes in the presence of PEG and trehalose", in: *Soft matter* 14.43 (2018), pp. 8792–8802.

[242] Hiroshi Takahashi, Akira Matsuo, and Ichro Hatta, "Effects of chaotropic and kosmotropic solutes on the structure of lipid cubic phase: Monoolein-water systems", in: *Molecular Crystals and Liquid Crystals Science and Technology. Section A. Molecular Crystals and Liquid Crystals* 347.1 (2000), pp. 231–238.

[243] Pannur Venkatesu, Ming-Jer Lee, and Ho-mu Lin, "Thermodynamic characterization of the osmolyte effect on protein stability and the effect of GdnHCl on the protein denatured state", in: *The Journal of Physical Chemistry B* 111.30 (2007), pp. 9045–9056.

[244] Pankaj Attri, Pannuru Venkatesu, and Ming-Jer Lee, "Influence of osmolytes and denaturants on the structure and enzyme activity of α-chymotrypsin", in: *The Journal of Physical Chemistry B* 114.3 (2010), pp. 1471–1478.

[245] Martin Caffrey, Victoria Fonseca, and A Carl Leopold, "Lipid-sugar interactions: relevance to anhydrous biology", in: *Plant Physiology* 86.3 (1988), pp. 754–758.

[246] M del C Luzardo et al., "Effect of trehalose and sucrose on the hydration and dipole potential of lipid bilayers", in: *Biophysical Journal* 78.5 (2000), pp. 2452–2458.

[247] Heidi D Andersen et al., "Reconciliation of opposing views on membrane–sugar interactions", in: *Proceedings of the National Academy of Sciences* 108.5 (2011), pp. 1874–1878.

[248] L Saturni et al., "Sugar-induced stabilization of the monoolein Pn 3 m bicontinuous cubic phase during dehydration", in: *Physical Review E* 64.4 (2001), p. 040902.

[249] Zhining Wang, Liqiang Zheng, and Tohru Inoue, "Effect of sucrose on the structure of a cubic phase formed from a monoolein/water mixture", in: *Journal of colloid and interface science* 288.2 (2005), pp. 638–641.

[250] Caleb W Reese et al., "Structural insights into the cubic–hexagonal phase transition kinetics of monoolein modulated by sucrose solutions", in: *Physical Chemistry Chemical Physics* 17.14 (2015), pp. 9194–9204.

[251] Alice B Fulton, "How crowded is the cytoplasm?", in: *Cell* 30.2 (1982), pp. 345–347.

[252] Allen P Minton, "The influence of macromolecular crowding and macromolecular confinement on biochemical reactions in physiological media", in: *Journal of biological chemistry* 276.14 (2001), pp. 10577–10580.

[253] Damien Hall and Allen P Minton, "Macromolecular crowding: qualitative and semiquantitative successes, quantitative challenges", in: *Biochimica et Biophysica Acta (BBA)-Proteins and Proteomics* 1649.2 (2003), pp. 127–139.

[254] Allen P Minton, "[7] Molecular crowding: analysis of effects of high concentrations of inert cosolutes on biochemical equilibria and rates in terms of volume exclusion", in: *Methods in enzymology*, vol. 295, Elsevier, 1998, pp. 127–149.

[255] Germán Rivas, Frank Ferrone, and Judith Herzfeld, "Life in a crowded world: Workshop on the Biological Implications of Macromolecular Crowding", in: *EMBO reports* 5.1 (2004), pp. 23–27.

[256] Kim A Sharp, "Analysis of the size dependence of macromolecular crowding shows that smaller is better", in: *Proceedings of the National Academy of Sciences* 112.26 (2015), pp. 7990–7995.

[257] Sho Asakura and Fumio Oosawa, "On interaction between two bodies immersed in a solution of macromolecules", in: *The Journal of chemical physics* 22.7 (1954), pp. 1255–1256.

[258] Sho Asakura and Fumio Oosawa, "Interaction between particles suspended in solutions of macromolecules", in: *Journal of polymer science* 33.126 (1958), pp. 183–192.

[259] B Götzelmann, Robert Evans, and Siegfried Dietrich, "Depletion forces in fluids", in: *Physical Review E* 57.6 (1998), p. 6785.

[260] Y Mao, ME Cates, and HNW Lekkerkerker, "Depletion force in colloidal systems", in: *Physica a* 222 (1995), pp. 10–24.

[261] Thierry Biben, Peter Bladon, and Daan Frenkel, "Depletion effects in binary hard-sphere fluids", in: *Journal of Physics: Condensed Matter* 8.50 (1996), p. 10799.

[262] Alessio Zaccone and Eugene M Terentjev, "Theory of molecular crowding in Brownian hard-sphere liquids", in: *Physical Review E* 85.6 (2012), p. 061202.

[263] K Devanand and JC Selser, "Asymptotic behavior and long-range interactions in aqueous solutions of poly (ethylene oxide)", in: *Macromolecules* 24.22 (1991), pp. 5943–5947.

[264] Yanwei Ding and Guangzhao Zhang, "Collapse and aggregation of poly (N-isopropylacrylamide) chains in aqueous solutions crowded by polyethylene glycol", in: *The Journal of Physical Chemistry C* 111.14 (2007), pp. 5309–5312.

[265] Qicong Ying and Benjamin Chu, "Overlap concentration of macromolecules in solution", in: *Macromolecules* 20.2 (1987), pp. 362–366.

[266] Nicholas P Money, "Osmotic pressure of aqueous polyethylene glycols: relationship between molecular weight and vapor pressure deficit", in: *Plant physiology* 91.2 (1989), pp. 766–769.

[267] LT Boni, TP Stewart, and SW Hui, "Alterations in phospholipid polymorphism by polyethylene glycol", in: *The Journal of membrane biology* 80.1 (1984), pp. 91–104.

[268] Martin D King and Derek Marsh, "Polymorphic phase behavior of lysopalmitoylphosphatidylcholine in poly (ethylene glycol)-water mixtures", in: *Biochemistry* 28.13 (1989), pp. 5643–5647.

[269] Klaus Arnold et al., "Exclusion of poly (ethylene glycol) from liposome surfaces", in: *Biochimica et Biophysica Acta (BBA)-Biomembranes* 1022.3 (1990), pp. 303–310.

[270] Shinpei Ohki et al., "Molecular mechanisms of membrane fusion", in: *Electrical Phenomena at Interfaces and Biointerfaces* (1987), pp. 673–707.

[271] Rudolf Gross and Achim Marx, *Festkörperphysik*, Walter de Gruyter GmbH & Co KG, 2018.

[272] William Henry Bragg and William Lawrence Bragg, "The reflection of X-rays by crystals", in: *Proceedings of the Royal Society of London. Series A, Containing Papers of a Mathematical and Physical Character* 88.605 (1913), pp. 428–438.

[273] W Friedrich, P Knipping, and Mvon Laue, "Sitzungsber. Math. Phys. Kl. K", in: *Bayer. Akad. Wiss. München* (1912), pp. 303–322.

[274] William Longley and Thomas J McIntosh, "A bicontinuous tetrahedral structure in a liquid-crystalline lipid", in: *Nature* 303.5918 (1983), pp. 612–614.

[275] PE Harper et al., "Electron density modeling and reconstruction of infinite periodic minimal surfaces (IPMS) based phases in lipid-water systems. II. Reconstruction of D surface based phases", in: *The European Physical Journal E* 2.3 (2000), pp. 229–245.

[276] M. Tolan, *X-ray scattering from soft-matter thin films: materials science and basic research*, Springer, 1999.

[277] Lyman G Parratt, "Surface studies of solids by total reflection of X-rays", in: *Physical review* 95.2 (1954), p. 359.

[278] Y Yoneda, "Anomalous surface reflection of X rays", in: *Physical review* 131.5 (1963), p. 2010.

[279] George H Vineyard, "Grazing-incidence diffraction and the distorted-wave approximation for the study of surfaces", in: *Physical Review B* 26.8 (1982), p. 4146.

[280] Lutz Wiegart, "Low Temperature Self-Assembly of Organic Monolayers", dissertation, Technische Universität Dortmund, July 2007.

[281] Paul Scherrer, "Bestimmung der inneren Struktur und der Größe von Kolloidteilchen mittels Röntgenstrahlen", in: *Kolloidchemie Ein Lehrbuch*, Springer, 1912, pp. 387–409.

[282] AL Patterson, "The Scherrer formula for X-ray particle size determination", in: *Physical review* 56.10 (1939), p. 978.

[283] Florian J Wirkert et al., "X-ray reflectivity measurements of liquid/solid interfaces under high hydrostatic pressure conditions", in: *Journal of synchrotron radiation* 21.1 (2014), pp. 76–81.

[284] Christina Krywka et al., "Effect of Osmolytes on Pressure-Induced Unfolding of Proteins: A High-Pressure SAXS Study", in: *ChemPhysChem* 9.18 (2008), pp. 2809–2815.

[285] Thos C Poulter, "Apparatus for optical studies at high pressure", in: *Physical Review* 40.5 (1932), p. 860.

[286] David C Chan, "Mitochondrial fusion and fission in mammals", in: *Annu. Rev. Cell Dev. Biol.* 22 (2006), pp. 79–99.

[287] TC Huang et al., "X-ray powder diffraction analysis of silver behenate, a possible low-angle diffraction standard", in: *Journal of applied crystallography* 26.2 (1993), pp. 180–184.

[288] Jason Briggs, Hesson Chung, and Martin Caffrey, "The temperature-composition phase diagram and mesophase structure characterization of the monoolein/water system", in: *Journal de Physique II* 6.5 (1996), pp. 723–751.

[289] C Czeslik et al., "Temperature-and pressure-dependent phase behavior of monoacylglycerides monoolein and monoelaidin", in: *Biophysical Journal* 68.4 (1995), pp. 1423–1429.

[290] Takeshi Yamada et al., "Dynamical behavior of hydration water molecules between phospholipid membranes", in: *The Journal of Physical Chemistry B* 121.35 (2017), pp. 8322–8329.

[291] Felix Campelo, Harvey T McMahon, and Michael M Kozlov, "The hydrophobic insertion mechanism of membrane curvature generation by proteins", in: *Biophysical journal* 95.5 (2008), pp. 2325–2339.

[292] Doncho V Zhelev et al., "Interaction of synthetic HA2 influenza fusion peptide analog with model membranes", in: *Biophysical journal* 81.1 (2001), pp. 285–304.

[293] Marjorie L Longo et al., "Area expansion and permeation of phospholipid membrane bilayers by influenza fusion peptides and melittin", in: *Langmuir* 14.9 (1998), pp. 2385–2395.

[294] Howard Brockman, "Lipid monolayers: why use half a membrane to characterize protein-membrane interactions?", in: *Current opinion in structural biology* 9.4 (1999), pp. 438–443.

[295] Regine Maget-Dana, "The monolayer technique: a potent tool for studying the interfacial properties of antimicrobial and membrane-lytic peptides and their interactions with lipid membranes", in: *Biochimica et Biophysica Acta (BBA)-Biomembranes* 1462.1-2 (1999), pp. 109–140.

[296] Susanne Dogan, "In-situ analysis of the influence of gases and ions on biological interfaces", dissertation, Technische Universität Dortmund, 2020.

[297] Dubravka Sisak Jung et al., "MYTHEN detector–perspectives in residual stress measurements", in: *Advanced Materials Research*, vol. 996, Trans Tech Publ, 2014, pp. 203–208.

[298] CA Helm et al., "Phospholipid monolayers between fluid and solid states", in: *Biophysical journal* 52.3 (1987), pp. 381–390.

[299] Naoki Takeshita, Masanari Okuno, and Taka-aki Ishibashi, "Molecular conformation of DPPC phospholipid Langmuir and Langmuir–Blodgett monolayers studied by heterodyne-detected vibrational sum frequency generation spectroscopy", in: *Physical Chemistry Chemical Physics* 19.3 (2017), pp. 2060–2066.

[300] J Miñones Jr et al., "The effect of polar groups on structural characteristics of phospholipid monolayers spread at the air–water interface", in: *Colloids and Surfaces A: Physicochemical and Engineering Aspects* 203.1-3 (2002), pp. 273–286.

[301] Andria Aroti et al., "Effects of Hofmeister anions on DPPC Langmuir monolayers at the air- water interface", in: *The Journal of Physical Chemistry B* 108.39 (2004), pp. 15238–15245.

[302] Elżbieta Rudolphi-Skórska, Maria Zembala, and Maria Filek, "Mechanical and electrokinetic effects of polyamines/phospholipid interactions in model membranes", in: *The Journal of membrane biology* 247.1 (2014), pp. 81–92.

[303] I Estrela-Lopis, G Brezesinski, and H Möhwald, "Miscibility of DPPC and DPPA in monolayers at the air/water interface", in: *Chemistry and physics of lipids* 131.1 (2004), pp. 71–80.

[304] Nir Ben-Tal et al., "Binding of small basic peptides to membranes containing acidic lipids: theoretical models and experimental results", in: *Biophysical Journal* 71.2 (1996), pp. 561–575.

[305] Jens Als-Nielsen et al., "Principles and applications of grazing incidence x-ray and neutron scattering from ordered molecular monolayers at the air-water interface", in: *Physics Reports* 246.5 (1994), p. 254.

[306] Kristian Kjaer, "Some simple ideas on x—ray reflection and grazing incidence diffraction from thin surfactant films", in: *Physica B* 198 (1994), pp. 100–109.

[307] Waldemar Kulig et al., "Complex Behavior of Phosphatidylcholine–Phosphatidic Acid Bilayers and Monolayers: Effect of Acyl Chain Unsaturation", in: *Langmuir* 35.17 (2019), pp. 5944–5956.

[308] André Hädicke and Alfred Blume, "Binding of the cationic peptide (KL) 4K to lipid monolayers at the air–water interface: Effect of lipid headgroup charge, acyl chain length, and acyl chain saturation", in: *The Journal of Physical Chemistry B* 120.16 (2016), pp. 3880–3887.

[309] Linus Pauling, Robert B Corey, and Herman R Branson, "The structure of proteins: two hydrogen-bonded helical configurations of the polypeptide chain", in: *Proceedings of the National Academy of Sciences* 37.4 (1951), pp. 205–211.

[310] Robert C Neuman Jr, Walter Kauzmann, and Adam Zipp, "Pressure dependence of weak acid ionization in aqueous buffers", in: *The Journal of Physical Chemistry* 77.22 (1973), pp. 2687–2691.

[311] C Ponchut et al., "MAXIPIX, a fast readout photon-counting X-ray area detector for synchrotron applications", in: *Journal of Instrumentation* 6.01 (2011), p. C01069.

[312] Takeyoshi Taguchi, Christian Brönnimann, and Eric F Eikenberry, "Next generation X-ray detectors for in-house XRD", in: *Powder Diffraction* 23.2 (2008), pp. 101–105.

[313] Paul S Prevéy, "The Use of Person VII Distribution Functions in X-Ray Diffraction Residual Stress Measurement", in: *Advances in X-ray Analysis* 29 (1985), pp. 103–111.

[314] Roland Winter, "Synchrotron X-ray and neutron small-angle scattering of lyotropic lipid mesophases, model biomembranes and proteins in solution at high pressure", in: *Biochimica et Biophysica Acta (BBA)-Protein Structure and Molecular Enzymology* 1595.1-2 (2002), pp. 160–184.

[315] Doru Constantin et al., "Solid-supported lipid multilayers: structure factor and fluctuations", in: *The European Physical Journal E* 12.2 (2003), pp. 283–290.

[316] Alain Caillé, "Remarques sur la diffusion des rayons X dans les smectiques", in: *CR Acad. Sci. Serie B* 274 (1972), pp. 891–893.

[317] Nicuşor Tîmneanu et al., "Auger electron cascades in water and ice", in: *Chemical physics* 299.2-3 (2004), pp. 277–283.

[318] Anchi Cheng and Martin Caffrey, "Free radical mediated x-ray damage of model membranes", in: *Biophysical journal* 70.5 (1996), pp. 2212–2222.

[319] Thierry Charitat et al., "Adsorbed and free lipid bilayers at the solid-liquid interface", in: *The European Physical Journal B-Condensed Matter and Complex Systems* 8.4 (1999), pp. 583–593.

[320] Christoph Naumann, Thomas Brumm, and Thomas M Bayerl, "Phase transition behavior of single phosphatidylcholine bilayers on a solid spherical support studied by DSC, NMR and FT-IR", in: *Biophysical journal* 63.5 (1992), pp. 1314–1319.

Acknowledgments

Numerous people were involved in the creation process of this thesis in various ways and I would like to express my sincere thanks to all of them. The contributions range from the initial conception of the topic and the provision of financial resources, to support with experiments and data analysis, to proofreading. Equally important was the pleasant working atmosphere and the support on a personal level that I experienced. Since it is certainly not possible to reflect the past years in these paragraphs completely and adequately in every respect, I would also like to express my gratitude to all persons not mentioned by name in the following, who directly or indirectly contributed to this work.

First of all, I would like to thank Dr. Julia Nase for giving me the opportunity to work on this exciting topic within her project in the Forschergruppe 1979, Professor Dr. Metin Tolan for the admission to the chair of experimental physics E1a and both for their supervision. I would like to acknowledge Professor Dr. Roland Winter for co-supervising this thesis and for fruitful discussions about experimental results. I thank the Forschergruppe 1979 (**DFG-FOR1979**) for financial support.

I am very grateful for the support of Dr. Julia Nase and Dr. Michael Paulus during my entire time at the chair E1a. This work would not have been possible without their advice and the many hours they invested in discussions, experiments and proofreading. Many thanks also go to Dr. Paul Salmen, who introduced me to sample preparation methods, the high pressure setup and the program LSFIT, and supported me in organizing and conducting my first external experiments at the ESRF. A big thanks also to Dr. Susanne Dogan. From her expertise in the field of molecular biology I have benefited greatly.

I would like to thank Dr. Artem Levin and Professor Dr. Claus Czeslik for sharing their experience with monoolein and the fusion peptides with me. Moreover, I want to acknowledge Dr. Samy Al-Ayoubi for showing me how to prepare multi-lamellar vesicles.

I would like to thank the many people who helped me with the experiments at DELTA and the ESRF and ensured that the measurements ran twenty-four hours a day: Dr. Julia Nase, Dr. Michael Paulus, Dr. Paul Salmen, Dr. Susanne Dogan, Eric Schneider, Mirko Elbers, Dr. Yury Forov, Dr. Simon Egger, Christian Albers, Mike Moron, Jan Latarius, Alina Sparenberg, Kevin Foryt, Fatima Mallal, Lukas Tepper, Dr. Karin Esch, Justin Sonneck, Jennifer Bolle, Marc Moron, Dr. Karin Julius, Arin Banawe, Dr. Julian Schulze, and Dr. Steffen Bieder. A special thanks goes to Dr. Simon Egger from the faculty of chemistry, who stepped in to support an experiment at ID10 and made a considerable contribution to the success of the beamtime with his dedicated work in the laboratory. Moreover, I acknowledge our local contacts Dr. Veijo Honkimäki at ID31 and Dr. Oleg

Konovalov and Dr. Andrei Chumakov at ID10 and the entire staff of both beamlines for the support during our beamtimes at the ESRF. Likewise, I thank Dr. Michael Paulus and Dr. Christian Sternemann for their support during the experiments at BL2 and BL9 at DELTA.

A big thanks also goes to Manuela Linke, who made sure that all administrative matters ran smoothly, was always helpful, for example, when forms had to be filled in correctly, and always processed orders quickly when we unexpectedly ran out of chemicals. I also thank Thorsten Witt for fixing my computer and Georg Jülicher for helping me to install the permanent high pressure setup at BL9.

I would like to thank all current and former colleagues of the chair E1a for the pleasant working environment, the great willingness to help with any work-related issues and also the many enjoyable hours spent on less work-related activities like bowling evenings, soccer games, movie nights and, of course, coffee breaks. I especially want to acknowledge my office colleagues Dr. Susanne Dogan, Christain Albers, Fatima Mallal, and Dr. Nico König. Experimental physics can be frustrating and it is invaluable to have people around to cheer you up, but you need to clean the coffee machine from time to time. A big thanks also to Eric Schneider for his commitment as *Beamline Scientist der Herzen*. Moreover, I thank Dr. Susanne Dogan, Mirko Elbers, Hanna Förster, Christian Albers, Jennifer Bolle, Dr. Julian Schulze, Dr. Nico König and Dr. Hendrik Rahmann for expanding my cinematic horizon, letting me win at Tower Fall, and demonstrating how long a good Nidhogg match takes. I would like to thank Alexander Kononov for regularly going to basketball with me despite our limited talent. I also thank Jan Rasche for introducing me to the sport of bouldering, which was a perfect balance during the writing phase.

Last but not least, I would like to thank my friends and family, especially my parents Marlies and Uwe Surmeier, who supported me throughout my entire studies. The greatest thanks goes to my wonderful girlfriend Dr. Susanne Dogan, who recently showed me how to successfully complete a doctorate. Thank you for always being there for me, for discussing data with me and proofreading this thesis, for your encouragement and support with this work and in all other areas of life. I am glad to have you by my side!